# Persistence and origin of the lunar core dynamo

Clément Suavet[a,1], Benjamin P. Weiss[a], William S. Cassata[b], David L. Shuster[c,d], Jérôme Gattacceca[a,e], Lindsey Chan[f], Ian Garrick-Bethell[f,g], James W. Head[h], Timothy L. Grove[a], and Michael D. Fuller[i]

[a]Department of Earth, Atmospheric, and Planetary Sciences, Massachusetts Institute of Technology, Cambridge, MA 02139; [b]Chemical Sciences Division, Lawrence Livermore National Laboratory, Livermore, CA 94550; [c]Department of Earth and Planetary Science, University of California, Berkeley, CA 94720; [d]Berkeley Geochronology Center, Berkeley, CA 94709; [e]Centre Européen de Recherche et d'Enseignement des Géosciences de l'Environnement, Centre National de la Recherche Scientifique, Université Aix-Marseille 3, 13545 Aix-en-Provence, France; [f]Department of Earth and Planetary Sciences, University of California, Santa Cruz, CA 95064; [g]School of Space Research, Kyung Hee University, Yongin 446–701, South Korea; [h]Department of Geological Sciences, Brown University, Providence, RI 02912; and [i]Hawai'i Institute of Geophysics and Planetology, University of Hawaii at Manoa, Honolulu, HI 96822

The lifetime of the ancient lunar core dynamo has implications for its power source and the mechanism of field generation. Here, we report analyses of two 3.56-Gy-old mare basalts demonstrating that they were magnetized in a stable and surprisingly intense dynamo magnetic field of at least ~13 µT. These data extend the known lifetime of the lunar dynamo by ~160 My and indicate that the field was likely continuously active until well after the final large basin-forming impact. This likely excludes impact-driven changes in rotation rate as the source of the dynamo at this time in lunar history. Rather, our results require a persistent power source like precession of the lunar mantle or a compositional convection dynamo.

high-K mare basalts | paleomagnetism

The existence of a global planetary magnetic field provides evidence of an advecting liquid core. Although the Moon does not have a global field today, lunar crustal magnetism and paleomagnetism in returned samples provide evidence of an ancient lunar dynamo (1, 2). Laser ranging experiments (3) and reanalysis of Apollo-era seismic data (4, 5) indicate that the Moon currently has a small (~330 km) partially molten metallic core. Recent paleomagnetic studies of slowly cooled, unshocked samples demonstrate that the Moon had a core dynamo at 4.2 Ga (6) and 3.7 Ga (7). However, the subsequent history of the lunar dynamo is largely unknown.

Determining the lifetime of the lunar dynamo would constrain the nature of its power source and the mechanism of magnetic field generation. Models of core thermal convection have found that a lunar dynamo can only unambiguously persist for as late as 4.1 Ga, well before the youngest current evidence for the magnetic field at 3.7 Ga (7). Although a compositional convection dynamo driven by the crystallization of the core is also possible, the lifetime of such a dynamo is currently unclear. This has motivated alternative models that use precession (8, 9) and/or basin-forming impacts (10) to power the dynamo mechanically via differential motion between the liquid core and rocky mantle. Precession appears to be capable of powering a dynamo until as late as ~1.8–2.7 Ga (9). By comparison, a dynamo driven by impact-induced unlocking from synchronous rotation could likely be active only when basin-forming impacts occurred, before or during the Early Imbrian epoch (≥~3.72 Ga). Therefore, these two mechanisms could potentially be distinguished using measurements of the lunar magnetic field after this time.

Some Apollo-era paleomagnetic studies argued that the termination of the lunar dynamo occurred before the eruption of the Apollo 11 high-K basalts at ~3.6 Ga (11), whereas others suggested that the dynamo persisted but slowly decayed until at least ~3.2 Ga (12). Two Apollo 11 samples, mare basalts 10017 and 10049, provided contrasting results that were central to this debate. Analyses of 10017 (13–16) identified one of the most stable natural remanent magnetization (NRM) records identified in any lunar sample. However, the presence of Johnson Space Center (JSC) saw marks on some subsamples and what was perceived to be a wide range of paleointensities (~40–90 µT) led these investigators to exclude

10017 as a constraint on the lunar dynamo. Instead, these authors relied on their analyses of 10049, whose subsamples were found to carry a unidirectional magnetization (17) with a seemingly weak paleointensity (4–10 µT). However, our reanalysis of their data with modern multicomponent methods yields paleointensities up to ~30 µT (*SI Appendix*).

A recent paleomagnetic study found that lunar samples with ages of 3.3 Ga and in the range 3.7–3.94 Ga may have recorded a field of several tens of microteslas (18). In this study, only one sample (12002, which has an age of 3.3 Ga) was younger than Apollo high-K basalts. However, the nature of its paleomagnetic record is currently ambiguous: Its NRM does not trend toward the origin during alternating field (AF) demagnetization, its remanent magnetization derivative (REM') paleointensity (19) varies by nearly an order of magnitude throughout the demagnetization, the sample was measured while encased in a container whose moment was similar to the demagnetized sample, and no mutually oriented subsamples were measured.

## Samples

Mare basalts 10017 and 10049 are fine-grained, high-K ilmenite basalts of petrological group A (20, 21). Their major phases are pyroxene (50.6 vol % and 51.3%, respectively), plagioclase (23.6 vol. % and 24.5%, respectively), and ilmenite (15.1 vol % and 14.1%, respectively), and minor mesostasis includes high-K glass (21) (*SI Appendix*). These basalts erupted at ~3.56 Ga and form the present surface of most of the southwest portion of Mare Tranquillitatis. The collected rock samples are thought to have been excavated by the impact that formed West Crater ~100 Ma (21), ~0.5 km from the Apollo 11 landing site.

We observed similar mineral assemblages and compositions as those previously described for these samples (21). Our electron microprobe analyses of metal in 10017,62 and 10049,40 found that it has a composition of nearly pure metallic iron ($Fe_{1-x}Ni_x$ with $x < 0.02$) and is typically intergrown with troilite (*SI Appendix*). Because the high-temperature taenite phase (γ-Fe) with this bulk composition transforms fully to kamacite at 912 °C, which is above Curie temperature of 780 °C (22), the kamacite in these rocks should have acquired a pure thermoremanent magnetization (TRM) during primary cooling rather than the thermochemical remanent magnetization that forms when $x > 0.03$ (23). Rock magnetic experiments (*SI Appendix*) indicate that the kamacite grain size is in the multidomain range for both 10017 and 10049.

To constrain the samples' cooling rates below 1,100 °C, we measured the width of the largest plagioclase lath perpendicular to the (010) faces following the method used by Grove and Beaty (20) (*SI Appendix*, Section 9). Our measured values of 550 µm and 120 µm indicate cooling rates of ~0.03 °C·h$^{-1}$ and ~0.43 °C·h$^{-1}$ for 10017 and 10049, respectively, which correspond to cooling times from the Curie point to ambient lunar surface temperatures of ~$10^3$ d and ~$10^2$ d, respectively. Because these samples are antiophitic, these are likely minimum estimates of the cooling timescale (20). These time scales are much longer than the expected 1-d maximum lifetime of fields generated by basin-forming impacts (24). Therefore, any primary magnetization in these samples is likely a record of a temporally stable field like that expected for a core dynamo. Furthermore, we observed no petrographic evidence for shock (peak pressure <5 GPa), such as plagioclase fracturing, mechanical twinning, or alteration to maskelynite (*SI Appendix*). Mare basalts 10017 and 10049 are therefore ideal samples for testing the lunar dynamo hypothesis late in lunar history.

## NRM

We carried out AF demagnetization up to 85–290 mT on eight mutually oriented subsamples of 10017,378 and on three mutually oriented subsamples of 10049,102 (all samples without JSC saw cut faces). Because 10017 and 10049 were collected as regolith float by the Apollo astronauts, they are not mutually oriented,

although their individual subsamples are mutually oriented with respect to their parent rock. We found that the subsamples had NRM intensities of $5.5 \times 10^{-6}$–$3.5 \times 10^{-5}$ Am$^2$·kg$^{-1}$ for 10017 and $1.1 \times 10^{-5}$ to $2.3 \times 10^{-5}$ Am$^2$·kg$^{-1}$ for 10049. All demagnetized samples were observed to have two components of magnetization (Fig. 1, Table 1, and *SI Appendix*). All samples had a low coercivity (LC) and a high coercivity (HC) component. The LC component was removed by AF demagnetization up to somewhere between 9 and 20 mT for subsamples of 10017, with the exception of subsample 378-10, for which the LC and HC components demagnetized concurrently up to several tens of microteslas. The LC component was removed by AF demagnetization between 4 and 11.5 mT for subsamples of 10049. For all samples (with the exception of subsample 378-10), these values are lower than or comparable to those observed by previous studies: The LC component was removed at ~50 mT for 10017 (16) and at ~20 mT for 10049 (17). The LC component is inconsistent in direction between subsamples (Fig. 2) and decays like an isothermal remanent magnetization (IRM) during AF demagnetization (*SI Appendix*). The ratio of the LC component to an IRM (19) ranges between 0.026 and 0.083 over its coercivity range. These results indicate that the LC components in each basalt are likely to be overprints acquired in a strong artificial field during transportation (25) or preparation of the samples at the JSC.

The HC component was observed to decay throughout the demagnetization up to at least 85 mT for all subsamples. Stepwise demagnetization was carried out up to even higher fields for samples 10017,378-2, 10017,378-3, 10017,378-8, and 10049,102-2 (*SI Appendix*). We found that subsample 378-3 had a directionally stable HC magnetization that continued to decay in intensity up to 120 mT, beyond which it remained directionally stable but without further decay up to 290 mT [likely due to anhysteretic remanent magnetization (ARM) noise]. We found that the HC magnetization in subsample 378-2 was stable in direction and continued to decay in intensity up to 120 mT, at which point the sample had completely demagnetized (i.e., became directionally unstable). Subsample 378-8 was stable in direction and decaying in intensity up to 110 mT, beyond which it remained relatively stable in direction with a superposed random component, again likely due to ARM noise. Subsample 102-2 was stable in direction and decaying in intensity up to 290 mT, whereas subsamples 102-1 and 102-3 were directionally stable and decayed in intensity up to at least 85 mT. The HC components are unidirectional within both 10017,378 and 10049,102. The maximum angle between the HC directions is 18° for 10017 and 8° for 10049. For 10017, the Fisher mean direction 95% confidence angle is 6.0° and the Fisher precision parameter is $k = 153$ (number of samples, $n = 6$). For 10049, the Fisher mean direction 95% confidence angle is 6.9° and the Fisher precision parameter is $k = 478$ ($n = 3$). Given the orientation uncertainty of ~5–10° and maximum angular deviation (MAD) values in the range of 2.8–10.0° for 10017 and 5.2–10.6° for 10049, the HC directions are therefore indistinguishable from one another within both samples. In the absence of a statistical method to estimate whether a magnetization component is origin-trending with a confidence interval, we compared the angle between the best-fitting line through the data and the line connecting the origin with the center of mass of the data [deviation angle (DANG) (26)] with the MAD. We found a DANG < MAD for all HC components for both basalt samples, suggesting that the magnetizations are origin-trending, and are therefore the characteristic magnetizations.

To determine whether the NRMs of 10017 and 10049 were contaminated by viscous remanent magnetization (VRM) acquired during their 40-y exposure to the geomagnetic field since return to Earth, and how much of this VRM subsequently decayed during storage in our shielded room before our NRM measurements, we conducted VRM acquisition and decay experiments (*SI Appendix*). For 10017, we found that the residual VRM would be $9.4 \times 10^{-11}$



**Fig. 1.** NRM in mare basalts 10017 and 10049. Shown is a 2D projection of the NRM vectors of subsamples 10017,378-3; 10017,378-8; 10049,102-1; and 10049,102-2 during AF demagnetization. Solid (●) [open (○)] circles represent end points of magnetization projected onto the Y–Z (X–Y) planes for 10017 and onto the Y'–Z' (X'–Z') planes for 10049. Peak fields for selected AF steps are labeled in microteslas. Red arrows denote HC component directions determined from principal component analyses. Subsample 10017,378-3 (*A*); subsample 10017,378-8 (*B*); subsample 10049,102-1 (*C*); and subsample 10049,102-2 (*D*).

**Table 1. Summary of LC and HC components for subsamples from 10017,378 and 10049,102 obtained with principal component analysis**

| Sample | Component | AF range, mT | Type | Dec., Inc.; ° | MAD, ° | DANG, ° | N | Paleointensity, µT | | |
|---|---|---|---|---|---|---|---|---|---|---|
| | | | | | | | | ARM, 50 µT | ARM, 100 µT | IRM |
| 10017,378-1 | LC | NRM-10 | L | 52.0, −30.9 | 2.3 | | 19 | | | |
| | HC | 10.5–85 | AL | 310.6, −44.0 | 4.1/4.8 | 3.5 | 90 | | | |
| 10017,378-2 | LC | NRM-9 | L | 322.0, 43.5 | 23.3 | | 17 | | | |
| | HC | 9.5–120 | AL | 310.0, −35.6 | 2.8/3.6 | 1.3 | 102 | 83.5 ± 1.2 | 80.6 ± 0.8 | 95.1 ± 4.6 |
| 10017,378-3 | LC | NRM-10 | L | 271.3, 25.4 | 7.9 | | 19 | | | |
| | HC | 10.5–290 | AL | 312.6, −30.1 | 4.8/5.7 | 3.0 | 101 | 78.2 ± 1.7 | 76.7 ± 1.1 | 82.9 ± 1.6 |
| 10017,378-6 | LC | NRM-20 | L | 232.6, 25.6 | 7.8 | | 39 | | | |
| | HC | 20.5–85 | AL | 303.6, −34.0 | 7.0/12.3 | 1.9 | 70 | | | |
| 10017,378-7 | LC | NRM-10 | L | 186.8, 16.0 | 3.0 | | 19 | | | |
| | HC | 10.5–85 | AL | 308.7, −35.4 | 3.9/5.7 | 2.3 | 90 | 64.9 ± 1.2 | 55.5 ± 0.8 | 61.9 ± 3.0 |
| 10017,378-8 | LC | NRM-13 | L | 213.1, 26.7 | 5.2 | | 25 | | | |
| | HC | 13.5–110 | AL | 297.1, −28.8 | 10.0/14.0 | 5.8 | 95 | 50.5 ± 1.5 | 47.2 ± 1.6 | 43.2 ± 2.3 |
| 10017,378-10 | LC | NRM-20 | L | 219.2, −24.1 | 7.3 | | 39 | | | |
| | HC | 20–180 | AL | 271.7, −51.4 | 3.8/4.9 | 2.5* | 128 | | | |
| | HC | 20–180 | C | 78.1, −37.9 | 18.2 | | 128 | | | |
| | All | NRM-180 | C | 95.3, −37.6 | 15.7 | | 166 | | | |
| 10017,378-11 | LC | NRM-15 | L | 243.3, −58.6 | 8.2 | | 30 | | | |
| | HC | 15–180 | AL | 313.5, −40.1 | 3.0/4.2 | 4.1* | 137 | | | |
| 10049,102-1 | LC | NRM-10.5 | L | 353.1, −53.3 | 5.7 | | 20 | | | |
| | HC | 11–85 | AL | 332.5, −77.9 | 10.6/13.7 | 4.7 | 89 | 69.7 ± 5.3 | 86.3 ± 4.6 | 95.2 ± 4.3 |
| 10049,102-2 | LC | NRM-11.5 | L | 175.2, −51.2 | 12.6 | | 22 | | | |
| | HC | 12–290 | AL | 294.2, −80.2 | 5.2/6.0 | 2.9 | 96 | 55.2 ± 1.3 | 49.3 ± 1.0 | 59.1 ± 3.2 |
| 10049,102-3 | LC | NRM-4 | L | 268.6, −1.1 | 23.8 | | 3 | | | |
| | HC | 6–85 | AL | 339.7, −79.1 | 6.6/9.1 | 7.6 | 20 | | | |

The first column gives the subsample name and component name; the second column gives the magnetization component; the third column gives the range of AF steps used for the fit; the fourth column gives the fit type (AL, line anchored to the origin; C, circle fit forced through the origin, poles reported; L, line); the fifth column gives the declination (Dec.) and inclination (Inc.) of the fit direction (for line fits) or great circle pole (for circle fits); the sixth column gives the MAD of the component forced through the origin/not forced through the origin; the seventh column gives the DANG; and the eighth column gives the number of AF steps used in fit (N). The last three columns give paleointensities: ARM paleointensity (in microteslas) = (NRM lost)/(ARM lost)/$f'$ × [bias field (in microteslas)] × anisotropy correction factor, IRM paleointensity (in microteslas) = (NRM lost)/(IRM lost) × $a$ × anisotropy correction factor. We used $f' = 1.34$ and $a = 3,000$. Uncertainties on each paleointensity value are formal 95% confidence intervals on the slope fit using the Student $t$ test (31) and do not include the factor of ∼3–5 uncertainty associated with the unknown ratios of ARM and IRM to TRM.
*DANG calculated using first point of fit.

Am², equivalent to only 2.4% of the observed initial NRM. For 10049, we found that the residual VRM would be $9.3 \times 10^{-11}$ Am², equivalent to only 2.7% of the initial NRM. Therefore, neither the



**Fig. 2.** Equal area stereographic projection of NRM component fits. Circles denote HC directions (primary magnetization) for each subsample, and squares denote LC directions (overprint). The stars are the Fisher mean HC direction from principal component analyses, with surrounding dashed ellipses indicating 95% formal confidence intervals on mean directions (not accounting for additional ∼3–5° mutual orientation uncertainty). (A) Sample 10017,378. Black and gray symbols correspond to samples measured at the Massachusetts Institute of Technology and University of California, Santa Cruz, respectively. The dashed great circle denotes a circle fit forced through the origin for the HC data of subsample 10. (B) Sample 10049,102.

LC nor HC components of 10017 and 10049 are likely to be VRM-acquired in the Earth's magnetic field.

Although our petrographic observations exclude shocks with pressures >5 GPa, even shocks with lower peak pressures could produce magnetization if a field were present. To investigate this possibility, we conducted pressure remanent magnetization (PRM) acquisition experiments (*SI Appendix*) for subsamples 378-3 and 102-1 following the method used by Gattacceca (27). Like previous such studies of lunar rocks (27), we found that PRM was acquired dominantly by LC grains (<∼30–40 mT) with even the 2.0-GPa PRM significantly softer than the NRM (*SI Appendix*). This suggests that neither the LC nor HC components are likely shock remanent magnetizations (SRM). We found that a 1-mT field and a 2-mT field would have been necessary to produce the LC and HC components of 378-3, respectively. Similarly, a 0.1-mT field and a 0.3-mT field would have been necessary to produce the LC and HC components of 102-1, respectively. Such fields are well above theoretical estimates of maximum dynamo fields for the Moon and at the upper end of predicted impact-generated fields (e.g., refs. 28, 29). Therefore, these field values provide further evidence against an SRM origin for either NRM component.

We conducted AF demagnetization of laboratory-induced magnetizations and compared them with that of the NRM. The HC component in each rock demagnetizes like an ARM [an analog of TRM (30)] and unlike either a PRM or an IRM (*SI Appendix*).

Therefore, the HC components of 10017 and 10049 are likely TRMs acquired during cooling in a stable field on the Moon.

## Paleointensity

The HC components of 10017,378 yielded anisotropy-corrected paleointensities ranging between 47 and 84 µT from the ARM method and between 43 and 95 µT from the IRM method; 10049,102 yielded anisotropy-corrected HC component paleointensities ranging between 49.3 and 86.3 µT from the ARM method and between 59.1 and 95.2 µT from the IRM method (Table 1 and *SI Appendix*). The range of variability between subsamples is expected, given the uncertainty in the calibration factors for these methods. Furthermore, the similarity between the ARM and IRM values gives confidence that each method is producing relatively accurate results. Given that each individual paleointensity is uncertain by a factor of 3–5, the multispecimen mean values should be significantly less uncertain than this factor. The average values for the ARM method are 67 ± 15 µT for 10017 and 65 ± 14 µT for 10049 [uncertainties are formal 95% confidence intervals on the slope fit using the Student *t* test (31) and do not include the factor of ~3–5 uncertainty associated with the unknown ratios of ARM and IRM to TRM]. The average values for the IRM method are 71 ± 21 µT for 10017 and 77 ± 18 µT for 10049 (uncertainties on mean values are observed 1 SD from multiple samples). These paleointensities are indistinguishable within the uncertainty and give a mean value for all experiments on both samples of 69 ± 16 µT, which corresponds to a very conservative minimum paleofield of ~13 µT. These values are also within error of the paleointensity inferred at 3.7 Ga from mare basalt 10020 (7) and consistent with values recently obtained for other samples with crystallization ages from 3.7 to 3.94 Ga (18) (although the age and origin of the magnetization in the latter samples are not well constrained). These paleointensities are higher than previous estimates for 10049, likely due to lack of complete NRM demagnetization in these earlier studies (*SI Appendix*).

## Thermochronology

The 3.56-Ga crystallization ages of 10017 and 10049 place an upper limit on the time at which they acquired their magnetization. It is possible that the magnetization of these rocks could have been acquired or reset during thermal excursions following their formation. Although the lack of shock features in these rocks precludes direct shock heating, they could have experienced temperature excursions from burial in a hot ejecta blanket or nearby volcanic activity. To assess this possibility, we conducted $^{40}$Ar/$^{39}$Ar and $^{38}$Ar/$^{37}$Ar thermochronometry on two whole-rock subsamples of 10017 and 10049 (Fig. 3 and *SI Appendix*).
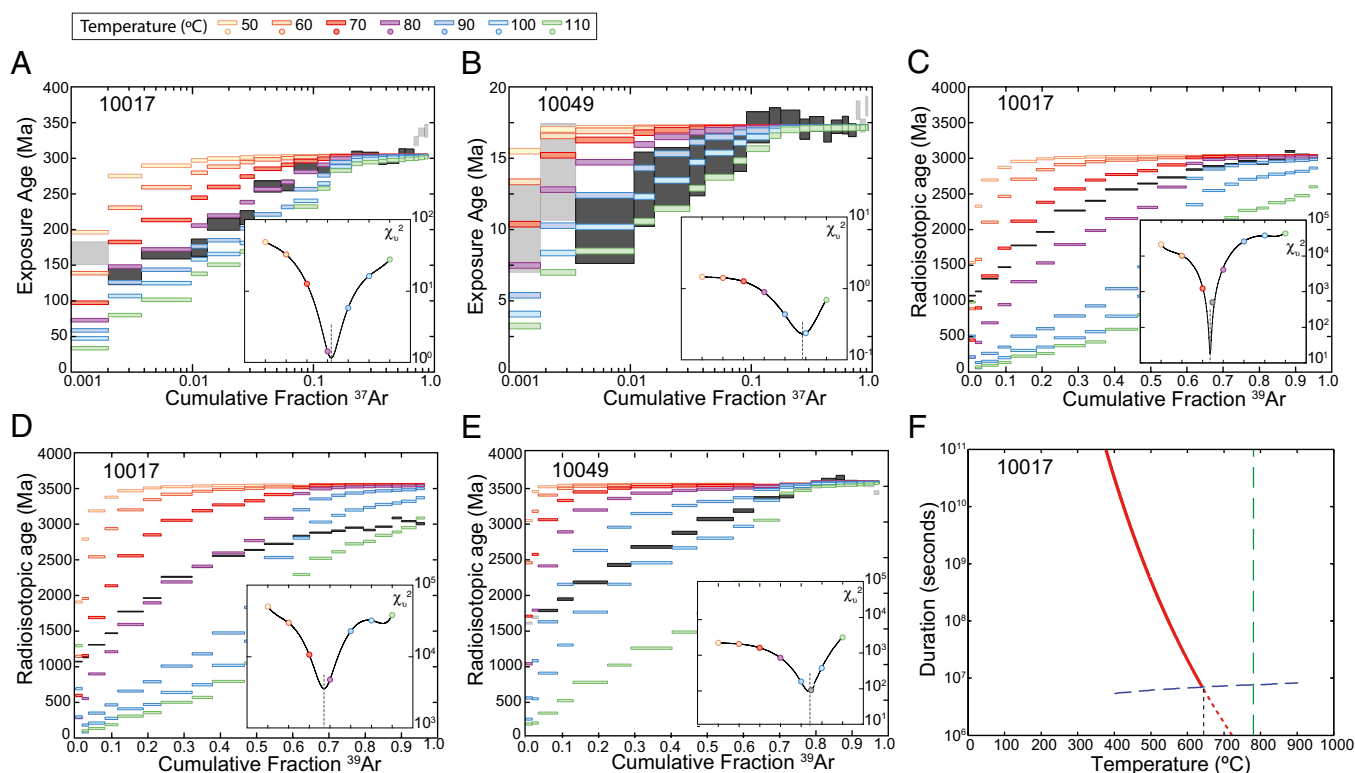


**Fig. 3.** Radiogenic $^{40}$Ar and cosmogenic $^{38}$Ar thermochronometry of whole-rock mare basalts 10017 and 10049. Production and diffusion of $^{38}$Ar$_{cos}$ for 10017 (*A*) and 10049 (*B*). The observed exposure ages ± 1 SD (gray boxes) are plotted against the cumulative release fraction of $^{37}$Ar. $^{38}$Ar$_{cos}$ was produced in situ while the rocks were exposed at the surface of the Moon. The colored steps are model release spectra calculated using the multiphase, multidomain model (model parameters are provided in *SI Appendix*) for the production and diffusion of $^{38}$Ar$_{cos}$, assuming the rocks were subjected to various constant effective daytime temperatures ranging from 50 to 110 °C during the last 303.1 Ma for 10017 or during the last 17.2 Ma for 10049 (i.e., $^{38}$Ar$_{cos}$ is produced continuously over this duration, whereas diffusion occurs only over half of this period during elevated daytime temperatures). (*Insets*) Reduced $\chi^2$ fit statistic for each model, identifying ~80 °C as the best-fit effective mean temperature for 10017 and ~95 °C as that for 10049. The diffusion of $^{40}$Ar* due to solar heating for 10017 is shown, calculated assuming the K/Ar system was reset at 3.03 Ga (*C*) or 3.56 Ga (*D*) (symbols and model parameters are the same as in *A*). (*E*) Diffusion of $^{40}$Ar* due to solar heating, calculated assuming the crystallization age is 3.56 Ga (symbols and model parameters are the same as in *B*). (*F*) Duration-temperature conditions required to cause >95% loss of $^{40}$Ar* from the most retentive plagioclase domains in 10017 during the proposed 3.0-Ga thermal event (red curve). The dashed blue curve predicts the time required to cool diffusively from an initial temperature, *T*, to <100 °C in the center of a 6-m-thick ejecta blanket. The intersection of this curve with the solid curve gives the peak temperature that would explain the Ar data under this scenario. The green dashed line represents the Curie temperature of kamacite (780 °C).

Our analyses confirm that like other Apollo group A basalts (32), 10049 has a weighted average $^{40}Ar/^{39}Ar$ plateau age of $3,556 \pm 8$ Ma [uncertainty is 1 SD; uncertainty in the decay constant and age of the fluence monitor is excluded (33)]. However, 10017's $^{40}Ar/^{39}Ar$ plateau age of $3,037 \pm 7$ Ma is ~600 My younger than its crystallization age (34). Our thermochronological calculations suggest that 10017 may have been heated to several hundred °C at ~3.05 Ga. Although this event may have partially remagnetized or demagnetized low blocking temperature grains in this rock (depending on whether a field was present at this time), many of these grains would have subsequently been demagnetized during zero-field residence on the lunar surface over the intervening 3 Ga and during residence in our laboratory's shielded room. As has been inferred for many other Apollo 11 basalts (7, 35), both 10017 and 10049 also apparently experienced modest gas loss due to solar heating over the last $304.7 \pm 2.0$ Ma and $17.5 \pm 0.1$ Ma, respectively. In particular, numerical models of simultaneous production and diffusion of both radiogenic $^{40}Ar$ and cosmogenic $^{38}Ar$ indicate that sample 10049 only experienced temperatures in excess of the ambient crustal conditions because it was exposed near the lunar surface.

## Implications for the Power Source of the Lunar Dynamo

Large impacts have the potential to unlock the Moon from synchronous rotation (36), such that the resulting differential motion between the librating mantle and core could generate a dynamo lasting for up to $10^4$ y (10). It is estimated that this can only occur for impactors that are larger than that required to produce a crater with a diameter of ~300 km (assuming an Earth-Moon distance of 25 Earth radii) (36). The youngest such basin is Orientale, which formed at 3.73 Ga and marks the end of the Early Imbrian epoch (37, 38). Because this event occurred ~160 Ma before the Late Imbrian eruption of 10017 and 10049, this likely excludes unlocking from synchronous rotation as a field source at 3.6 Ga.

Smaller impacts that are insufficient to unlock the Moon from synchronous rotation could still generate a mechanical dynamo by inducing longitudinal free librations (10). However, it is estimated that this was only possible while the Earth-Moon separation was <~40 Earth radii. Orbital history models constrained by geological evidence for the past 0.6 Ga (39, 40) suggest that the Earth-Moon separation was 37–44 Earth radii at 3.6 Ga, whereas uniformly scaled models give a range of 47–51 Earth radii (41). Therefore, the conditions for the existence of a libration dynamo might have been met during the eruption of the high-K basalts. Assuming this is the case, it is estimated that for the smallest Earth-Moon separation (37 Earth radii), an impact would have to produce a libration amplitude of at least 70° to trigger a libration dynamo (10). Using equations 1 and 6 in ref. 42, we determined the minimum impactor diameter [assuming a spherical bolide with uniform density of 3,500 kg·m$^{-3}$ and a lunar crustal density of 2,691 kg·m$^{-3}$ (43)] required to induce a libration dynamo as a function of impact location colatitude $\theta$, impact trajectory inclination relative to the lunar spin axis $\theta_v$, impact trajectory declination relative to the impact location $\phi_v$, and velocity $V$ (angles are defined in Fig. 4, *Inset*). Using the crater-scaling equation 5.6 in ref. 44, we calculated the corresponding crater size $D_{min}$. Using the impact velocity probability distribution $p(V)$ of Le Feuvre and Wieczorek (37), the probability distribution $p(\theta_v)$ of impact inclinations of Le Feuvre and Wieczorek (45), and the probability distribution of impact geographic colatitude $p(\theta)$ calculated from the relative cratering rate variations with latitude of Le Feuvre and Wieczorek (45); assuming a uniform distribution for impact declinations $\phi_v$; and ignoring the curvature of impact trajectories and acceleration due to the gravity of the Moon (which would tend to make trajectories more vertical and larger craters, and therefore reduce the effect on librations for a given crater size), we computed the probability
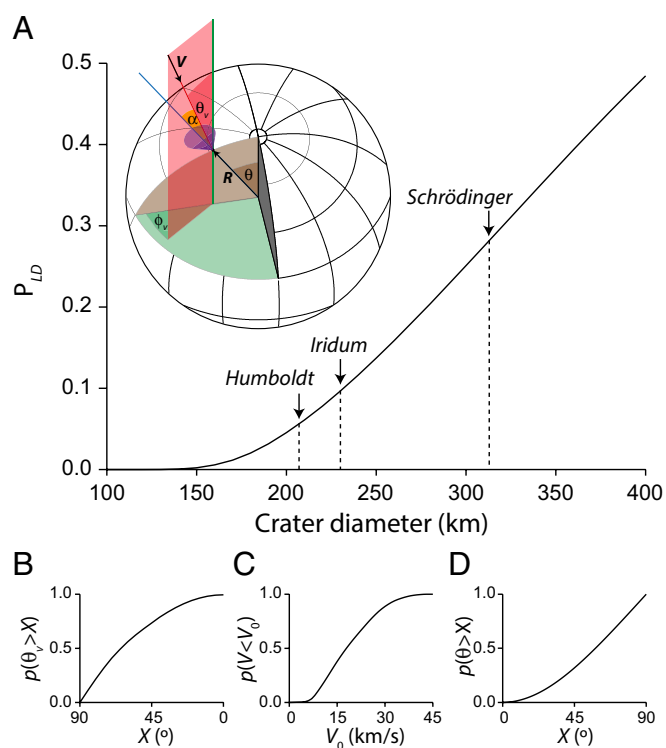


**Fig. 4.** (*A*) Probability to have induced a libration dynamo as a function of crater diameter. The diameters of the Late Imbrian crater Humboldt and Early Imbrian craters Iridum and Schrödinger are shown. (*Inset*) Impact geometry. The red line is the impact trajectory; the red surface is the plane defined by the impact trajectory and a line parallel to the lunar spin axis at the impact location. The blue line is the local vertical. The purple cone represents trajectories with $\alpha > 80°$. (*B*) Cumulative probability distribution for the inclination of the impact trajectory, $\theta_v$ (45). (*C*) Cumulative probability distribution for the impact velocity, $V$ (37). (*D*) Cumulative probability distribution for the impact location colatitude, $\theta$ (45).

$P_{LD}$ for an impact that produces a crater with diameter $D$ to induce a libration dynamo (Fig. 4):

$$P_{LD}(D) = \int \int \int \int \delta(\theta, \theta_v, \phi_v, V) \cdot p(\theta) \cdot p(\theta_v) \cdot p(\phi_v)$$
$$\cdot p(V) \cdot d\theta \cdot d\theta_v \cdot d\phi_v \cdot dV$$
$$\delta(\theta, \theta_v, \phi_v, V) = \begin{cases} 1 \text{ if } D_{min}(\theta, \theta_v, \phi_v, V) \leq D \\ 0 \text{ if } D_{min}(\theta, \theta_v, \phi_v, V) > D \end{cases}$$

where $\delta$ selects impact parameters that produce craters larger than the threshold value $D_{min}$. Impacts with incidence angles $\alpha > 80°$ [where $\alpha = \mathrm{acos}(RV/|R||V|)$; angle and vector definitions are provided in Fig. 4, *Inset*] are expected to produce elliptical craters (46). Because no such crater is known to have formed in the Late Imbrian era, we excluded these trajectories. We find that only craters with a diameter >~230 km have a probability to induce a libration dynamo >10% (Fig. 4). All the craters with a diameter >230 km identified in a recent Lunar Reconnaissance Orbiter survey* (47) are presented in *SI Appendix*, Table S1. The largest crater identified in the Late Imbrian era is Humboldt (38, 47); its diameter is ~207 km, which corresponds to a probability of ~6% to induce a libration dynamo. The youngest impacts that had

---

*Kadish SJ, et al. (2011), A global catalog of large lunar crater (≥20 KM) from the Lunar Orbiter Laser Altimeter, 42nd Lunar and Planetary Science Conference (March 7-11, The Woodlands, TX), Abstract 1006.

a significant (>25%) probability to trigger a libration dynamo are the Early Imbrian basins Schrodinger and Orientale (47)*.

The Late Imbrian 3.56-Ga crystallization age of the high-K basalts means that they are very likely too young to have been magnetized by an impact-driven dynamo. Furthermore, attributing the paleomagnetic records of 76535 at 4.2 Ga (6), 10020 at 3.7 Ga (7), and 10017 and 10049 at 3.6 Ga to an impact-driven dynamo would require a series of transient impact-driven dynamos. The fact that the 10017 and 10049 paleointensities are so similar to one another, as well to those of the 3.72-Ga basalt 10020 (7), argues strongly in favor of a stable lunar dynamo at least between 3.72 and 3.56 Ga. This lifetime is inconsistent with existing models of core convection, which have been unable to power a dynamo unambiguously after 4.1 Ga by thermal convection alone (48). Rather, these results support the possibility of a longer-lived power source for the lunar dynamo, such as precession (9) or thermochemical convection due to core crystallization, although impact-induced core dynamos could have operated earlier in lunar history.

Nevertheless, the high paleointensities of 10017 and 10049 [and 10020 (7)] still present a major challenge, given that all current lunar dynamo models are only thought to be capable of producing surface fields <15 μT (9). It currently remains unclear when the dynamo finally decayed.

1. Fuller M, Cisowski SM (1987) Lunar paleomagnetism. *Geomagnetism*, ed Jacobs JA (Academic, Orlando, FL), pp 307–455, Vol 2.
2. Wieczorek MA, et al. (2006) The constitution and structure of the lunar interior. *Reviews in Mineralogy and Geochemistry* 60:221–364.
3. Williams JG, Turyshev SG, Boggs DH, Ratcliff JT (2006) Lunar laser ranging science: Gravitational physics and lunar interior and geodesy. *Adv Space Res* 37(1):67–71.
4. Weber RC, Lin P-Y, Garnero EJ, Williams Q, Lognonné P (2011) Seismic detection of the lunar core. *Science* 331(6015):309–312.
5. Garcia RF, Gagnepain-Beyneix J, Chevrot S, Lognonné P (2011) Very preliminary reference Moon model. *Physics of the Earth and Planetary Interiors* 188(1–2):96–113.
6. Garrick-Bethell I, Weiss BP, Shuster DL, Buz J (2009) Early lunar magnetism. *Science* 323(5912):356–359.
7. Shea EK, et al. (2012) A long-lived lunar core dynamo. *Science* 335(6067):453–456.
8. Williams JG, Boggs DH, Yoder CF, Ratcliff JT, Dickey JO (2001) Lunar rotational dissipation in solid body and molten core. *J Geophys Res* 106(E11):27933–27968.
9. Dwyer CA, Stevenson DJ, Nimmo F (2011) A long-lived lunar dynamo driven by continuous mechanical stirring. *Nature* 479(7372):212–214.
10. Le Bars M, Wieczorek MA, Karatekin O, Cébron D, Laneuville M (2011) An impact-driven dynamo for the early Moon. *Nature* 479(7372):215–218.
11. Fuller M (1998) Lunar magnetism—A retrospective view of the Apollo sample magnetic studies. *Phys Chem Earth* 23(7-8):725–735.
12. Runcorn SK (1996) The formation of the lunar core. *Geochim Cosmochim Acta* 60(7):1205–1208.
13. Runcorn SK, et al. (1970) Magnetic properties of Apollo 11 lunar samples. *Proceedings of the Apollo 11 Lunar Science Conference held 5–8 January, 1970 in Houston, TX. Volume 3: Physical Properties*, ed AA Levinson (New York, Pergamon Press), pp 2369–2387.
14. Stephenson A, Runcorn SK, Collinson DW (1977) Paleointensity estimates from lunar samples 10017 and 10020. *Lunar Science Conference, 8th, (Houston, TX, March 14–18, 1977) Proceedings*. Vol 1. (A78-41551 18–91) (Pergamon Press, Inc., New York), pp 679–687.
15. Sugiura N, Strangway DW, Pearce GW (1978) Heating experiments and paleointensity determinations. *Lunar and Planetary Science Conference, 9th (Houston, TX, March 13–17, 1978) Proceedings*. Vol 3. (A79-39253 16-91) (Pergamon Press, Inc., New York), pp 3151–3163.
16. Hoffman KA, Baker JR, Banerjee SK (1979) Combining paleointensity methods: A dual-valued determination on lunar sample 10017,135. *Physics of the Earth and Planetary Interiors* 20:317–323.
17. Fuller M, Meshkov E, Cisowski CS (1979) On the natural remanent magnetism of certain mare basalts. *Lunar and Planetary Science Conference, 10th, (Houston, TX, March 19-23, 1979). Proceedings. Vol 3*. (A80-23677 08-91) (Pergamon Press, Inc., New York), pp 2211–2233.
18. Cournède C, Gattacceca J, Rochette P (2012) Magnetic study of large Apollo samples: Possible evidence for an ancient centered dipolar field on the Moon. *Earth Planet Sci Lett* 331-332:31–42.
19. Gattacceca J, Rochette P (2004) Toward a robust normalized magnetic paleointensity method applied to meteorites. *Earth Planet Sci Lett* 227(3–4):377–393.
20. Grove TL, Beaty DW (1980) Classification, experimental petrology and possible volcanic histories of the Apollo 11 high-K basalts. *Lunar and Planetary Science Conference, 11th, (Houston, TX, March 17–21, 1980) Proceedings*. Vol 1. (A82-22251 09-91) (Pergamon Press, New York), pp 149–177.
21. Beaty DW, Albee AL (1978) Comparative petrology and possible genetic relations among the Apollo 11 basalts. *Lunar and Planetary Science Conference, 9th, Houston, Tex., March 13–17, 1978, Proceedings. Volume 1. (A79-39107 16–91)* (New York, Pergamon Press, Inc.), pp 359–463.
22. Garrick-Bethell I, Weiss BP (2010) Kamacite blocking temperatures and applications to lunar magnetism. *Earth Planet Sci Lett* 294(1–2):1–7.
23. Dunlop DJ, Ozdemir O (1997) *Rock Magnetism: Fundamentals and Frontiers* (Cambridge Univ Press, New York), p 573.
24. Hood LL, Artemieva NA (2008) Antipodal effects of lunar basin-forming impacts: Initial 3D simulations and comparisons with observations. *Icarus* 193(2):485–502.
25. Pearce GW, Strangway DW (1972) Cause of secondary magnetization in lunar samples. *Apollo 16 Preliminary Science Report, NASA Special Publication SP-315*, eds Brett R, et al. (National Aeronautics and Space Administration, Houston), pp 7.55–7.58.
26. Tauxe L, Staudigel H (2004) Strength of the geomagnetic field in the Cretaceous Normal Superchron: New data from submarine basaltic glass of the Troodos Ophiolite. *Geochemistry, Geophysics, Geosystems*, 10.1029/2003GC000635.
27. Gattacceca J, et al. (2010) Can the lunar crust be magnetized by shock: Experimental groundtruth. *Earth Planet Sci Lett* 299(1–2):42–53.
28. Weiss BP, et al. (2010) Paleomagnetism of impact spherules from Lonar crater, India and a test for impact-generated fields. *Earth Planet Sci Lett* 298(1–2):66–76.
29. Louzada KL, et al. (2008) Paleomagnetism of Lonar impact crater, India. *Earth Planet Sci Lett* 275(3-4):309–319.
30. Dunlop DJ, Argyle KS (1997) Thermoremanence, anhysteretic remanence, and susceptibility of submicron magnetites: Nonlinear field dependence and variation in grain size. *J Geophys Res* 102:20199–20210.
31. Student (1908) The probable error of a mean. *Biometrika* 6(1):1–25.
32. Snyder GA, Lee D-C, Taylor LA, Halliday AN, Jerde EA (1994) Evolution of the upper mantle of the Earth's Moon: Neodymium and strontium isotopic constraints from high-Ti mare basalts. *Geochim Cosmochim Acta* 58(21):4795–4808.
33. Renne PR, Balco G, Ludwig K, Mundil R, Min K (2011) Response to the Comment by W. H. Schwarz et al. on "Joint determination of 40K decay constants and 40Ar*/40K for the Fish Canyon sanidine standard, and improved accuracy for 40Ar/39Ar geochronology" by P. R. Renne et al. (2010). *Geochim Cosmochim Acta* 75(17):5097–5100.
34. Papanastassiou DA, Depaolo DJ, Wasserburg GJ (1977) Rb-Sr and Sm-Nd chronology and genealogy of mare basalts from the Sea of Tranquility. *Lunar Science Conference, 8th, (Houston, TX, March 14–18, 1977) Proceedings*. Vol 2. (A78-39101 18-91) (Pergamon Press, Inc., New York), pp 1639–1672.
35. Turner G (1971) $^{40}$Ar-$^{39}$Ar ages from the lunar maria. *Earth Planet Sci Lett* 11(1–5):161–191.
36. Wieczorek MA, Le Feuvre M (2009) Did a large impact reorient the Moon? *Icarus* 200(2):358–366.
37. Le Feuvre M, Wieczorek MA (2011) Nonuniform cratering of the Moon and a revised crater chronology of the inner Solar System. *Icarus* 214(1):1–20.
38. Wilhelms DE (1987) *The Geologic History of the Moon* (US Department of the Interior, Washington, DC), p 302.
39. Williams GE (2000) Geological constraints on the Precambrian history of Earth's rotation and the Moon's orbit. *Rev Geophys* 38(1):37–59.
40. Walker JCG, et al. (1983) Environmental evolution of the Archean-Early Proterozoic Earth. *Earth's Earliest Biosphere: Its Origin and Evolution*, ed Schopf JW (Princeton Univ Press, Princeton), pp 260–290.
41. Touma J, Wisdom J (1994) Evolution of the Earth-Moon system. *Astron J* 108(5):1943–1961.
42. Peale SJ (1975) Dynamical consequences of meteorite impacts on the Moon. *J Geophys Res* 80(35):4939–4946.
43. Huang Q, Wieczorek MA (2012) Density and porosity of the lunar crust from gravity and topography. *J Geophys Res* 117:E05003.1–E05003.9.
44. Stöffler D, Ryder G, Ivanov BA, Artemieva NA (2006) Cratering history and lunar chronology. *Reviews in Mineralogy and Geochemistry* 60:519–526.
45. Le Feuvre M, Wieczorek MA (2008) Nonuniform cratering of the terrestrial planets. *Icarus* 197(1):291–306.
46. Bottke WF, Love SG, Tytell D, Glotch T (2000) Interpreting the elliptical crater populations on Mars, Venus and the Moon. *Icarus* 145(1):108–121.
47. Head JW, 3rd, et al. (2010) Global distribution of large lunar craters: Implications for resurfacing and impactor populations. *Science* 329(5998):1504–1507.
48. Stegman DR, Jellinek AM, Zatman SA, Baumgardner JR, Richards MA (2003) An early lunar core dynamo driven by thermochemical mantle convection. *Nature* 421(6919):143–146.

# Supporting Information (SI) Appendix
# Persistence and origin of the lunar core dynamo

Clément Suavet, Benjamin P. Weiss, William S. Cassata, David L. Shuster, Jérôme Gattacceca, Lindsey Chan, Ian Garrick-Bethell, James W. Head, Timothy L. Grove, and Michael D. Fuller

## 1. Previous paleomagnetic studies of high-K mare basalts

During the Apollo era, paleomagnetic studies were carried out on at least six high-K basalts: 10017, 10022, 10024, 10049, 10057, and 10069. 10022 was thermally demagnetized (49), but the lack of published directional data precludes the identification of magnetization components. 10024 was found to carry an intense soft overprint and a higher coercivity component blocked from 5 to at least 50 mT, but spurious demagnetization effects prevented a detailed characterization of the latter (1). Similarly, 10057 was found to contain a soft overprint and a higher coercivity component from 9 to >18 mT, but a high-quality paleointensity value could not be obtained because the sample was not fully demagnetized (50, 51). 10069 was only demagnetized to <7 mT before thermal demagnetization was attempted, at which point the sample irreversibly altered (49).

Because so many lunar rocks have poor magnetic recording properties (52), we decided to focus on two samples that appeared to be unusually well-behaved during previous AF demagnetization experiments: 10017 and 10049 (Fig. S1 and Table S6). The natural remanent magnetization (NRM) of 10017 was studied by three groups (13-16). Initial reports identified a directionally stable magnetization component during alternating field (AF) demagnetization of subsample 10017,64 up to 50 mT (13). Further investigation of subsample 10017,27 isolated a directionally stable component of magnetization between 7.5 mT and 48 mT, for which a paleointensity of 70 µT was obtained using the anhysteretic remanent magnetization (ARM) method with a calibration factor $f' = 1.34$ (see Section 6) (14). Thermal demagnetization of subsample 10017,30 was attempted, but no paleointensity could be retrieved as its NRM was completely destroyed by heating to 300°C and decayed during AF demagnetization differently from a laboratory-induced thermoremanent magnetization (TRM) (15). These data were interpreted as indicating that its magnetization may not be a total TRM (15). However, subsequent thermal demagnetization experiments by Hoffman et al. (16) strongly suggested that 10017 alters irreversibly during heating at even these low temperatures. Hoffman et al. (16) also observed a remarkably stable magnetization in the coercivity range of 50-100 mT during AF demagnetization of subsample 10017,135 which yielded a Shaw paleointensity of 71 µT and an ARM paleointensity of 93 µT using a corrected factor $f'_{corr} = 0.94$ (16). Although these early studies suggest that 10017 is a promising candidate for renewed AF analyses, none of the these studies fully demagnetized the samples due to technical limitations, no mutually oriented samples were measured, and the NRM was not compared to pressure remanent magnetization (PRM, as an analog of shock remanent magnetization), viscous remanent magnetization (VRM), and isothermal remanent magnetization (IRM). Furthermore, detailed thermochronology and cooling history studies were not conducted.

Two mutually oriented samples of 10049 were previously studied: 10049,14.1 and 10049,14.3 (17). A unidirectional, origin-trending mid-coercivity component was identified between 20 and 50 mT for subsamples 14.1 and 14.3. Paleointensities of ~4 and ~10 µT, respectively, were determined using the residual REM method after demagnetization to 20 mT. Thermal methods were attempted but extensive sample alteration occurred.
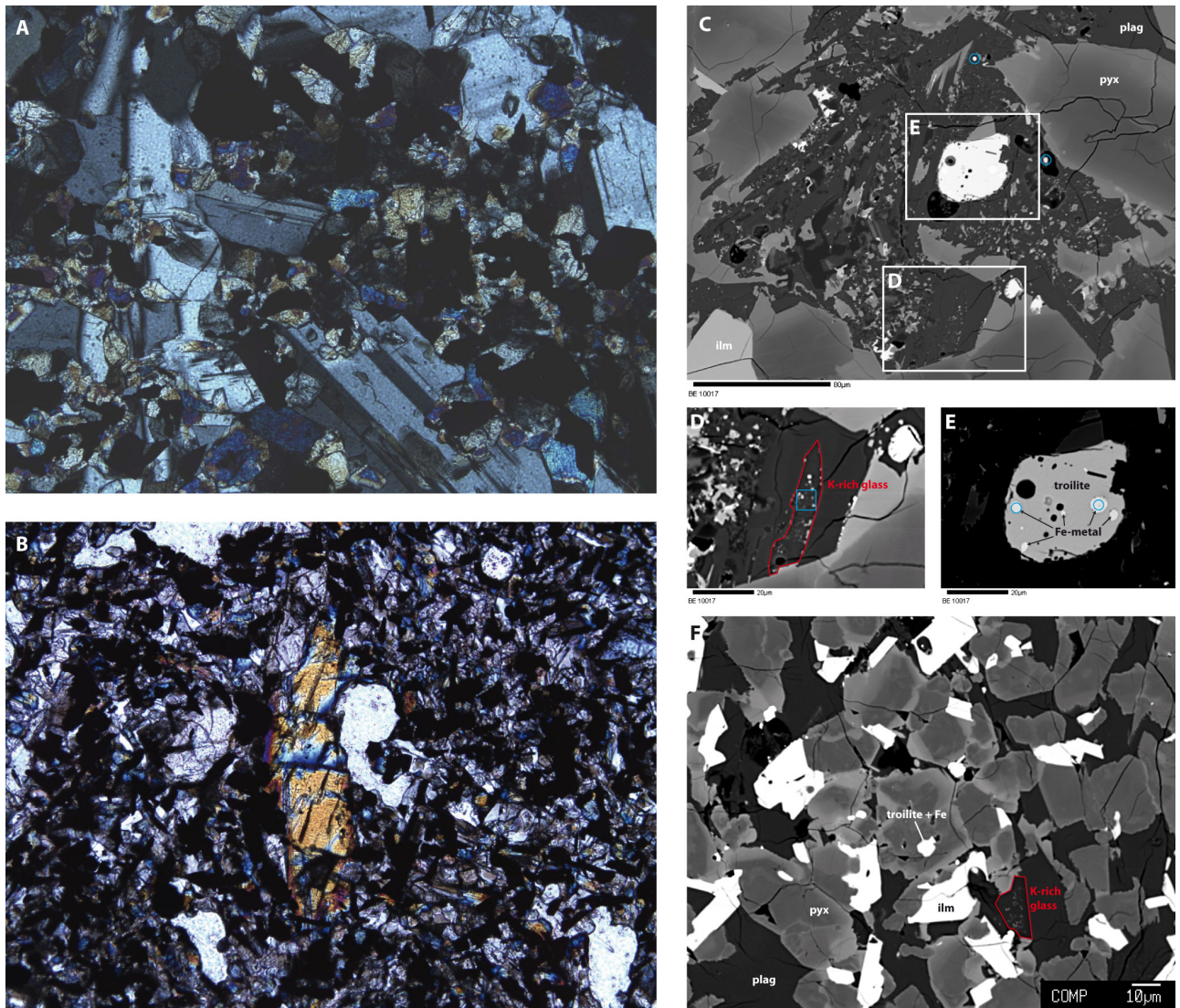
**Fig. S1.** (**A, B**) Photographs of 30 μm thin sections of 10017,62 (**A**) and 10049,40 (**B**) in transmitted light with crossed polarizers. Plagioclase is visible as light gray laths. Pyroxene is large phenocrysts displaying high order interference colors. The pictured areas are 2 mm wide. (**C-F**) BSEM images of 30 μm thin sections. (**C**) Context image showing plagioclase (plag), pyroxene (pyx), ilmenite (ilm), and K-rich glass in section 10017,62. Blue circles indicate microprobe spots. White boxes shows region magnified in (**D**) and (**E**). (**C**) Magnified image of K-rich glass and surrounding phases. (**E**) Magnified image of troilite-kamacite assemblages. (**F**) Context image showing plagioclase, pyroxene, ilmenite, troilite and iron assemblages, and K-rich glass in section 10049,40.

## 2. Sample preparation

Our paleomagnetic measurements were acquired on samples 10017,378 and 10049,102, which were chipped off from the non-space weathered interiors of parent samples 10017,15 and 10049,0 using a non-magnetic stainless steel hammer and chisel at the NASA Johnson Space Center (JSC). A recent investigation at JSC revealed that neither parent sample has been cut with a circular saw (which is suspected of having heated some lunar samples) and in fact 10049 has never been cut with a saw at all at JSC. The subsamples were shipped in a magnetically shielded case to the Massachusetts Institute of Technology (MIT) Paleomagnetism Laboratory (http://web.mit.edu/paleomag) and stored in a magnetically shielded (DC field <150 nT), class ~10,000 clean room for >6 months before the first measurements were performed. With the exception of 10017,378-10 and -11 described below, nearly all subsequent sample handling was performed in the magnetically shielded clean room at MIT. Microscopy and microprobe measurements were acquired on 30 μm thin sections of 10017,62 and 10049,40 (Fig. S1).

     Sample 10017,378 (5.95 g) was cut into 2 pieces labeled P1 (3.894 g) and P2 (1.829 g). P2 was then cut with a wire saw or broken into 10 subsamples: 378-1 (105 mg), fragment 378-1f (31

mg), 378-2 (241 mg), 378-3 (221 mg), 378-4 (201 mg), 378-5 (220 mg), 378-6 (133 mg), 378-7 (251 mg), 378-8 (199 mg), and 378-9 (41 mg). P1 was cut into 2 pieces: P1A (1.995 g) and P1B (1.800 g). P1A was stored for later studies. P1B was cut into 3 subsamples with a wire saw: 378-10 (407 mg), 378-11 (734 mg), and 378-12 (565 mg). All subsamples are mutually oriented except 378-1f. Sample 10049,102 (2.19 g) was cut into 3 mutually oriented subsamples: 102-1 (221.3 mg), 102-2 (307.8 mg) and 102-3 (47.2 mg).

Before measurements, the samples were glued to nonmagnetic GE 124 quartz disks with nonmagnetic cyanoacrylate cement. All samples were analyzed in the MIT Paleomagnetism Laboratory with the exception of 10017 subsamples 378-10 and 378-11 which were analyzed independently at the University of California (UC) Santa Cruz Paleomagnetism Laboratory. Before measurement, these samples were glued to non-magnetic plastic boxes with nonmagnetic cyanoacrylate cement.

## 3. Methods

At MIT, we conducted room temperature three-axis alternating field (AF) demagnetization using a 2G Enterprises Superconducting Rock Magnetometer 755 (sensitivity $\sim 1\times10^{-12}$ Am$^2$) equipped with a robotic sample handling system (53) (Figs. 1, S2 and S3). This method was chosen rather than thermal demagnetization because heating was shown to permanently alter samples (as previously observed for 10017; see Section 2). AF demagnetization also has the advantage of efficiently removing secondary low field IRM due to sample handling (3, 25), which is restricted to low coercivity grains but can be blocked up to the Curie point. However, acquisition of spurious ARM noise and gyroremanent magnetization (GRM) are two disadvantages of AF demagnetization (52, 54). To reduce spurious ARM noise, we made repeat AF applications (between 5-11 times depending on the field) and calculated the vector mean for each field level. Moment measurements were made after AF application along each of the three orthogonal axes to reduce the effects of GRM [following the Zijderveld-Dunlop method (6, 54)]. To rule out induced fields as a source of the measured magnetization, subsample 378-6 was measured with a different orientation from all other subsamples. NRM magnetization directions were characterized using principal component analysis (PCA) (55).

The two samples of 10017 analyzed at UC Santa Cruz were first demagnetized up to 99 mT with a Schonstedt tumbling AF demagnetizer. The samples were demagnetized 3-5 times at each AF level, and the results were averaged together to reduce noise. From 99-180 mT, the samples were 3-axis AF demagnetized and the Zijderveld-Dunlop method was used to reduce the effects of GRM. Above 99 mT, each AF level was repeated 3-5 times to reduce noise. All of these measurements were performed with a 2G Enterprises Superconducting Rock Magnetometer (sensitivity $\sim 1\times10^{-11}$ Am$^2$).
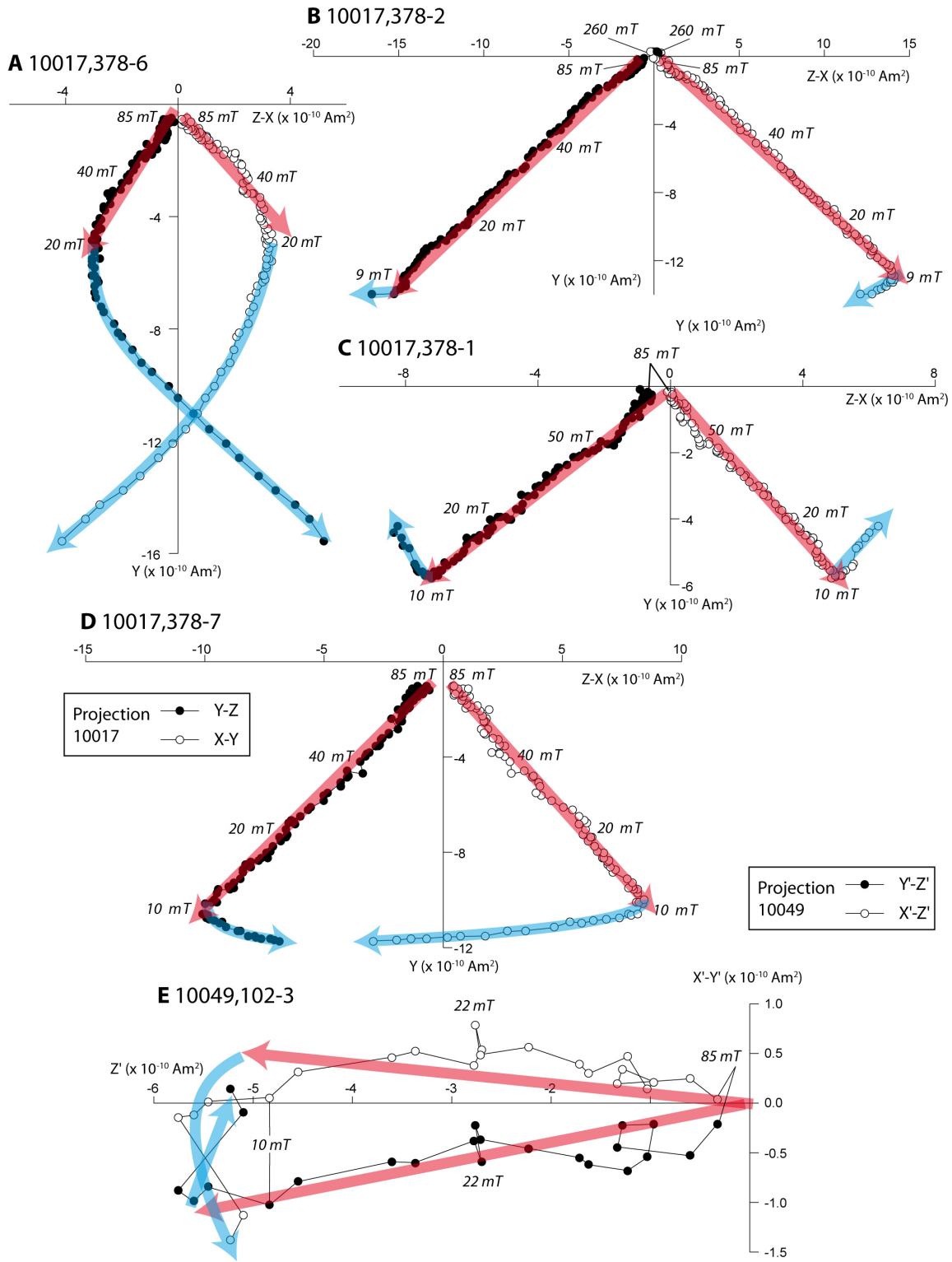
**Fig. S2.** AF demagnetization of additional subsamples of 10017 and 10049. Shown is a two-dimensional projection of the NRM vectors of subsamples 10017,378-1, 10017,378-2, 10017,378-6, 10017,378-7 and 10049,102-3 during AF demagnetization. Solid (open) symbols represent end points of magnetization projected onto the Y-Z (X-Y) planes for 10017, and onto the Y'-Z' (X'-Z') planes for 10049. Peak fields for selected AF steps are labeled in mT. Red arrows denote HC component directions determined from principal component analyses (PCA). The mass of each subsample is listed below the sample name. (**A**) Subsample 10017,378-6. (**B**) Subsample 10017,378-2. (**C**) Subsample 10017,378-1. (**D**) Subsample 10017,378-7. (**E**) Subsample 10049,102-3.
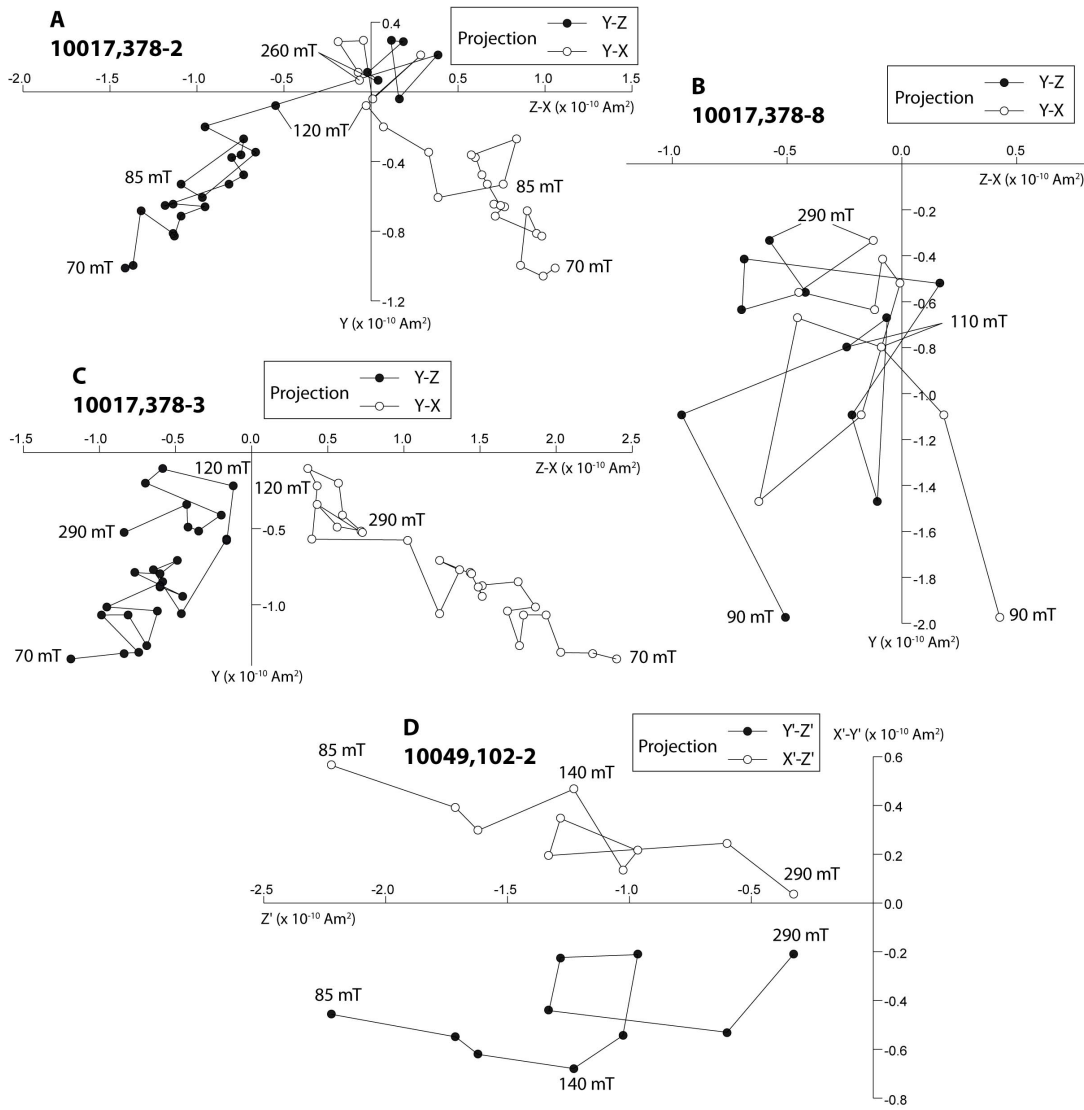
**Fig. S3.** High-field AF demagnetization. Shown is a two-dimensional projection of the NRM vector during AF demagnetization. Solid (open) symbols represent end points of magnetization projected onto the Y-Z (X-Y) planes for 10017, and onto the Y'-Z' (X'-Z') planes for 10049. Peak fields for selected AF steps are labeled in mT. (**A**) Subsample 10017,378-2. (**B**) Subsample 10017,378-8. (**C**) Subsample 10017,378-3. (**D**) Subsample 10049,102-2.

## 4. Paleointensity experiments

Following demagnetization, the samples were subjected to paleointensity experiments (Fig. S4 and Table S2). Although Thellier-Thellier heating experiments could potentially provide the best estimates for paleointensities of TRM, they involve heating the samples which alters the magnetic mineralogy, precluding accurate recovery of the paleointensity. Therefore, we used room-temperature methods that provide an estimate of the paleofield by comparing the demagnetization of the NRM with the demagnetization of a laboratory-induced magnetization (6, 56). The IRM method, in which the samples are submitted to a strong field up to the maximum coercivity of the HC component and AF demagnetized, gives an estimate of the paleointensity with the following formula:

$$\text{IRM paleointensity in } \mu T = (\Delta NRM/\Delta IRM) \times a$$

A typical value of $a = 3000$ was used (19). The ARM method, for which and ARM of known bias field is imparted and AF demagnetized, gives an estimate of the paleointensity with the following formula:

$$\text{ARM paleointensity in } \mu T = (\Delta NRM/\Delta ARM) / f \times \text{bias field}$$
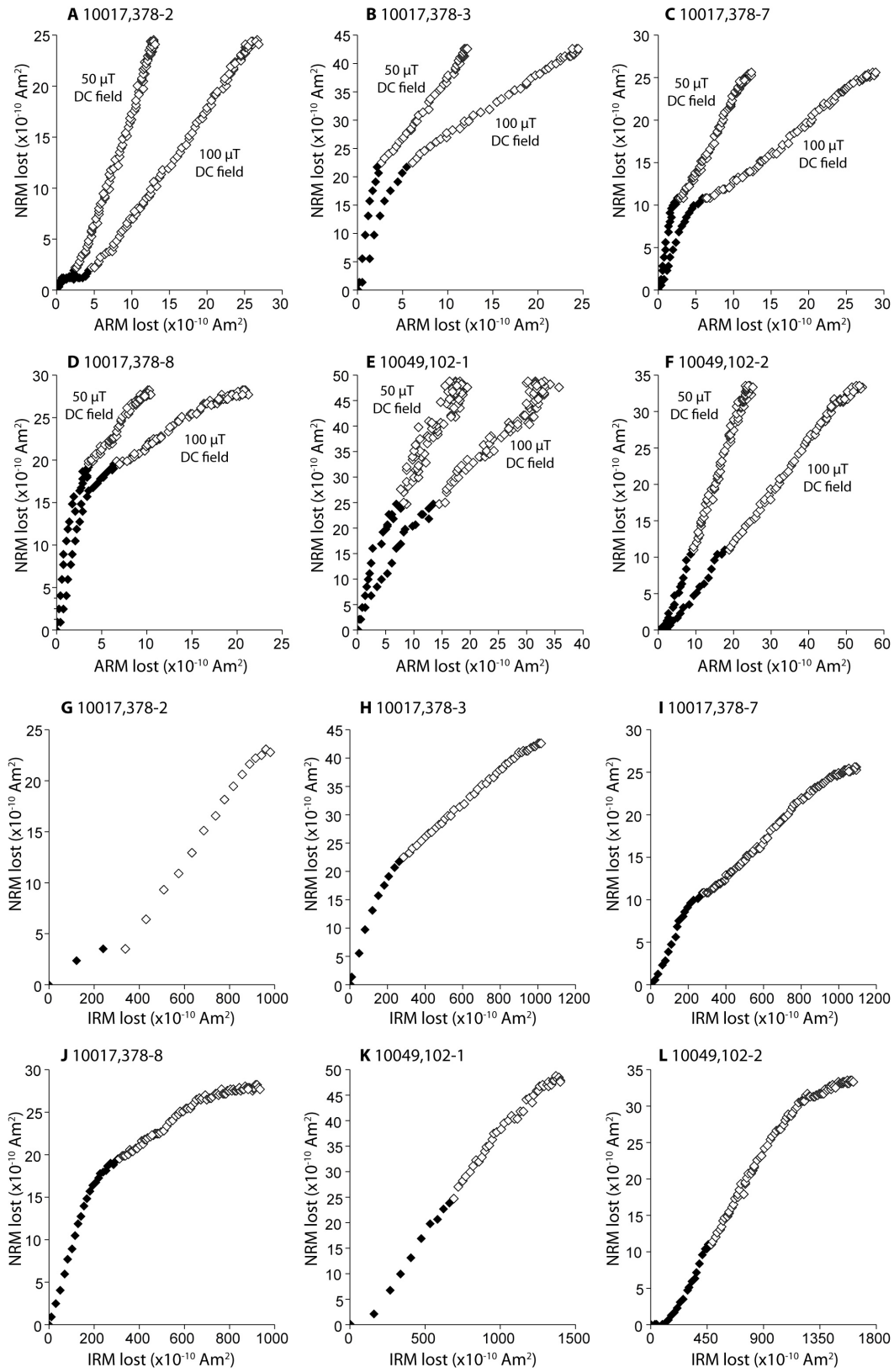
5

**Fig. S4.** Paleointensity experiments. AF demagnetization of NRM is plotted as a function of AF demagnetization of ARM acquired in laboratory DC bias fields of 50 µT, or 100 µT and AF field of 85 mT (**A-F**), or as a function of AF demagnetization of a strong field IRM (**G-L**). Data points from LC and HC components are represented with solid and open symbols, respectively. (**A**) Subsample 10017,378-2. (**B**) Subsample 10017,378-3. (**C**) Subsample 10017,378-7. (**D**) Subsample 10017,378-8. (**E**) Subsample 10049,102-1. (**F**) Subsample 10049,102-2. (**G**) Subsample 10017,378-2. (**H**) Subsample 10017,378-3. (**I**) Subsample 10017,378-7. (**J**) Subsample 10017,378-8. (**K**) Subsample 10049,102-1. (**L**) Subsample 10049,102-2.

6

The greatest source of uncertainty in this method is for the value of $f'$, as this factor is sample-dependent and not easily determined due to alteration during heating. We used $f' = 1.34$, similar to the value experimentally measured for 10017 by ref. (16) (see Section 1); most rocks have been observed to have $f'$ within a factor of 3-5 of this value (57-61). The resulting paleointensities were then corrected for sample magnetic anisotropy (see Section 10 and Table S3).

Using the AF demagnetization data from ref. (17), we computed the paleointensities for subsample 10049,14.3 using the same method. We obtained paleointensities of $22 \pm 6$ µT for the 20-50 mT coercivity range with the ARM method and ~32 µT for the 20-30 mT coercivity range with the IRM method. Subsample 10049,14.1 yielded paleointensities of ~11 µT for the 20-50 mT coercivity range with the IRM method. These values are significantly higher than the ~4 µT obtained by NRM/IRMs normalization reported by this study and used to make the argument that the lunar dynamo was not active during the formation of this rock. The difference between our results and the values reported comes from the fact that we used the REM' method (19) to calculate the paleointensity rather than total NRM/IRMs normalization. The newly computed values are within error of our new measurements (Table S2) given the uncertainty of the IRM and ARM methods.

## 5. Paleointensity fidelity experiments

The majority of lunar rocks exhibit nonideal behaviors during AF demagnetization, acquiring spurious remanence at high fields that can mask the underlying NRM and yield inaccurate paleointensity values (52). To determine the ability of 10017 and 10049 to record magnetic fields, we conducted artificial paleointensity experiments on subsamples 10017,378-8 and 10049,102-1 following ref. (52).
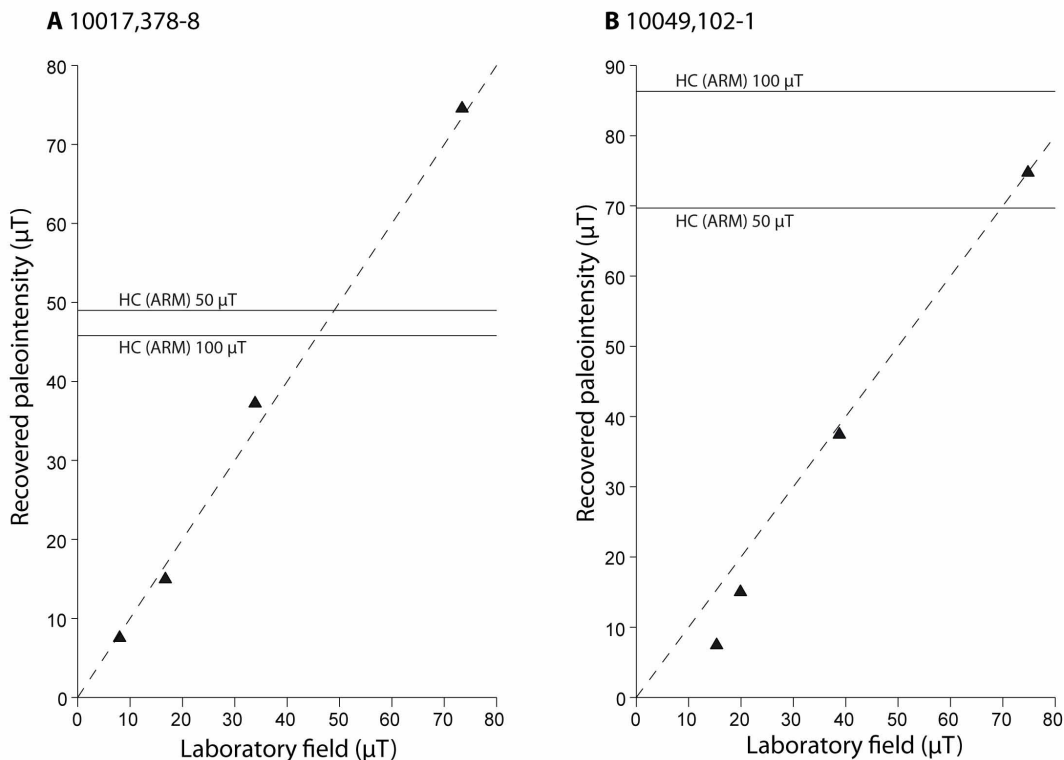


**Fig. S5.** Recovered paleointensities versus TRM-equivalent applied laboratory field (triangles). Perfect agreement is shown by dashed line of slope 1. Actual paleointensities for HC component of NRM using the ARM method with 100 µT and 50 µT bias fields are shown by horizontal lines. (**A**) Subsample 10017,378-8. (**B**) Subsample 10049,102-1.

We applied multiple ARMs using an AC field of 85 mT and DC bias fields of 10, 20, 50, and 100 µT, and carried out AF demagnetization after each ARM application. We then computed the

paleointensity using the same method as that used for the NRM: the moment lost at each AF step was compared to the ARM gained in a 200 µT DC field at the same AF step. We found that we could retrieve applied TRM-equivalent paleointensities in the range of the average observed NRM paleointensity (50-100 µT) (Table S4) with 1-10% accuracy (Fig. S5 and Table S4) for both samples.

## 6. Rock magnetism

The room-temperature hysteresis properties of subsamples 10017,378-3 and 10049,102-1 were measured with a PMC Vibrating Sample Magnetometer VSM with a peak field of 1 T (noise level of $10^{-9}$ Am$^2$) at Centre Européen de Recherche et d'Enseignement (CEREGE) in Aix-en-Provence, France. The high-field slope (between 1 and 0.95 T) of the hysteresis loop was used to estimate the contribution of paramagnetic and diamagnetic minerals and this contribution was subtracted from the loops to recover the ferromagnetic contribution. The results (Fig. S6 and Table S5) indicate ratios of saturation remanence to saturation magnetization ($M_{rs}/M_s$) and coercivity of remanence to coercivity ($B_{cr}/B_c$) characteristic of a mean grain size in the multidomain range (62).
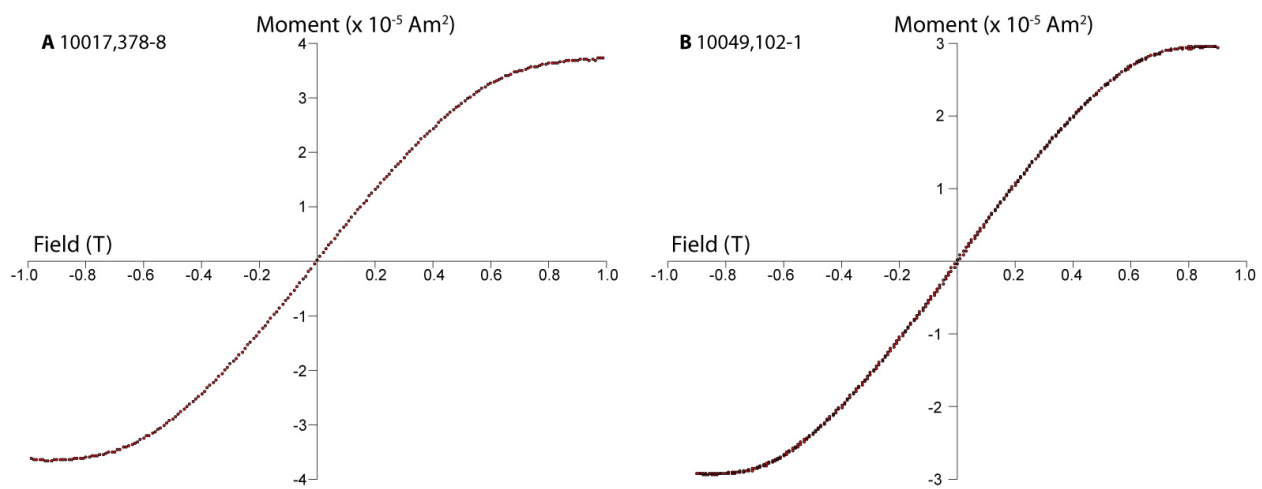


**Fig. S6.** Room temperature hysteresis loops after subtraction of paramagnetic and diamagnetic contributions. Shown is the sample moment as a function of applied field. (**A**) Subsample 10017,378-8. (**B**) Subsample 10049,102-1.

Samples 10017,378-1 and 10049,102-1 were given stepwise ARM in increasing DC bias fields from 0.2 to 2 mT in a peak AC field of 200 mT (Fig. S7) to infer the degree of magnetostatic interactions in the samples (63). Following ARM acquisition, the ARM was then stepwise AF demagnetized; the samples were then given an IRM in a field of 200 mT that was also subsequently stepwise AF demagnetized. Back field experiments were also conducted in which a 1 T IRM was applied and then oppositely oriented fields of progressively increasing strength were applied until the sample moment reached zero. Sample 10017,378-2 and 10049,102-1 were also subjected to progressive IRM acquisition (Fig. S8). IRM acquisition, back field IRM, and AF demagnetization of IRM data are indicators of the coercivity spectrum of the sample. The field at which IRM acquisition and AF demagnetization of IRM curves intersect is indicative of $B_{cr}$, as is the back field value at which the remanence goes to zero. The comparison of normalized curves of AF demagnetization of ARM and IRM (Fig. S9) constitutes the Lowrie-Fuller test, an indicator of grain size and stress state (64, 65). The Lowrie-Fuller test indicates that 10017 exhibits high-field-type (IRM more stable than ARM) behavior, consistent with kamacite (Table S7) in the pseudo single domain to multidomain size range. IRM acquisition and demagnetization data (Fig. S8) and $B_{cr}$ values are consistent with the presence of multidomain kamacite [and not the high coercivity mineral tetrataenite (66, 67)] as the dominant ferromagnetic phase in 10017 and 10049. ARM susceptibility values (Fig. S7) indicate that 10017 and 10049 contain moderately interacting multidomain grains.
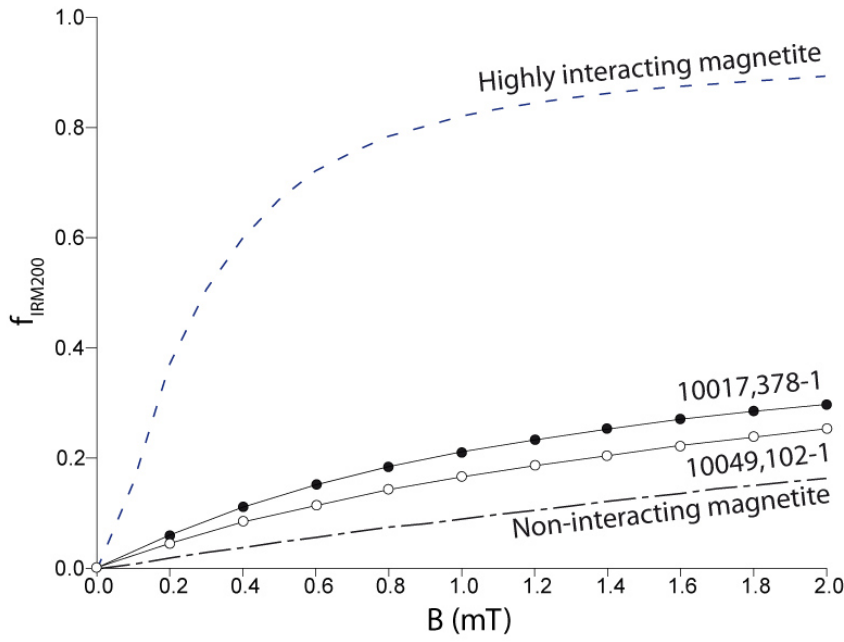
**Fig. S7.** ARM acquisition experiments on samples 10017,378-1 (black circles) and 10049,102-1 (white circles). Shown is the ratio of ARM and acquired in a 200 mT AC field and IRM acquired in a 200 mT DC field, as a function of DC bias field. Upper dotted curve is that of highly interacting chiton tooth magnetite and lower dotted curve is non-interacting magnetite in magnetotactic bacteria (116).
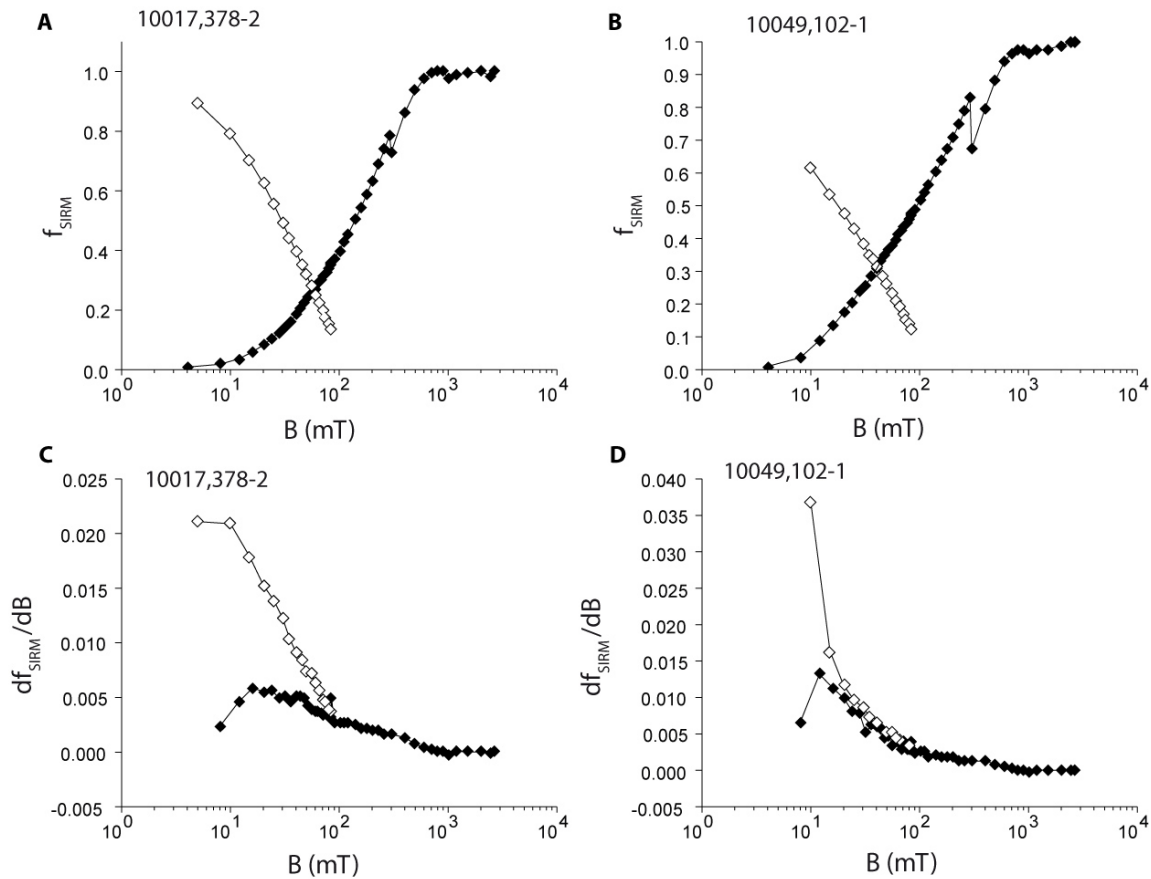


**Fig. S8.** IRM acquisition and demagnetization experiments. $f_{SIRM}$ = fraction of IRM acquired/remaining. **(A)** IRM acquisition and AF demagnetization of IRM for subsample 10017,378-2. Both curves are normalized to the highest-field IRM value. **(B)** IRM acquisition and AF demagnetization of IRM for subsample 10049,102-1. Both curves are normalized to the highest-field IRM value. **(C)** Field derivative of AF demagnetization of IRM and of IRM acquisition for subsample 10017,378-2. **(D)** Field derivative of AF demagnetization of IRM and of IRM acquisition for subsample 10049,102-1.

9

**Fig. S9.** AF demagnetization of samples 10017,378-3 (**G, H**) and 10049,102-1 (**I, J**). Shown is the intensity of NRM during AF demagnetization compared to that of various forms o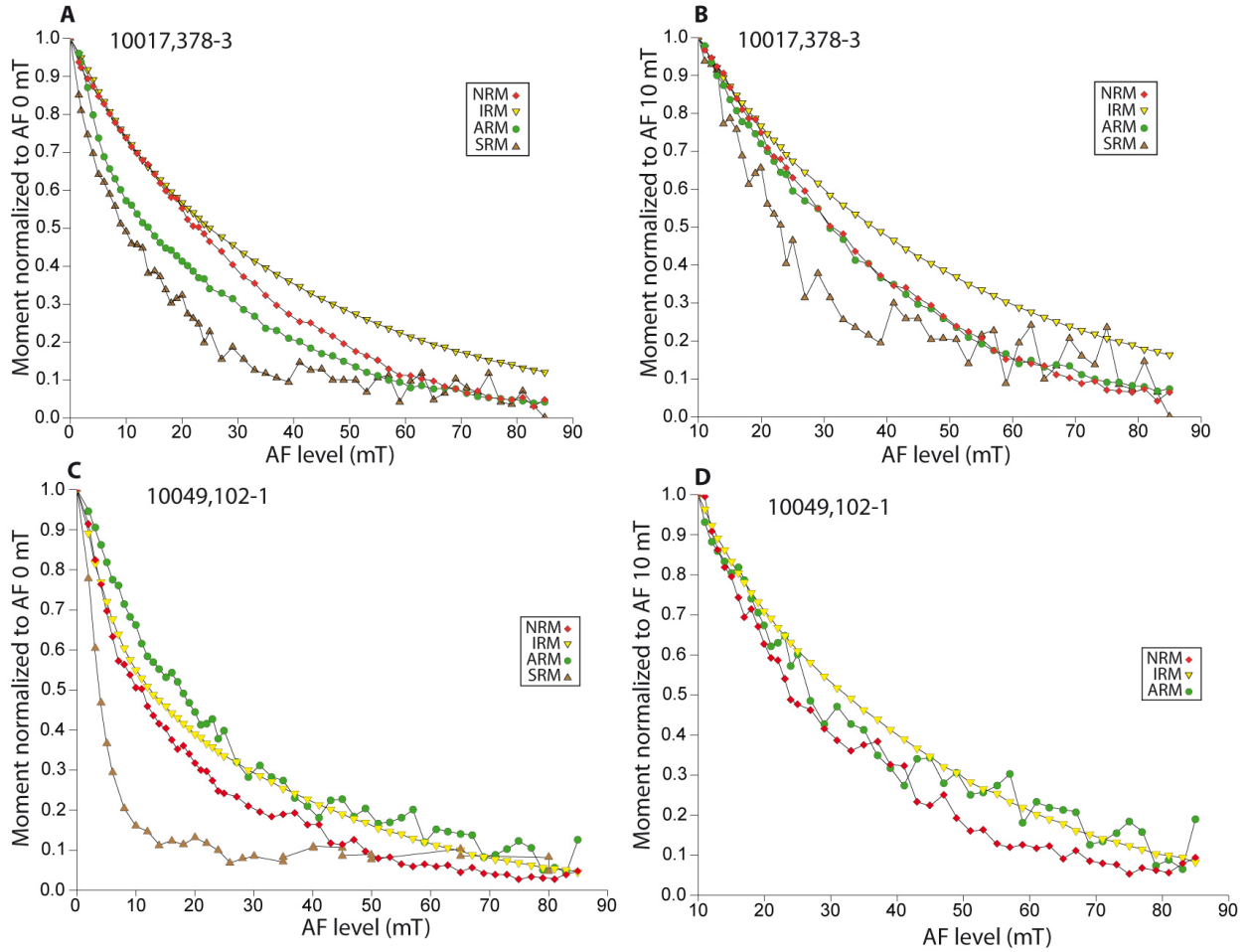f laboratory-induced magnetization: ARM acquired in a 85 mT AC field and 0.2 mT DC bias field, IRM acquired in a 200 mT field, and PRM acquired in a field of 0.8 mT at a pressure of 2 GPa. (**G, I**) Magnetization normalized to initial (undemagnetized) step to emphasize comparison between LC component and laboratory magnetizations. (**H, J**) Magnetization normalized to 10 mT AF step to emphasize comparison between HC component and laboratory magnetizations.

## 7. PRM experiments

PRM experiments were conducted at CEREGE. The subsamples were placed in a Teflon cup filled with polyethylsiloxane fluid (68) and inserted in a non-magnetic pressure vessel. A coil was mounted around the vessel to generate a magnetic field of 0.8 mT. The sample was pressurized in this field using a press and then the pressure was slowly released over ~1 min. The sample was then AF demagnetized. These experiments were conducted at 0.2, 0.6, 1.2, 1.6 and 2.0 GPa for 378-3 and at 0.8, 1.2, 1.6 and 2 GPa for 102-1. We observed a roughly linear relationship between the acquired total PRM intensity and pressure (Fig. S10). We used linear regressions to estimate both the total PRM and the PRM demagnetized to 10 mT that would be produced by a 5 GPa shock in a 0.8 mT field (Fig. S10). These values allow us to calculate a lower limit for the paleofield intensity that would have been necessary to produce the observed LC and HC components (e.g., NRM blocked above and below AF 10 mT) assuming they are 5 GPa PRMs:

$$\text{Paleofield (LC)} = \text{lab field} \times [\text{NRM} - \text{NRM(AF 10 mT)}]/[\text{PRM(5 GPa)} - \text{PRM(5 GPa, 10 mT)}]$$
$$\text{Paleofield (HC)} = \text{lab field} \times \text{NRM(AF 10 mT)}/\text{PRM(5 GPa, 10 mT)}$$

where NRM(AF 10 mT) and PRM(5 GPa, 10 mT) are the NRM and 5 GPa PRM after demagnetization to 10 mT, respectively.
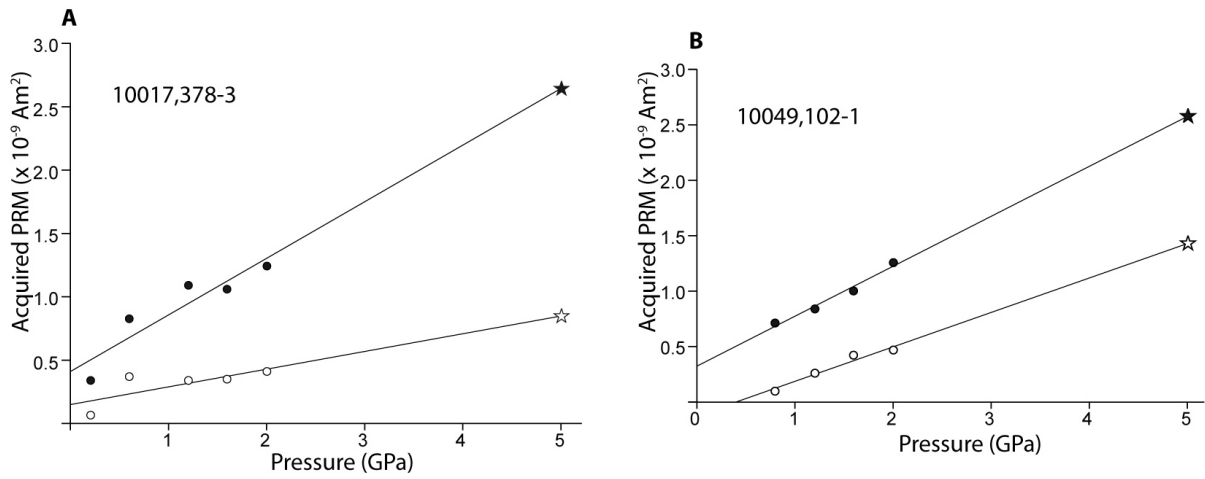
**Fig. S10.** PRM acquisition experiments. Shown is the PRM intensity as a function of applied pressure (acquired in a 0.8 mT field. Empty circles are PRM normalized by the AF 0 mT step and filled circles are normalized by the AF 10 mT step. Solid lines are best fit linear regression to data. Extrapolation yields a maximum estimate of the PRM acquired at 5 GPa (stars). (**A**) Subsample 10017,378-3. (**B**) Subsample 10049,102-1.

## 8. Magnetic viscosity experiments

We seek to determine whether (a) the NRMs of 10017 and 10049 were contaminated by VRM acquired during their 40 year exposure to the geomagnetic field since return to Earth and (b) how much of this VRM subsequently decayed during storage in our shielded room prior to our NRM measurements. With this goal, samples 10017,378-3 and 10049,102-2 were placed in the Earth's magnetic field (~50 µT) for 57 and 26 days, respectively. The samples were returned to the shielded room (<150 nT) and their magnetizations repeatedly measured over a period of ~10 days. This experiment was repeated on the same two samples with acquisition times of 6 days and 5 days, respectively.

We found that the samples acquired weak VRM: sample 10017 acquired $7.33 \times 10^{-11}$ Am$^2$ after 6 days and $1.06 \times 10^{-10}$ Am$^2$ after 57 days, equivalent to 1.9% and 2.7% of the NRM, respectively. Sample 10049 acquired $7.94 \times 10^{-11}$ Am$^2$ after 5 days and $1.07 \times 10^{-10}$ Am$^2$ after 26 days, equivalent to 2.3% and 3.1% of the NRM, respectively. The acquisition rate we measured – ~$5 \times 10^{-8}$ Am$^2$/kg/log(s) – is higher than the ~$7 \times 10^{-8}$ Am$^2$/kg/log(s) (normalized to the Earth's field) obtained in ref. (17). However their experiment was very different: the acquisition was measured over a period of 1.5 hours only in a 1 mT field. We observed that over the time period of our experiments, the decay rates for both samples was approximately linear in log(time), and the magnetizations returned toward the initial direction. From these experiments, we can estimate the VRM acquisition rate in the Earth's magnetic field and the decay rate of the VRM in a shielded environment: assuming that acquisition and decay rates can be approximated as linear in log(time), these results give an acquisition rate of $3.0 \times 10^{-11}$ Am$^2$ per log(s) and a decay rate of at least -$1.28 \times 10^{-11}$ Am$^2$ per log(s) for 10017, and an acquisition rate of $3.0 \times 10^{-11}$ Am$^2$ per log(time) unit and a decay rate of -$1.59 \times 10^{-11}$ Am$^2$ per log(s) for 10049.

The measured acquisition rate permits an estimation of the magnitude of the VRM acquired in the geomagnetic field since arrival on Earth 40 years ago assuming the samples were in fixed positions with respect to the field during this period [log(time) = 9.1 log(s)] (Fig. S11). Because the actual functional form of the VRM decay rate is unknown for periods outside the timescale of our experiment, as a minimum bound, we fit the data assuming a linear rate in log(time). The measured decay rate was then used to estimate how much of this 40-year VRM subsequently would have decayed after ~6 months (for 10017) and ~15 months (for 10049) in the shielded room prior to our first NRM measurements.

11
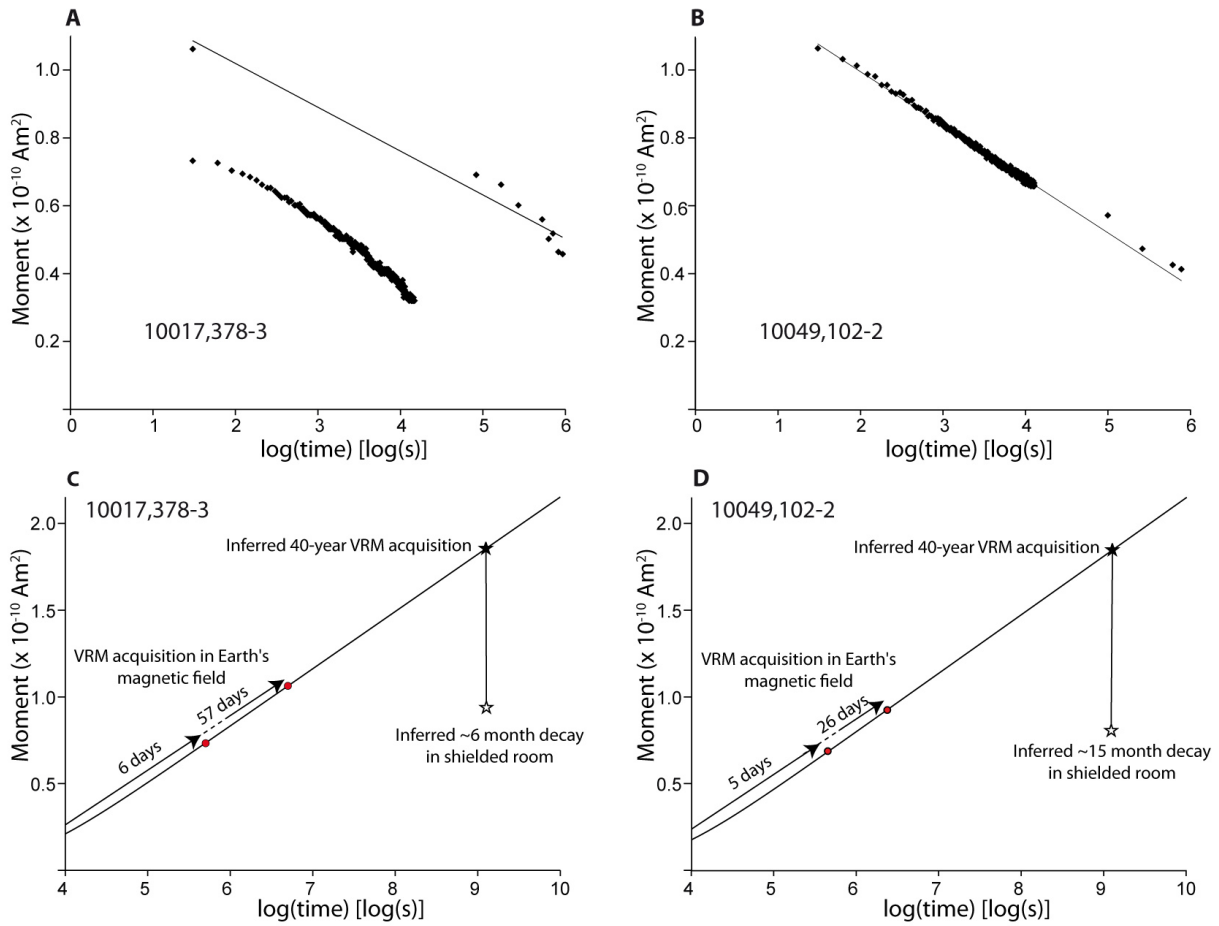
**Fig. S11.** VRM experiments. Samples were stored in the Earth's magnetic field (~50 μT) and then returned to our shielded room (<150 nT) where their moments were semi-continuously measured (diamonds). The 40-year acquisition was estimated assuming linear acquisition rates in log(time) based on 6 and 57 days experiments for 10017, and 5 and 26 days for 10049. The VRM remaining after the decay period in our shielded room was estimated assuming linear decay in log(time) based on the decay measurements. (**A**) Sample 10017,378-3: VRM decay after 57 days acquisition (upper) and 6 days acquisition (lower). The solid line is the least-square logarithmic fit used as a lower limit for the decay rate. (**B**) Sample 10049,102-2: VRM decay after 26 days acquisition. The solid line is the least-square logarithmic fit. (**C**) Estimation of VRM remaining after a ~40 year acquisition period followed by a ~6 month decay period for 10017,378-3. (**D**) Estimation of VRM remaining after a ~40 year acquisition period followed by a ~15 month decay period for 10049,102-2.

## 9. Electron microprobe analysis and imaging

To determine the ferromagnetic mineralogies and late-stage cooling rates of the lunar samples, we conducted electron microprobe analyses and backscattered electron microscopy (BSEM) in the MIT Electron Microprobe Facility on 30 μm thin sections 10017,62 and 10049,40 (Fig. S1 and Tables S7-S13). We used a JEOL 8200 microprobe with 15 keV accelerating voltage, 10 nA beam current, and a spot size less than 1 μm. Raw analytical data were reduced using the $\varphi(\rho z)$ algorithm (69) implemented by Paul Carpenter as CITZAF (70) in the JEOL software. Matrix corrections for oxides use the Armstrong correction (71) and metals use the XPP correction (72).

The cooling timescale was determined using equation (1) of ref. (20). The published equation contains a typo and should be:

$$\log_{10} \text{(plag width, mm)} = -0.66 \log_{10} \text{(cooling rate, °C/hr)} - 1.23$$

## 10. Anisotropy of remanence

Paleomagnetic directions and paleointensity values inferred from samples with strong remanence anisotropy can be biased if this anisotropy is not taken into account. To assess this possibility, we measured the ARM anisotropy of all samples (Table S3). We applied an ARM (85 mT AC field

12

with 0.1 mT DC field) in three orthogonal directions to construct an anisotropy matrix and then solved for the principal axes of the anisotropy ellipsoid following refs. (73, 74).

We found that our subsamples of 10017,378 have anisotropy degrees, $P$, between 1.05 and 1.28, and shape factors, $T$, between –0.61 and –0.04. Subsamples of 10049 have $P$ values between 1.06 and 1.10 and $T$ values between –0.14 and 0.17.

Following ref. (75) we calculated the ancient field direction ($B_{anc}$) by multiplying the measured HC direction by the ARM anisotropy tensor. The ratio of the remanence acquired in a unit field parallel to the ancient field to the remanence acquired in a unit field in the laboratory field direction defines the ratio $r$. Dividing the paleointensity by $r$ yields the anisotropy-corrected paleointensity. These values are very similar to the uncorrected values (Table S2).

## 11. $^{40}Ar*/^{39}Ar_K$ and $^{38}Ar_{cos}/^{37}Ar_{Ca}$ thermochronology

### 11.1 Previous studies

Because 10017 was the largest lunar rock sample brought back during the Apollo 11 mission, subsamples were widely distributed for radiochronology and noble gas measurements. As a result, there is a tremendous amount of previous data available for radiometric ages and cosmic ray exposure ages (Tables S14-S16). We begin by summarizing these early results to contextualize our new measurements described later. The reported apparent exposure and radioisotopic ages were taken directly from the literature and have not been modified for currently accepted production rates and decay constants.

K/Ar ages of whole rock samples were found to be in the range of 2-2.6 Ga, while plagioclase separates have older ages of ~3.2 Ga. This was interpreted as indicating loss of Ar (76). A similar conclusion was reached from $^{40}Ar/^{39}Ar$ measurements (35, 77, 78), as the loss of ~48% of the initial $^{40}Ar$ content was necessary to explain the discrepancy between low temperature and high temperature release data. Because the age plateau was not reached during these experiments, the authors estimated a minimum crystallization age of 3.2 Ga. Other early studies observed Rb/Sr crystallization ages in the range of 3.4-3.78 Ga (32, 76, 79-85), $^{83}Kr/^{81}Kr$ apparent ages of 2.6-2.8 Ga (86, 87), and U/Th ages of 2.55 Ga (88). U-Th-Pb analyses (85, 89, 90) gave discordant ages in the range of 3.6-4.0 Ga, which indicates that the U/Pb system has been disturbed. Finally, recent Sm/Nd measurements yielded a crystallization age of ~3.67 ± 0.069 Ga (85).

Exposure ages were determined using different methods: 340-640 Ma for $^{38}Ar$ data (77, 86, 87, 91-93), 449-510 Ma for $^{81}Kr/^{83}Kr$ data (86, 87, 94, 95), 290-375 Ma for $^{3}He$ data (88, 91-93), 340-387 Ma for $^{21}Ne$ data (88, 92, 93), 340 Ma for $^{22}Na-^{22}Ne$ data (96), and 320-340 for $^{126}Xe$ data (93). 10017 also displays the strongest Gd anomaly of the Apollo 11 samples (95, 97) which indicates that this sample has been exposed to a stronger thermal neutron flux. Depth profiles of numerous cosmogenic radionuclides were also measured within 10017 (98, 99). Cosmic ray tracks indicate a near-surface (< ~3 cm depth) exposure age of 5-11 Ma (100-103) (Table S15). These results are best explained by residence at somewhere >~3 cm and <~3 m depth for the last ~several hundred My followed by ejection to the near-surface (<~ 3 cm depth) at ~5-11 Ma (104-106).

Radiometric and exposure ages for 10049 are listed in Table S15. Apparent K/Ar ages are in the range of 2.6-3.2 Ga (84, 88, 92). High temperature $^{40}Ar-^{39}Ar$ data gives a crystallization age of 3.4 Ga (32). Apparent U/Th ages are in the range of 2.0-2.9 Ga (88, 92). Noble gas and spallation track exposure ages in the range of 21-36 Ma were determined using $^{38}Ar$, $^{3}He$ and $^{21}Ne$ data (84, 88, 92, 103). As the latter ages are similar to its surface exposure age, in the range of 21-36 Ma, 10049 does not show evidence of pre-irradiation in depth before excavation and apparently was excavated to the surface at 20-40 Ma (101-103).

### 11.2. Analytical results

Two whole-rock aliquots of 10049 and 10017 (denoted A and B for each sample) were subjected to $^{40}Ar/^{39}Ar$ analyses at the Berkeley Geochronology Center following procedures described in refs. (7, 107, 108). Apparent $^{40}Ar/^{39}Ar$ ages (Fig. S12) were calculated relative to the Hb3gr standard (age = 1081 Ma) using the decay constants and standard calibration of ref. (33) and isotope

abundances of ref. (109). Cosmogenic isotope abundances and ages were calculated following procedures described in (7, 110). The complete datasets appear in Table S17.

Low-temperature (<1000°C) extractions comprise cosmogenic isotopes degassed from both K-glass and plagioclase. In calculating the apparent cosmic ray exposure ages (Fig. 3) of individual steps, the production rate was adjusted to account for variations in the relative proportion of $^{38}Ar_{cos}$ derived from K-glass and plagioclase according to the following equation:

$$P38_{Ca}\left(10^{-13}\frac{moles\ ^{38}Ar}{g-Ca\cdot Ma}\right) = 8.08 + 12.9\left(\frac{39.1}{40.1}\cdot\left(\frac{K}{Ca}\right)_{meas}\right) + 0.44\left(f_{Ca_{plag}}\left(\frac{[Fe]}{[Ca]}\right)_{plag} + \left(1 - f_{Ca_{plag}}\right)\left(\frac{[Fe]}{[Ca]}\right)_{glass}\right)$$

where $(K/Ca)_{meas}$ is equal to $0.51\times(^{39}Ar_K/^{37}Ar_{Ca})$, elemental concentrations (e.g., [Ca]) are in wt. % and are determined by electron probe microanalysis (EPMA; see Tables S8-S9), and the fraction of $^{37}Ar_{Ca}$ derived from plagioclase is given by

$$f_{Ca_{plag}} = 1 - \left(\frac{\left(\frac{[Ca]}{[K]}\right)_{plag} - \frac{40.1}{39.1}\cdot\left(\frac{Ca}{K}\right)_{meas}}{\left(\frac{[Ca]}{[K]}\right)_{plag} - \left(\frac{[Ca]}{[K]}\right)_{glass}}\right)$$

where $(Ca/K)_{meas}$ is equal to $1.96\times(^{37}Ar_{Ca}/^{39}Ar_K)$.

The two aliquots of each sample yielded internally consistent $^{40}Ar/^{39}Ar$ and $^{38}Ar/^{37}Ar$ release spectra. We observe very similar apparent Ca/K spectra for 10049 and 10017, which is expected due to the common lithology and texture of these two mare basalt samples. However, we also find significant differences between the two samples. Whereas we observe agreement between the two aliquots of of each parent sample in their apparent Ca/K spectra, $^{40}Ar/^{39}Ar$ age spectra (Fig. S12), and in the apparent cosmogenic exposure age spectra (Fig. 3), the $^{40}Ar/^{39}Ar$ plateau ages and exposure ages of the two parent samples differ from one another.

For sample 10049, we observe plateau ages of 3564 ± 11 and 3549 ± 11 Ma (analytical uncertainties given as one standard deviation) for aliquots A and B, respectively, between ~25% and ~75% of the cumulative $^{37}Ar$ release fractions (steps 13-18). The weighted mean age of these two plateaus is 3556 ± 8 Ma. The release spectra patterns of each aliquot are very similar, we observe (i) initial step ages as young as ~1400 Ma, followed by progressive increase in ages up to the plateau values over the initial ~25% of $^{37}Ar$ release, and (ii) apparent step ages as young as ~3000 Ma at steps beyond a cumulative $^{37}Ar$ release fraction of 75%. For 10049, the apparent cosmic ray exposure ages, calculated as described above, are in good agreement at steps 13-18 (primarily derived from plagioclase) with mean exposure ages of 17.7 ± 0.2 Ma and 17.2 ± 0.2 Ma [one standard deviation uncertainties not including uncertainty on the production rate] for aliquots A and B, respectively, and a weighted mean exposure age of 17.5 ± 0.1 Ma.

For sample 10017, we observe plateau ages of 3046 ± 10 and 3028 ± 10 Ma (analytical uncertainties given as one standard deviation) for aliquots A and B, respectively, between ~10% and ~25% of the cumulative $^{37}Ar$ release fractions (steps 17-22). The weighted mean age of these two plateaus is 3037 ± 7 Ma. We also observe (i) initial step ages as young as ~1100 Ma, followed by a progressive increase in ages up to the plateau values over the initial ~10% of $^{37}Ar$ release, and (ii) apparent step ages beyond step 22 that are in agreement with the apparent plateau ages. For 10017, the apparent cosmic ray exposure ages, calculated as described above, are in good agreement between steps 12-18 with mean exposure ages of 309.0 ± 3.7 Ma and 303.1 ± 2.3 Ma for aliquots A and B, respectively. The weighted mean exposure age these two values is 304.7 ± 2.0 Ma. All of these results are in broad agreement with previous analyses of these two samples (Table S18).
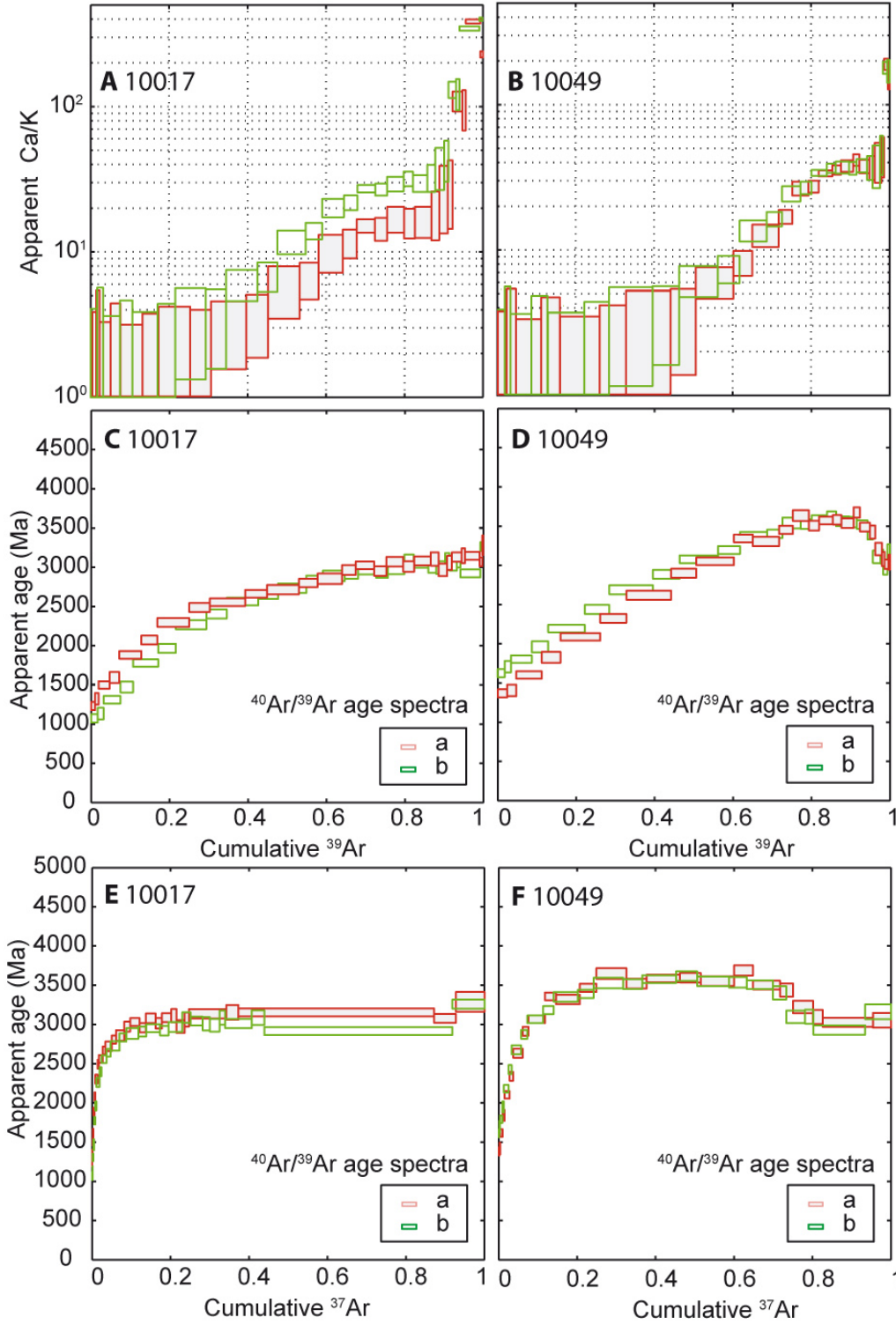
**Fig. S12.** $^{40}$Ar/$^{39}$Ar chronometry of 10017 and 10049. Apparent Ca/K ratios (**A, B**) and $^{40}$Ar/$^{39}$Ar ages (**C, D**) for each step plotted against the cumulative $^{39}$Ar release fraction for 10049. (**E, F**) Same data plotted against the cumulative $^{37}$Ar release fraction.

## 11.3. Modeling results

Diffusion coefficients (Fig. S13) were calculated following procedures described in refs. (7, 110). They reflect gas derived from multiple host phases (i.e., K-glass, plagioclase, pyroxene), each of which comprises a range of grain (domain) sizes. To reproduce the whole-rock diffusion kinetics and simulate lunar thermal histories, multi-phase, multi-domain diffusion (MP-MDD) models were fit to data obtained from aliquots 10017B and 10049B following the detailed procedure described in

15

ref. (7). The MP-MDD model parameters are summarized in Table S18. Additional information regarding MDD models and their applications to multi-phase samples can be found in refs. (7, 110, 111).
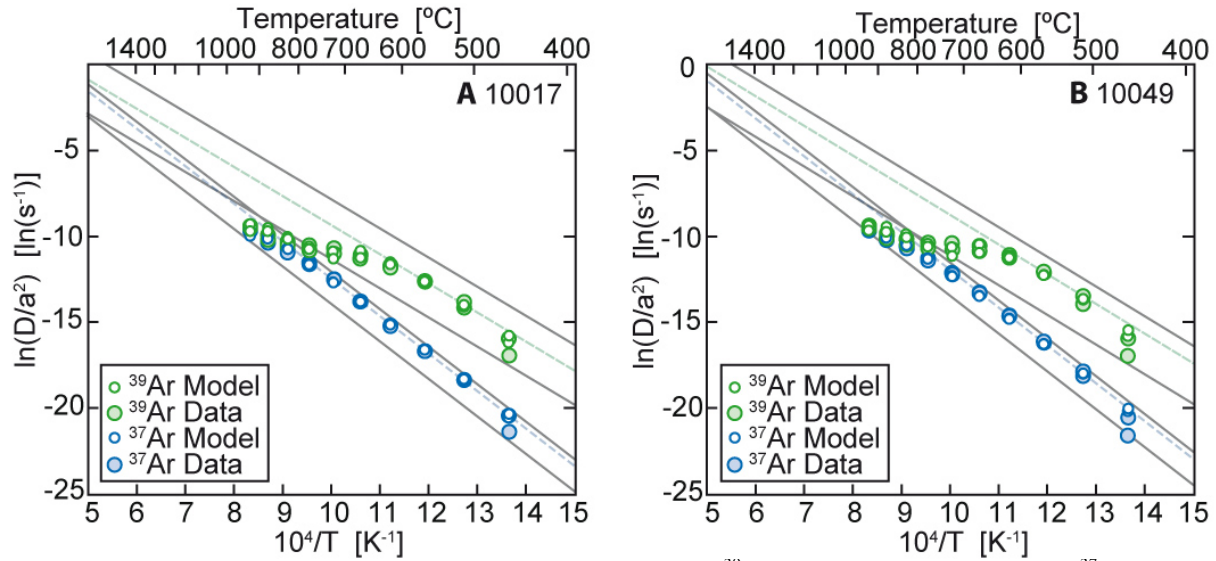


**Fig. S13.** Arrhenius plots with calculated diffusion coefficients for [39]Ar (large green symbols) and [37]Ar (large blue symbols) for 10017 (**A**) and 10049 (**B**) shown alongside the MP-MDD models (small white symbols) fit to the [39]Ar and [37]Ar data using the heating schedule of the analysis and the 4 specified domain sizes and gas fractions listed in Table S18. The grey lines indicate the input diffusion kinetics of each of the four model domains. The colored, dashed lines indicate linear regressions to extractions that yielded reproducible calculated values of $D/a^2$ at a given temperature, which were used to constrain the $E_a$ for Ar diffusion in K-glass ([39]Ar steps 3-6) and plagioclase ([37]Ar steps 3-12).

The discordant radiogenic and exposure age spectra obtained from 10017 and 10049 are indicative of thermally activated diffusive loss of [40]Ar* and [38]Ar$_{cos}$. Ref. (7) showed that daytime heating at the lunar surface to temperatures in excess of 100°C (112, 113) is sufficient to explain diffusive loss of [40]Ar* and [38]Ar$_{cos}$ manifest in spectra obtained from 10020, a comparable mare basalt. A logical question to ask is whether daytime heating can similarly explain the discordance observed in the 10017B and 10049B radiogenic and exposure age spectra. Using our MP-MDD models, we simulated the simultaneous production and diffusive loss of [40]Ar* and [38]Ar$_{cos}$ due to daytime heating for 303.1 ± 2.3 and 17.5 ± 0.1 Ma (for 10017B and 10049B, respectively) following procedures described in ref. (7). The results are shown in Fig. 3 and Fig. S14.

For 10049B, both the exposure and radioisotopic age spectra discordance can be explained by daytime heating at an effective mean (i.e., square-pulse) temperature of ~95°C (Fig. 3). Because diffusivity is an exponential function of temperature, the effective mean temperature is marginally lower (~15°C in the case of 10049 and 10017)[1] than the peak temperature of the sample through the lunation cycle [see refs. (35, 114) for details regarding the lunation cycle and the relationship between the effective mean and peak temperatures, respectively]. Thus, the inferred peak daytime heating temperature is ~110°C. This temperature agrees remarkably well the expected peak temperature at the Apollo 11 landing site [115°C; e.g. (113, 114)] and indicates that 10049 was not buried in the regolith or significantly shadowed during its 17 Ma residence near the lunar surface. The observation that the apparent [40]Ar/[39]Ar plateau age (3.56 ± 0.01 Ga; see Table S18) is indistinguishable from the mean inferred crystallization age of the high-K mare basalts [3.59 ± 0.04 Ga; (32)] is also consistent with a low-temperature thermal history for 10049. Thus 10049 appears

---

[1] The extent to which the effective mean temperature underestimates the peak temperature of lunar daytime heating is contingent upon on the temperature-dependence (i.e., activation energy) of the degassing phase (i.e., K-glass). For an $E_a$ of ~140 kJ/mole (33 kcal/mole) the difference between the effective mean and peak temperatures is ~15 °C.

not to have experienced temperatures in excess of ~115°C (i.e., surface temperatures) since it crystallized.

For 10017B, the exposure age spectrum discordance can be explained by daytime heating, but the radioisotopic age spectrum discordance cannot. The apparent plateau observed at 3.03 Ga underestimates the inferred crystallization age [3.59 ± 0.04 Ga; (32)] by ~0.6 Ga. Lunar surface temperatures are insufficient to extensively degas $^{40}$Ar* from the more retentive plagioclase domains over the noble gas cosmic ray exposure age of 303.1 Ma, such that the difference between the apparent plateau and crystallization ages cannot be reconciled. Thus it appears that the K/Ar system in plagioclase was reset at ~3 Ga by a thermal event involving higher temperatures, giving rise to the apparent plateau observed on the $^{40}$Ar/$^{39}$Ar age spectrum.
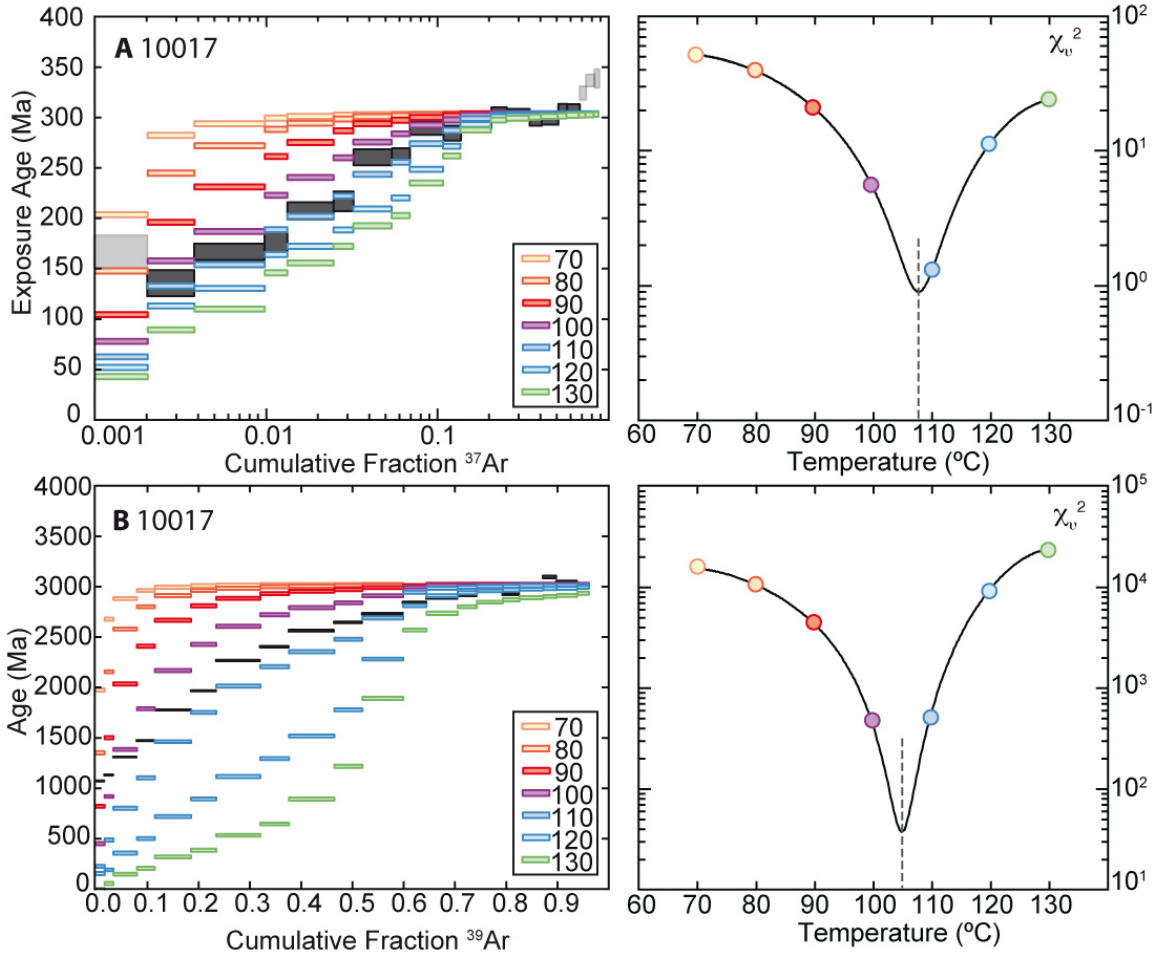


**Fig. S14.** The predicted effects of solar heating at the lunar surface for the last 5 Ma using the 10017 MP-MDD model. (**A**) The production and diffusion of $^{38}$Ar$_{cos}$. The observed exposure ages ± 1 standard deviation (gray boxes) are plotted against the cumulative release fraction of $^{37}$Ar released (note the log scale). $^{38}$Ar$_{cos}$ was produced in-situ while 10017 was exposed at the surface of the Moon. The colored steps are model release spectra calculated using the MP-MDD model parameters shown in Table S18 and for the production and diffusion of $^{38}$Ar$_{cos}$ assuming 10017 was subjected to various constant effective daytime temperatures ranging from 70 to 130°C during the last 5 Ma (i.e., $^{38}$Ar$_{cos}$ is produced continuously over this duration, while diffusion occurs only over half of this period during elevated daytime temperatures). To the right, the reduced chi squared fit statistic for each model is shown, identifying ~106.5°C as the best-fit effective mean temperature. (**B**) The diffusion of $^{40}$Ar* due to solar heating, calculated assuming the crystallization age is 3.03 Ga [symbols and model parameters are the same as (**A**)].

The remaining discordance represented by individual steps with ages lower than 3 Ga can be explained by daytime heating of 10017. Assuming that the rock was submitted to daytime heating for the whole of its ~300 Ma noble gas cosmic ray exposure age, the discordance is best explained by heating at an effective mean temperature of ~80°C (Fig. 3), as predicted by the exposure age spectrum, too. The inferred corresponding peak daytime heating temperature of ~95°C is ~20°C

lower than that expected at the Apollo 11 landing site. Interestingly, depth-dependent cosmogenic Xe isotopes in 10017 provide evidence for a period of shallow burial near the lunar surface (104), and cosmic ray tracks indicate very near-surface (<~3 cm) exposure since 5-11 Ma. This rock may therefore have been buried deep enough so as not to undergo daytime temperature cycling for part of its ~300 Ma noble gas cosmic ray exposure age until excavation at 5-11 Ma (115). Assuming that the daytime heating lasted for 5 My only, the radioisotopic age spectrum is best explained by an effective mean temperature of 105°C (Fig. S14), and the exposure age spectrum by an effective mean temperature of 108°C (Fig. S14). The average corresponding peak temperature is 121.5°C, which is in good agreement with the peak temperature expected at the Apollo 11 landing site. A longer exposure to daytime heating would result in lower temperatures, but the whole range of temperatures corresponding to exposures in the range of 5-303 Ma is consistent with the conditions at the sampling site.

Fig. 3F depicts the minimum duration-temperature conditions required to reset the most retentive plagioclase domains during the proposed 3.0 Ga thermal event. Cosmogenic Xe isotopes (95, 104, 105) indicate the possibility that at least 10017 experienced continuous exposure to slow neutrons produced by cosmic rays at modest depths (~1-5 m) since 3.0 Ga. However, the $^{38}$Ar exposure age limits the very near surface exposure history: it must have been buried sufficiently deeply such that it was shielded from $^{38}$Ar-producing cosmic rays prior to near surface exposure 300-500 Ma ago. The burial depth must have been >~3 m, where cosmogenic Xe isotopes production continues and $^{38}$Ar production tapers off. Assuming a thermal diffusivity of $10^{-6}$ m$^2$s$^{-1}$, we compute the time it takes to diffusively cool a rock from an initial temperature $T$ to <100°C in the middle of a nominal 6 m thick ejecta blanket (i.e., 3 m below the surface). This will provide an upper limit on the cooling rate since porous regolith can have ~100 times lower diffusivity than solid rock (136). Permissible peak temperatures in thicker ejecta blankets would intersect the plagioclase resetting curve at significantly lower temperatures. As the plagioclase resetting occurs at temperatures below the Curie point of kamacite (780ºC), it is possible for a thermal event to reset the plagioclase while preserving the remanence. Most of the magnetization of rocks is carried by magnetic grains that have blocking temperatures within a few tens of degrees of the Curie point (23), so a demagnetization of grains with low blocking temperatures is expected to have only a small effect on the total magnetization. Furthermore, day-night cycling at the surface of the Moon for ~300 Ma and storage in zero-field in our laboratory should have allowed low blocking temperature grains to relax their magnetization (22), which means that even samples that did not go through a temperature excursion may not carry any magnetization in their low blocking temperature grains. In summary, the Ar/Ar data are permissive of but do not require complete remagnetization of 10017 at 3 Ga. However, the similarity of the paleomagnetic records of 10017 and 10049, both in coercivity range and paleointensity, supports the idea of a thermal excursion that did not reset the magnetic record of 10017.

*11.4. Summary*

A possible geologic history of 10049, consistent with the thermochronology data, can be summarized by the following:
1) Sample 10049 crystallized at ~3.56 Ga, as quantified by the plateau portion of the age spectrum.
2) After ~3.54 Ga of quiescence, an impact event brought 10049 to the surface at ~17.5 Ma, where daytime heating caused diffusive loss of both $^{40}$Ar* and $^{38}$Ar$_{cos}$.

A possible geologic history of 10017, consistent with the thermochronology, can be summarized by the following:
1) Sample 10017 crystallized at ~3.56 Ga.
2) At ~3.0 Ga the sample was ejected from its bedrock location and deposited in a thick, hot ejecta blanket, resulting in the diffusive loss of $^{40}$Ar* and the plateau portion of the age spectrum while preserving its magnetic record in the high blocking temperature grains.

18

3) At ~305 Ma, a second impact event brought 10017 close to the surface (below 15 cm), where it was exposed to cosmic ray but protected from daytime heating.
4) At 5-11 Ma, a third impact event brought 10017 to the surface, where daytime heating caused diffusive loss of both $^{40}Ar^*$ and $^{38}Ar_{cos}$.

**Table S1.** Lunar impact craters with diameters larger than 230 km (47).

| Name | Diam. (km) | Age | Lon. (°) | Lat. (°) |
|---|---|---|---|---|
| South Pole-Aitken | 2050 | Pre-Nectarian | -170.0 | -54.0 |
| Imbrium | 1114 | Lower Imbrian | -17.4 | 33.5 |
| Crisium | 1092 | Nectarian | 59.8 | 17.0 |
| Orientale outer ring | 928 | Lower Imbrian | -94.6 | -19.7 |
| Nectaris | 915 | Nectarian | 34.7 | -14.5 |
| Smythii | 887 | Pre-Nectarian | 86.6 | -1.8 |
| Nubium | 835 | Pre-Nectarian | -15.4 | -18.6 |
| Serenitatis | 659 | Nectarian | 18.9 | 27.0 |
| Mendel-Rydberg | 636 | Nectarian | -93.7 | -50.1 |
| Moscoviense outer ring | 629 | Nectarian | 148.8 | 27.5 |
| Humboldtianum | 603 | Nectarian | 82.0 | 57.2 |
| Freundlich-Sharonov | 582 | Pre-Nectarian | 175.0 | 18.3 |
| Hertzsprung | 549 | Nectarian | -129.2 | 2.0 |
| Apollo | 476 | Pre-Nectarian | -151.7 | -36.1 |
| *unnamed* | 453 | older than Nectarian | 149.0 | -4.9 |
| Korolev | 417 | Nectarian | -157.5 | -4.4 |
| Humorum | 408 | Nectarian | -39.7 | -24.7 |
| Moscoviense inner ring | 402 | Nectarian | 147.0 | 26.1 |
| *unnamed* | 394 | Pre-Nectarian[a] | -158.2 | 13.5 |
| Amundsen-Ganswindt | 379 | Pre-Nectarian | 123.3 | -81.1 |
| *unnamed* | 359 | Pre-Nectarian[a] | -169.8 | 25.1 |
| Schiller-Zucchius | 350 | Pre-Nectarian | -45.3 | -55.5 |
| Lorentz | 333 | Pre-Nectarian | -97.1 | 34.4 |
| Mendeleev | 331 | Nectarian | 141.1 | 5.4 |
| Planck | 321 | Pre-Nectarian | 135.1 | -57.4 |
| Ingenii | 319 | Pre-Nectarian | 163.7 | -32.8 |
| Coulomb-Sarton | 316 | Pre-Nectarian | -122.5 | 51.3 |
| Schrodinger | 313 | Lower Imbrian | 133.5 | -74.9 |
| Poincare | 312 | Pre-Nectarian | 163.2 | -57.3 |
| Birkhoff | 308 | Pre-Nectarian | -147.2 | 59.3 |
| Bailly | 299 | Nectarian | -68.8 | -67.2 |
| *unnamed* | 276 | older than Orientale | -108.5 | -28.1 |
| Harkhebi | 265 | Pre-Nectarian | 98.6 | 40.4 |
| Balmer-Kapteyn | 265 | Pre-Nectarian | 69.3 | -15.6 |
| Gagarin | 256 | Pre-Nectarian | 149.4 | -19.7 |
| Sikorsky-Rittenhouse | 252 | Nectarian | 109.1 | -68.6 |
| Milne | 251 | Nectarian | 112.9 | -31.5 |
| Von Karman M | 245 | Pre-Nectarian | 176.3 | -47.0 |
| *unnamed* | 242 | Pre-Nectarian | 167.8 | -3.2 |
| Fermi | 241 | Pre-Nectarian | 123.4 | -19.7 |
| Iridum | 234 | Lower Imbrian[b] | -31.2 | 44.5 |
| Grimaldi inner ring | 234 | Pre-Nectarian | -68.7 | -5.0 |
| Leibnitz | 234 | Pre-Nectarian | 179.1 | -38.3 |
| d'Alembert | 232 | Nectarian | 164.8 | 51.1 |
| Janssen | 230 | Pre-Nectarian | 40.6 | -44.3 |

[a]These craters were previously unidentified. They have in excess of $2\times10^{-4}$ craters with diameter >20 km per square kilometer, and are therefore probably Pre-Nectarian in age (117).
[b]This crater was originally identified as Upper Imbrian (38), but has since been attributed to the Lower Imbrian (118).

**Table S2.** NRM paleointensity estimates for 10017 and 10049.

| Sample, Experiment | LC slope | HC slope | Paleointensity (µT) | Anisotropy-corrected Paleointensity (µT) |
|---|---|---|---|---|
| **10017,378-2** | | | | |
| ARM 50 µT* | - | 2.23±0.03 | 83.2±1.2 | 83.5±1.2 |
| ARM 100 µT* | - | 1.08±0.01 | 80.3±0.8 | 80.6±0.8 |
| IRM* | - | 0.032±0.001 | 94.8±4.6 | 95.1±4.6 |
| **10017,378-3** | | | | |
| ARM 50 µT | - | 2.15±0.04 | 80.2±1.7 | 78.2±1.7 |
| ARM 100 µT | - | 1.05±0.01 | 78.7±1.1 | 76.7±1.1 |
| IRM | 0.083±0.011 | 0.028±0.001 | 85.0±1.6 | 82.9±1.6 |
| **10017,378-7** | | | | |
| ARM 50 µT | - | 1.67±0.03 | 62.2±1.2 | 64.9±1.2 |
| ARM 100 µT | - | 0.71±0.01 | 53.2±0.8 | 55.5±0.8 |
| IRM | 0.043±0.032 | 0.020±0.001 | 59.3±3.0 | 61.9±3.0 |
| **10017,378-8** | | | | |
| ARM 50 µT | - | 1.31±0.04 | 49.0±1.5 | 50.5±1.5 |
| ARM 100 µT | - | 0.61±0.02 | 45.8±1.6 | 47.2±1.6 |
| IRM | 0.066±0.007 | 0.014±0.001 | 41.9±2.3 | 43.2±2.3 |
| **Mean 10017** | | | | |
| ARM 50 µT | - | - | 68.7±13.9 | 69.3±12.8 |
| ARM 100 µT | - | - | 64.5±15.2 | 64.0±14.0 |
| ARM all | - | - | 66.6±14.7 | 67.1±13.6 |
| IRM | - | - | 70.3±20.9 | 70.8±19.9 |
| All experiments | - | - | 67.8±17.1 | 68.4±16.0 |
| **10049,102-1** | | | | |
| ARM 50 µT | - | 1.84±0.37 | 69.7±5.3 | 69.7±5.3 |
| ARM 100 µT | - | 1.16±0.06 | 86.3±4.6 | 86.3±4.6 |
| IRM | 0.040±0.005 | 0.032±0.001 | 95.2±4.3 | 95.2±4.3 |
| **10049,102-2** | | | | |
| ARM 50 µT | - | 1.48±0.04 | 55.2±1.3 | 55.2±1.3 |
| ARM 100 µT | - | 0.66±0.01 | 49.3±1.0 | 49.3±1.0 |
| IRM | 0.026±0.003 | 0.020±0.001 | 59.1±3.2 | 59.1±3.2 |
| **Mean 10049** | | | | |
| ARM 50 µT | - | - | 62.5±7.3 | 62.5±7.3 |
| ARM 100 µT | - | - | 67.8±18.5 | 67.8±18.5 |
| ARM all | - | - | 65.1±14.3 | 65.1±14.3 |
| IRM | - | - | 77.2±18.1 | 77.2±18.1 |
| All experiments | - | - | 69.1±16.6 | 69.1±16.6 |
| **High-K basalts** | | | | |
| ARM 50 µT | - | - | 66.6±12.4 | 67.0±11.7 |
| ARM 100 µT | - | - | 65.6±16.4 | 65.9±15.7 |
| ARM all | - | - | 66.1±14.6 | 66.5±13.9 |
| IRM | - | - | 72.6±20.2 | 72.9±19.5 |
| All experiments | - | - | 68.2±17.0 | 68.6±16.3 |

*Note:* The first column gives the names of the subsample and paleointensity method or the mean values; the second column gives the slope for the LC component inferred from plots of NRM lost vs. IRM lost; the third column gives the slope for the HC component inferred from plots of NRM lost vs. IRM lost or NRM lost vs. ARM lost; the fourth column gives ARM paleointensity in µT= (NRM lost)/(ARM lost)/$f'$ × (bias field in µT) or IRM paleointensity in µT = (NRM lost)/(IRM lost) × $a$ where we used $f'$ = 1.34 and $a$ = 3000. Uncertainties on each paleointensity value are formal 95% confidence intervals on the slope fit using Student's t-test (31) and do not include the factor of ~3-5 uncertainty associated with the unknown ratios of ARM and IRM to TRM. Uncertainties on mean values are observed 1 standard deviation from multiple samples. Calculated values are rounded to the nearest decimal place but calculations were conducted with raw data.

*For these experiments, AF demagnetization of NRM was carried out without repeated steps for GRM and spurious ARM correction.

**Table S3.** Anisotropy of ARM (85 mT AC field with 0.1 mT DC field).

| Sample | Anisotropy degree $P$ | Shape factor $T$ |
|---|---|---|
| 10017,378-2 | 1.05 | -0.21 |
| 10017,378-3 | 1.16 | -0.04 |
| 10017,378-7 | 1.28 | -0.61 |
| 10017,378-8 | 1.10 | -0.37 |
| 10049,102-1 | 1.10 | 0.17 |
| 10049,102-2 | 1.06 | -0.14 |

**Table S4.** Paleointensity fidelity estimates for 10017 and 10049. Recovered intensity calculated via the ARM method with a bias field of 200 µT.

| Sample, ARM DC Bias Field (µT) | TRM-Equivalent Field (µT) | Recovered Intensity (µT) | Uncertainty (%) |
|---|---|---|---|
| **10017,378-8** | | | |
| 10 | 7.46 | 8.14 | 15.22 |
| 20 | 14.93 | 16.69 | 5.03 |
| 50 | 37.31 | 33.81 | 8.70 |
| 100 | 74.63 | 73.52 | 3.14 |
| **10049,102-1** | | | |
| 10 | 7.46 | 15.43 | 23.52 |
| 20 | 14.93 | 19.72 | 12.41 |
| 50 | 37.31 | 38.91 | 7.51 |
| 100 | 74.63 | 74.64 | 3.79 |

*Note:* Recovered paleointensity in µT = (NRM/ARM)/$f'$ × (bias field in µT) using $f'$ = 1.34. Uncertainties on each limit are formal 95% confidence intervals on the slope fit using Student's t-test (31).

**Table S5.** Rock magnetic parameters derived from remanence measurements.

| Sample | MDF ARM$_{200}$ (mT) | MDF IRM$_{200}$ (mT) | $R$ | $B_{cr}$ (mT) | $B_c$ (mT) | $M_{rs}$ (Am$^2$) | $M_s$ (Am$^2$) |
|---|---|---|---|---|---|---|---|
| **10017,378-1** | 42 | 27 | - | - | - | - | - |
| **10017,378-2** | 32 | 22 | 0.34 | -/45 | - | - | - |
| **10017,378-3** | - | 27 | - | - | - | - | - |
| **10017,378-7** | 38 | 28 | - | - | - | - | - |
| **10017,378-8** | 35 | 29 | - | 87/- | 3.0 | 1.88 ×10$^{-7}$ | 3.42 ×10$^{-5}$ |
| **10049,102-1** | 14 | 19 | 0.37 | 32/- | - | - | - |

*Note:* The first column gives the names of the subsample, the second column gives the mean AF destructive field for an ARM produced by a 200 mT AC field and 2 mT DC field; the third column gives the mean AF destructive field for an IRM produced by a 200 mT field; the fourth column gives the Cisowski $R$ value (41); the fifth column gives two estimates of the coercivity of remanence ($B_{cr}$): the first is derived from the intersection of AF of IRM and IRM acquisition curves (Fig. S8) following (41), while the second is the back field required to reduce a saturation IRM to zero moment; the sixth column gives the coercivity ($B_c$), the seventh column gives the saturation remanence ($M_{rs}$), and the seventh column gives the saturation magnetization ($M_s$). A dash indicates that quantity was not measured.

**Table S6.** Modal abundances in 10017 and 10049 [both from ref. (21)].

| Sample, Mineral | Abundance |
|---|---|
| **10017** | |
| Pyroxene | 48-60% |
| Plagioclase | 18-27% |
| Ilmenite | 15-24% |
| K-glass | 1-2% |
| **10049** | |
| Pyroxene | 47-51% |
| Plagioclase | 18-25% |
| Ilmenite | 14-17% |
| K-glass | 1-2% |

**Table S7.** Composition of typical metal grains in thin sections 10017,62 and 10049,40.

| Sample, Measurement # | Fe | Ni | Total |
|---|---|---|---|
| **10017,62** | | | |
| 1 | 98.4 | 0.4 | 98.8 |
| 2 | 98.2 | 0.4 | 98.6 |
| 3 | 97.4 | 0.4 | 97.8 |
| 4 | 97.2 | 0.4 | 97.6 |
| Ave. | 97.8 | 0.4 | 96.1 |
| Max. | 98.4 | 0.4 | 98.8 |
| Min. | 97.2 | 0.4 | 97.6 |
| **10049,40** | | | |
| 1 | 96.1 | 0.3 | 96.5 |
| 2 | 98.7 | 0.3 | 99.0 |
| 3 | 97.7 | 0.4 | 98.1 |
| Ave. | 97.9 | 0.3 | 97.9 |
| Max. | 96.5 | 0.3 | 96.5 |
| Min. | 99.0 | 0.4 | 99.0 |

*Note:* Analyses presented as wt.% rounded to the nearest decimal place. Calculations were conducted using raw data acquired with MIT microprobe. Detection limits as follows (in wt.%): Ni-0.005, Fe-0.002. Standards were pure Fe and Ni metal.

**Table S8.** Composition of plagioclase grains in 10017,62 measured with MIT microprobe.

| # | $SiO_2$ | CaO | FeO | $Na_2O$ | $Al_2O_3$ | $K_2O$ | MgO | Total | An | Ab | Or | Ca/K |
|---|---|---|---|---|---|---|---|---|---|---|---|---|
| 1 | 50.1 | 15.8 | 0.6 | 2.3 | 31.3 | 0.2 | 0.2 | 100.6 | 0.86 | 0.13 | 0.014 | 53.4 |
| 2 | 49.1 | 16.3 | 0.5 | 2.1 | 32.1 | 0.1 | 0.2 | 100.4 | 0.88 | 0.11 | 0.007 | 109.2 |
| 3 | 49.6 | 16.0 | 0.4 | 2.3 | 31.9 | 0.2 | 0.3 | 100.7 | 0.87 | 0.12 | 0.009 | 85.0 |
| 4 | 48.8 | 16.1 | 0.5 | 2.1 | 31.5 | 0.2 | 0.3 | 99.4 | 0.88 | 0.11 | 0.009 | 85.7 |
| 5 | 49.3 | 16.0 | 0.5 | 2.1 | 31.5 | 0.2 | 0.3 | 99.8 | 0.88 | 0.12 | 0.008 | 89.2 |
| 6 | 48.4 | 16.1 | 0.6 | 2.2 | 31.3 | 0.2 | 0.3 | 98.9 | 0.87 | 0.12 | 0.008 | 90.0 |
| 7 | 49.4 | 15.6 | 0.6 | 2.2 | 30.7 | 0.2 | 0.3 | 98.9 | 0.87 | 0.12 | 0.010 | 71.1 |
| 8 | 48.0 | 14.8 | 0.5 | 2.3 | 29.9 | 0.2 | 0.3 | 96.1 | 0.86 | 0.13 | 0.011 | 63.4 |
| 9 | 46.2 | 15.0 | 0.6 | 2.1 | 30.4 | 0.2 | 0.2 | 94.7 | 0.86 | 0.12 | 0.012 | 59.2 |
| 10 | 49.2 | 15.8 | 0.5 | 2.1 | 31.2 | 0.2 | 0.3 | 99.2 | 0.87 | 0.12 | 0.011 | 66.1 |
| 11 | 48.4 | 15.3 | 0.7 | 2.3 | 29.9 | 0.2 | 0.2 | 97.0 | 0.86 | 0.13 | 0.012 | 61.4 |
| 12 | 46.4 | 15.5 | 0.5 | 2.4 | 28.6 | 0.2 | 0.2 | 93.8 | 0.86 | 0.13 | 0.013 | 57.3 |
| 13 | 34.8 | 14.3 | 0.5 | 2.2 | 23.9 | 0.2 | 0.2 | 76.2 | 0.86 | 0.13 | 0.013 | 56.8 |
| 14 | 40.6 | 14.9 | 0.5 | 2.1 | 26.2 | 0.2 | 0.3 | 84.7 | 0.87 | 0.12 | 0.012 | 60.4 |
| 15 | 33.8 | 13.3 | 0.9 | 2.6 | 21.6 | 0.3 | 0.2 | 72.6 | 0.82 | 0.16 | 0.016 | 42.0 |
| 16 | 42.3 | 15.3 | 0.7 | 1.6 | 27.2 | 0.2 | 0.1 | 87.4 | 0.89 | 0.09 | 0.012 | 65.0 |
| 17 | 51.6 | 14.7 | 0.8 | 2.5 | 30.3 | 0.3 | 0.1 | 100.4 | 0.84 | 0.14 | 0.016 | 44.3 |
| 18 | 49.8 | 15.5 | 0.8 | 2.2 | 31.3 | 0.2 | 0.2 | 99.9 | 0.87 | 0.12 | 0.012 | 60.6 |
| 19 | 48.9 | 15.7 | 0.8 | 2.1 | 31.0 | 0.2 | 0.2 | 98.9 | 0.87 | 0.12 | 0.011 | 64.3 |
| 20 | 49.1 | 15.4 | 0.9 | 2.0 | 31.4 | 0.2 | 0.2 | 99.2 | 0.88 | 0.11 | 0.012 | 61.3 |
| 21 | 50.2 | 15.3 | 0.9 | 2.2 | 31.1 | 0.2 | 0.2 | 100.0 | 0.86 | 0.12 | 0.013 | 55.0 |
| 22 | 49.2 | 15.6 | 0.9 | 2.1 | 30.5 | 0.2 | 0.2 | 98.8 | 0.87 | 0.12 | 0.011 | 68.2 |
| 23 | 49.8 | 15.4 | 0.7 | 2.1 | 30.6 | 0.2 | 0.3 | 99.1 | 0.87 | 0.12 | 0.011 | 68.0 |
| 24 | 49.9 | 15.6 | 0.7 | 2.1 | 30.8 | 0.2 | 0.3 | 99.5 | 0.87 | 0.12 | 0.010 | 70.6 |
| Ave. | 47.2 | 15.4 | 0.7 | 2.2 | 29.8 | 0.2 | 0.2 | 95.7 | 0.87 | 0.12 | 0.01 | 67.0 |
| Max. | 51.6 | 16.3 | 0.9 | 2.6 | 32.1 | 0.3 | 0.3 | 100.7 | 0.89 | 0.16 | 0.02 | 109.2 |
| Min. | 33.8 | 13.3 | 0.5 | 1.6 | 21.6 | 0.1 | 0.1 | 72.5 | 0.82 | 0.09 | 0.01 | 42.0 |

**Table S9.** Composition of plagioclase grains in 10049,40 measured with MIT microprobe.

| # | SiO$_2$ | CaO | FeO | Na$_2$O | Al$_2$O$_3$ | K$_2$O | MgO | Total | An | Ab | Or | Ca/K |
|---|---------|-----|-----|---------|-------------|--------|-----|-------|-----|-----|-------|------|
| 1 | 51.0 | 16.0 | 1.0 | 2.2 | 31.0 | 0.2 | 0.2 | 101.6 | 0.87 | 0.12 | 0.013 | 55.1 |
| 2 | 52.3 | 15.2 | 1.1 | 2.4 | 30.4 | 0.3 | 0.2 | 101.8 | 0.85 | 0.13 | 0.016 | 45.0 |
| 3 | 51.7 | 15.2 | 0.9 | 2.4 | 30.7 | 0.3 | 0.2 | 101.4 | 0.85 | 0.13 | 0.014 | 51.0 |
| 4 | 50.9 | 15.8 | 1.0 | 2.2 | 31.4 | 0.2 | 0.2 | 101.7 | 0.87 | 0.12 | 0.012 | 60.6 |
| 5 | 51.0 | 15.6 | 0.8 | 2.2 | 30.7 | 0.2 | 0.3 | 100.8 | 0.87 | 0.12 | 0.012 | 61.1 |
| 6 | 50.9 | 15.7 | 0.9 | 2.0 | 31.1 | 0.2 | 0.3 | 101.0 | 0.88 | 0.11 | 0.013 | 58.6 |
| 7 | 50.5 | 15.6 | 0.9 | 2.1 | 31.2 | 0.2 | 0.2 | 100.8 | 0.87 | 0.12 | 0.014 | 53.5 |
| 8 | 51.2 | 15.6 | 1.0 | 2.2 | 30.5 | 0.3 | 0.2 | 100.9 | 0.86 | 0.12 | 0.014 | 51.2 |
| 9 | 51.0 | 15.8 | 0.8 | 2.1 | 30.7 | 0.2 | 0.3 | 100.9 | 0.87 | 0.12 | 0.012 | 59.4 |
| 10 | 50.7 | 15.7 | 1.0 | 2.0 | 30.8 | 0.3 | 0.3 | 100.7 | 0.87 | 0.11 | 0.014 | 52.6 |
| 11 | 51.2 | 15.4 | 0.9 | 2.2 | 30.6 | 0.2 | 0.3 | 100.9 | 0.87 | 0.12 | 0.012 | 60.5 |
| 12 | 51.2 | 15.7 | 0.9 | 2.2 | 30.7 | 0.3 | 0.2 | 101.2 | 0.87 | 0.12 | 0.014 | 52.6 |
| 13 | 50.3 | 16.0 | 0.7 | 2.0 | 31.4 | 0.2 | 0.2 | 100.9 | 0.88 | 0.11 | 0.011 | 68.9 |
| 14 | 51.2 | 15.6 | 1.0 | 2.2 | 30.5 | 0.2 | 0.4 | 101.0 | 0.87 | 0.12 | 0.012 | 62.6 |
| 15 | 51.8 | 15.1 | 1.1 | 2.4 | 30.2 | 0.3 | 0.2 | 101.1 | 0.85 | 0.14 | 0.016 | 45.1 |
| 16 | 49.7 | 16.1 | 0.9 | 2.0 | 31.8 | 0.2 | 0.3 | 100.8 | 0.88 | 0.11 | 0.011 | 68.1 |
| 17 | 50.8 | 15.8 | 0.8 | 2.1 | 31.0 | 0.2 | 0.3 | 100.9 | 0.87 | 0.11 | 0.012 | 61.0 |
| 18 | 50.9 | 15.4 | 0.8 | 2.3 | 30.7 | 0.2 | 0.3 | 100.6 | 0.86 | 0.13 | 0.012 | 58.2 |
| 19 | 50.3 | 16.0 | 0.8 | 2.0 | 31.5 | 0.2 | 0.3 | 101.0 | 0.88 | 0.11 | 0.010 | 72.7 |
| 20 | 51.3 | 15.3 | 0.9 | 2.3 | 30.6 | 0.2 | 0.3 | 100.9 | 0.86 | 0.13 | 0.012 | 59.4 |
| Ave. | 51.0 | 15.6 | 0.9 | 2.1 | 30.1 | 0.2 | 0.3 | 101.1 | 0.87 | 0.12 | 0.01 | 57.9 |
| Max. | 52.3 | 16.1 | 1.1 | 2.4 | 31.8 | 0.3 | 0.4 | 101.8 | 0.88 | 0.14 | 0.02 | 72.7 |
| Min. | 49.7 | 15.1 | 0.8 | 1.0 | 30.2 | 0.2 | 0.2 | 100.6 | 0.85 | 0.11 | 0.01 | 45.0 |

**Table S10.** Composition of pyroxene grains in 10017,62 measured with MIT microprobe.

| # | TiO$_2$ | Al$_2$O$_3$ | K$_2$O | MnO | Na$_2$O | Cr$_2$O$_3$ | SiO$_2$ | CaO | FeO | MgO | Total |
|---|---------|-------------|--------|-----|---------|-------------|---------|-----|-----|-----|-------|
| 1 | 1.4 | 1.8 | - | 0.15 | 0.06 | 0.4 | 52.1 | 13.9 | 12.3 | 19.0 | 101.2 |
| 2 | 1.9 | 2.3 | - | 0.16 | 0.12 | 0.5 | 51.6 | 16.6 | 10.6 | 17.8 | 101.5 |
| 3 | 1.8 | 2.9 | 0.01 | 0.21 | 0.08 | 0.4 | 50.3 | 13.1 | 15.0 | 16.9 | 100.6 |
| 4 | 1.4 | 2.1 | 0.01 | 0.18 | 0.07 | 0.3 | 50.9 | 17.4 | 14.3 | 14.4 | 100.9 |
| 5 | 1.8 | 2.5 | 0.01 | 0.14 | 0.10 | 0.4 | 50.3 | 17.9 | 9.9 | 16.9 | 100.0 |
| 6 | 1.7 | 2.7 | - | 0.17 | 0.09 | 0.5 | 50.9 | 15.6 | 12.1 | 17.6 | 101.2 |
| 7 | 1.8 | 3.3 | - | 0.16 | 0.07 | 0.4 | 50.5 | 17.1 | 11.3 | 15.9 | 100.4 |
| 8 | 1.7 | 2.9 | - | 0.15 | 0.12 | 0.4 | 50.1 | 16.8 | 10.4 | 16.8 | 99.4 |
| 9 | 1.8 | 2.6 | - | 0.16 | 0.10 | 0.4 | 49.5 | 17.0 | 10.0 | 17.3 | 98.8 |
| 10 | 0.8 | 1.3 | - | 0.29 | - | 0.2 | 51.1 | 4.8 | 20.5 | 21.4 | 100.3 |
| 11 | 1.4 | 2.2 | - | 0.23 | 0.07 | 0.3 | 50.2 | 13.6 | 15.6 | 16.9 | 100.5 |
| 12 | 0.6 | 0.9 | - | 0.28 | 0.01 | 0.2 | 52.1 | 4.7 | 20.8 | 22.5 | 102.0 |
| 13 | 1.7 | 2.4 | - | 0.15 | 0.13 | 0.4 | 51.0 | 16.9 | 10.4 | 17.8 | 100.8 |
| 14 | 1.4 | 2.3 | - | 0.22 | 0.09 | 0.3 | 49.8 | 14.3 | 15.2 | 16.7 | 100.2 |
| 15 | 1.6 | 2.3 | - | 0.15 | 0.10 | 0.4 | 52.2 | 15.8 | 10.7 | 17.7 | 100.9 |
| 16 | 1.4 | 2.9 | 0.01 | 0.22 | 0.09 | 0.3 | 51.8 | 16.3 | 12.4 | 16.5 | 101.8 |
| 17 | 1.2 | 2.3 | 0.01 | 0.20 | 0.11 | 0.3 | 51.2 | 17.6 | 13.6 | 14.7 | 101.1 |
| 18 | 0.5 | 0.8 | - | 0.26 | - | 0.2 | 54.0 | 4.6 | 17.6 | 21.2 | 101.9 |
| 19 | 0.4 | 0.8 | 0.01 | 0.27 | 0.01 | 0.1 | 53.7 | 4.3 | 4.6 | 22.5 | 101.6 |
| 20 | 1.1 | 1.6 | 0.01 | 0.17 | 0.05 | 0.3 | 52.5 | 14.3 | 11.5 | 19.7 | 101.2 |
| 21 | 0.4 | 0.7 | 0.01 | 0.30 | 0.03 | 0.1 | 53.4 | 4.0 | 22.0 | 21.4 | 102.3 |
| 22 | 1.4 | 2.9 | - | 0.19 | 0.09 | 0.3 | 50.9 | 17.1 | 11.7 | 16.5 | 101.1 |
| 23 | 0.9 | 1.7 | 0.01 | 0.21 | 0.14 | 0.2 | 49.5 | 13.2 | 13.9 | 19.7 | 99.6 |
| 24 | 1.4 | 2.1 | - | 0.19 | 0.08 | 0.4 | 46.1 | 16.3 | 13.5 | 15.3 | 65.3 |
| Ave. | 1.3 | 2.1 | - | 0.20 | 0.07 | 0.3 | 51.1 | 13.5 | 14.1 | 18.0 | 100.6 |
| Max. | 1.9 | 3.3 | 0.01 | 0.30 | 0.14 | 0.5 | 54.0 | 17.9 | 22.0 | 22.5 | 102.3 |
| Min. | 0.4 | 0.7 | - | 0.14 | - | 0.1 | 46.1 | 4.0 | 9.9 | 14.4 | 95.3 |

**Table S11.** Composition of pyroxene grains in 10049,40 measured with MIT microprobe.

| # | TiO$_2$ | Al$_2$O$_3$ | K$_2$O | MnO | Na$_2$O | Cr$_2$O$_3$ | SiO$_2$ | CaO | FeO | MgO | Total |
|---|---------|-------------|--------|-----|---------|-------------|---------|-----|-----|-----|-------|
| 1 | 1.6 | 2.2 | 0.01 | 0.16 | 0.04 | 0.4 | 50.5 | 16.6 | 11.2 | 17.0 | 99.7 |
| 2 | 1.7 | 2.4 | 0.01 | 0.18 | 0.10 | 0.3 | 50.9 | 15.9 | 11.6 | 17.1 | 100.1 |
| 3 | 1.6 | 2.6 | 0.01 | 0.15 | 0.13 | 0.4 | 50.5 | 16.9 | 11.2 | 16.6 | 100.0 |
| 4 | 1.6 | 2.1 | - | 0.15 | 0.08 | 0.4 | 51.1 | 15.3 | 11.8 | 17.7 | 100.2 |
| 5 | 1.7 | 2.4 | 0.01 | 0.16 | 0.08 | 0.5 | 50.2 | 16.8 | 11.1 | 16.7 | 99.6 |
| 6 | 1.5 | 2.0 | 0.01 | 0.17 | 0.11 | 0.4 | 50.9 | 15.5 | 11.6 | 18.0 | 100.2 |
| 7 | 1.5 | 1.9 | - | 0.17 | 0.05 | 0.4 | 50.8 | 15.1 | 12.0 | 18.1 | 100.0 |
| 8 | 1.3 | 1.8 | 0.01 | 0.19 | 0.08 | 0.4 | 51.4 | 15.8 | 11.8 | 17.6 | 100.4 |
| 9 | 0.7 | 0.9 | 0.02 | 0.34 | 0.01 | 0.2 | 50.0 | 8.7 | 26.3 | 13.3 | 100.6 |
| 10 | 0.6 | 0.7 | 0.04 | 0.41 | 0.04 | 0.2 | 48.7 | 7.2 | 33.2 | 9.2 | 100.3 |
| 11 | 0.7 | 1.0 | 0.01 | 0.33 | 0.01 | 0.1 | 49.4 | 10.5 | 26.3 | 11.5 | 99.9 |
| 12 | 0.6 | 0.7 | - | 0.34 | - | 0.1 | 49.5 | 7.5 | 29.3 | 12.1 | 100.1 |
| 13 | 0.9 | 1.7 | 0.04 | 0.32 | - | 0.2 | 48.4 | 12.8 | 26.0 | 9.6 | 99.9 |
| 14 | 1.1 | 1.7 | - | 0.26 | - | 0.2 | 49.1 | 15.2 | 20.1 | 11.7 | 99.4 |
| 15 | 0.5 | 0.6 | - | 0.36 | - | 0.1 | 48.6 | 6.9 | 35.0 | 8.0 | 100.2 |
| 16 | 0.7 | 1.0 | - | 0.35 | 0.08 | 0.2 | 49.0 | 10.1 | 29.5 | 8.7 | 99.6 |
| Ave. | 1.1 | 1.6 | 0.01 | 0.25 | 0.05 | 0.3 | 49.9 | 12.9 | 19.9 | 13.9 | 100.0 |
| Max. | 0.5 | 0.6 | - | 0.15 | - | 0.1 | 48.4 | 6.9 | 11.1 | 8.0 | 99.4 |
| Min. | 1.7 | 2.6 | 0.04 | 0.41 | 0.13 | 0.5 | 51.4 | 16.9 | 35.0 | 18.1 | 100.6 |

**Table S12.** Composition of high-K glass in 10017,62 measured with MIT microprobe.

| # | TiO$_2$ | Al$_2$O$_3$ | K$_2$O | MnO | Na$_2$O | Cr$_2$O$_3$ | SiO$_2$ | CaO | FeO | MgO | Total |
|---|---------|-------------|--------|-----|---------|-------------|---------|-----|-----|-----|-------|
| 1 | 2.1 | 9.1 | 4.94 | 0.08 | 0.46 | 0.1 | 63.1 | 1.5 | 9.3 | - | 90.7 |
| 2 | 0.7 | 10.8 | 4.62 | 0.01 | 0.64 | - | 79.3 | 0.7 | 2.0 | - | 98.8 |
| 3 | 0.6 | 11.8 | 6.06 | - | 0.60 | - | 76.9 | 0.8 | 2.4 | - | 99.2 |
| 4 | 0.8 | 11.9 | 6.22 | 0.02 | 0.36 | - | 70.3 | 1.2 | 3.4 | - | 94.2 |
| 5 | 0.5 | 11.0 | 6.16 | 0.01 | 0.31 | - | 70.5 | 0.8 | 1.1 | - | 90.3 |
| 6 | 0.6 | 11.1 | 4.49 | 0.01 | 0.95 | - | 75.8 | 2.3 | 2.9 | - | 98.1 |
| 7 | 0.5 | 11.3 | 4.41 | 0.02 | 0.90 | - | 78.9 | 1.9 | 2.4 | - | 100.3 |
| 8 | 0.4 | 12.1 | 5.02 | - | 0.82 | - | 77.9 | 1.8 | 1.2 | - | 99.2 |
| Ave. | 0.8 | 11.2 | 5.24 | 0.02 | 0.63 | - | 74.1 | 1.4 | 3.1 | - | 96.4 |
| Max. | 2.1 | 12.1 | 6.22 | 0.08 | 0.95 | 0.1 | 79.3 | 2.3 | 9.3 | 0.1 | 100.3 |
| Min. | 0.4 | 9.1 | 4.41 | - | 0.31 | - | 63.1 | 0.7 | 1.1 | - | 90.3 |

**Table S13.** Composition of high-K glass in 10049,40 measured with MIT microprobe.

| # | TiO$_2$ | Al$_2$O$_3$ | K$_2$O | MnO | Na$_2$O | Cr$_2$O$_3$ | SiO$_2$ | CaO | FeO | MgO | Total |
|---|---------|-------------|--------|-----|---------|-------------|---------|-----|-----|-----|-------|
| 1 | 0.5 | 10.2 | 4.04 | - | 0.56 | - | 78.8 | 0.7 | 1.7 | - | 96.5 |
| 2 | 0.5 | 11.9 | 4.76 | - | 0.74 | - | 77.4 | 1.1 | 1.4 | - | 97.9 |
| 3 | 0.7 | 11.0 | 4.31 | - | 0.78 | - | 74.9 | 1.5 | 3.8 | 0.1 | 96.9 |
| 4 | 0.7 | 10.8 | 4.22 | - | 0.77 | - | 78.8 | 1.1 | 1.3 | - | 97.8 |
| Ave. | 0.6 | 11.0 | 4.33 | - | 0.71 | - | 77.5 | 1.1 | 2.0 | - | 97.3 |
| Max. | 0.5 | 10.2 | 4.04 | - | 0.56 | - | 74.9 | 0.7 | 1.3 | - | 96.5 |
| Min. | 0.7 | 11.9 | 4.76 | - | 0.78 | - | 78.8 | 1.5 | 3.8 | 0.1 | 97.9 |

**Table S14.** Radiometric ages for 10017 and 10049 compiled from the literature.

| Sample, Method | Age (Ga) | Reference |
|---|---|---|
| **10017** | | |
| K/Ar | 2.45 | (76) |
| | 3.2 (plagioclase) | (76) |
| | 2.200 | (94) |
| | 2.600 | (119) |
| | 2.38±0.11 | (120) |
| | 2.26±0.10 | (120) |
| | 2.200±0.150 | (121) |
| | 2.2-2.4 | (122) |
| | 2.350±0.06 | (95) |
| | 3.260±60 (plagioclase) | (95) |
| | 3.200 | (119) |
| | 2.7 | (123) |
| | 2.63±0.02 | (124) |
| $^{40}Ar/^{39}Ar$ (apparent) | 2.31±0.05 | (77) |
| | 2.30±0.05 | (78) |
| $^{40}Ar/^{39}Ar$ (high temperature) | >3.23±0.06 | (77) |
| | >3.23±0.06 | (78) |
| | >3.23±0.09 | (125) |
| | 3.63±0.11 | (126) |
| Rb/Sr | 3.59±0.08 | (76) |
| | 3.78±0.10 | (127)[1] |
| | 3.575±0.215 | (128) |
| | 3.400±0.600 | (129) |
| | 3.59±0.05 | (130) |
| | 3.71±0.11 | (131)[2] |
| | 3.51±0.05 | (124)[3] |
| | 3.56±0.05 | (126)[4] |
| | 3.633±0.057 | (132) |
| Sm/Nd | 3.678±0.069 | (132) |

[1]Average of 10017 and 10072.
[2]Recalculated from ref. (127).
[3]Recalculated from ref. (130).
[4]Recalculated from ref. (124).

**Table S15.** Radiometric ages compiled from the literature (continued).

| Sample, Method | Age (Ga) | Reference |
|---|---|---|
| **10017** | | |
| $^{81}$Kr/$^{83}$Kr | 2.840±0.160 | (133) |
| | 2.597±0.125 | (133) |
| U/Th | 2.5 | (76) |
| | 2.550 | (119) |
| | 2.950 | (119) |
| | 2.0 | (123) |
| $^{206}$Pb/$^{238}$U | 3.727 | (134) |
| | 3.767 | (135) |
| | 3.616±0.098 | (132) |
| $^{207}$Pb/$^{235}$U | 3.887 | (134) |
| | 3.935 | (135) |
| $^{207}$Pb/$^{206}$Pb | 3.970 | (134) |
| | 4.022 | (135) |
| $^{238}$Pb/$^{232}$Th | 3.643 | (134) |
| | 3.598 | (135) |
| **10049** | | |
| K/Ar | 3.200 | (119) |
| | 2.63±0.02 | (124) |
| $^{40}$Ar/$^{39}$Ar (high temperature) | 3.41±0.04 | (126) |
| U/Th | 2.950 | (119) |

**Table S16.** Cosmic ray exposure ages for 10017 and 10049 compiled from the literature.

| Sample, Method | Age (Ma) | Reference |
|---|---|---|
| **10017** | | |
| $^{38}$Ar | 640±160 | (91) |
| | 510 | (123) |
| | 420-440 | (93)[1] |
| | 440 | (77) |
| | 340-360 | (93) |
| | 510 | (123) |
| $^{81}$Kr/$^{83}$Kr | 510±50 | (94) |
| | 509±29 | (120) |
| | 449±22 | (120) |
| | 509 | (133) |
| | 449 | (133) |
| | 480 | (95) |
| $^{3}$He | 375±40 | (91) |
| | 291 | (119) |
| | 290 | (123) |
| | 300-320 | (93) |
| $^{21}$Ne | 387 | (119) |
| | 340-360 | (93) |
| | 340 | (119) |
| $^{22}$Na-$^{22}$Ne | 340±37 | (121) |
| $^{126}$Xe | 320-340 | (93) |
| Cosmic ray tracks | 11 | (100) |
| | 9-11 | (101) |
| | 5.7 | (103) |
| **10049** | | |
| $^{38}$Ar | 36 | (123) |
| | 21 | (124) |
| $^{3}$He | 23 | (119) |
| | 23 | (123) |
| $^{21}$Ne | 22.5 | (119) |
| | 21 | (123) |

[1]Recalculated from ref. (91).

# Table S17. Complete $^{40}$Ar/$^{39}$Ar incremental heating results.

| # | Temp (°C) | Time (s) | $^{40}$Ar ± 1σ | $^{39}$Ar ± 1σ | $^{38}$Ar ± 1σ | $^{37}$Ar ± 1σ | $^{36}$Ar ± 1σ | $^{40}$Ar* (%) | $^{39}$Ar$_k$ (%) | $^{38}$Ar$_{cos}$ (%) | $^{38}$Ar$_{trap}$ (%) | $^{38}$Ar$_{Cl}$ (%) | $^{36}$Ar$_{cos}$ (%) | $^{36}$Ar$_{trap}$ (%) | Ca/K | Apparent Age ± 1σ (Ma) |
|---|---|---|---|---|---|---|---|---|---|---|---|---|---|---|---|---|

## 10017A    whole-rock fragment

| # | Temp (°C) | Time (s) | $^{40}$Ar ± 1σ | $^{39}$Ar ± 1σ | $^{38}$Ar ± 1σ | $^{37}$Ar ± 1σ | $^{36}$Ar ± 1σ | $^{40}$Ar* (%) | $^{39}$Ar$_k$ (%) | $^{38}$Ar$_{cos}$ (%) | $^{38}$Ar$_{trap}$ (%) | $^{38}$Ar$_{Cl}$ (%) | $^{36}$Ar$_{cos}$ (%) | $^{36}$Ar$_{trap}$ (%) | Ca/K | Apparent Age ± 1σ (Ma) |
|---|---|---|---|---|---|---|---|---|---|---|---|---|---|---|---|---|
| 1 | 460 °C | 597 | 1.50174 ± 0.00161 | 0.01951 ± 0.00017 | 0.00186 ± 0.00002 | 0.01203 ± 0.00070 | 0.00160 ± 0.00002 | 100.0 | 100.0 | 80.8 | 0.0 | 0.0 | 100.0 | 0.0 | 1.2 | 1237 ± 14 |
| 2 | 460 °C | 596 | 1.54592 ± 0.00141 | 0.01814 ± 0.00015 | 0.00167 ± 0.00002 | 0.01029 ± 0.00065 | 0.00132 ± 0.00001 | 100.0 | 100.0 | 81.9 | 4.9 | 0.0 | 67.1 | 32.7 | 1.1 | 1330 ± 15 |
| 3 | 513 °C | 597 | 5.66102 ± 0.00411 | 0.05559 ± 0.00030 | 0.00671 ± 0.00004 | 0.03830 ± 0.00101 | 0.00547 ± 0.00003 | 100.0 | 100.0 | 84.9 | 5.0 | 0.0 | 67.5 | 32.3 | 1.4 | 1505 ± 15 |
| 4 | 513 °C | 597 | 5.49325 ± 0.00521 | 0.04921 ± 0.00024 | 0.00525 ± 0.00004 | 0.02683 ± 0.00093 | 0.00390 ± 0.00003 | 100.0 | 100.0 | 85.0 | 3.6 | 0.0 | 74.2 | 25.6 | 1.1 | 1601 ± 15 |
| 5 | 567 °C | 597 | 15.94103 ± 0.00801 | 0.11025 ± 0.00057 | 0.01611 ± 0.00007 | 0.08107 ± 0.00173 | 0.01253 ± 0.00005 | 100.0 | 99.9 | 87.7 | 4.0 | 0.0 | 73.0 | 26.8 | 1.4 | 1890 ± 17 |
| 6 | 566 °C | 596 | 13.91917 ± 0.00711 | 0.08225 ± 0.00038 | 0.01184 ± 0.00006 | 0.05797 ± 0.00125 | 0.00875 ± 0.00004 | 100.0 | 100.0 | 88.4 | 3.1 | 0.0 | 77.4 | 22.4 | 1.4 | 2079 ± 17 |
| 7 | 620 °C | 596 | 32.28531 ± 0.01701 | 0.15996 ± 0.00071 | 0.03123 ± 0.00010 | 0.16080 ± 0.00173 | 0.02538 ± 0.00009 | 100.0 | 99.9 | 89.3 | 4.4 | 0.0 | 71.2 | 28.6 | 2.0 | 2303 ± 18 |
| 8 | 619 °C | 596 | 24.46371 ± 0.00683 | 0.10508 ± 0.00087 | 0.02210 ± 0.00008 | 0.10484 ± 0.00167 | 0.01662 ± 0.00006 | 100.0 | 99.9 | 89.1 | 3.0 | 0.0 | 78.5 | 21.4 | 2.0 | 2493 ± 21 |
| 9 | 672 °C | 597 | 43.78955 ± 0.02103 | 0.17891 ± 0.00071 | 0.04956 ± 0.00023 | 0.27453 ± 0.00265 | 0.04315 ± 0.00010 | 100.0 | 99.9 | 90.2 | 5.4 | 0.0 | 67.1 | 32.7 | 3.0 | 2561 ± 19 |
| 10 | 672 °C | 597 | 29.39654 ± 0.01402 | 0.11118 ± 0.00064 | 0.03366 ± 0.00010 | 0.19363 ± 0.00186 | 0.02693 ± 0.00008 | 100.0 | 99.9 | 92.1 | 3.8 | 0.0 | 74.6 | 25.2 | 3.4 | 2668 ± 20 |
| 11 | 725 °C | 596 | 44.05292 ± 0.01702 | 0.16062 ± 0.00101 | 0.04987 ± 0.00025 | 0.46025 ± 0.00331 | 0.06666 ± 0.00015 | 100.0 | 99.8 | 91.8 | 5.5 | 0.0 | 66.9 | 32.9 | 5.6 | 2721 ± 21 |
| 12 | 726 °C | 596 | 27.68411 ± 0.00933 | 0.09501 ± 0.00055 | 0.04987 ± 0.00013 | 0.31302 ± 0.00298 | 0.03970 ± 0.00009 | 100.0 | 99.8 | 94.2 | 3.5 | 0.0 | 76.6 | 23.2 | 6.5 | 2807 ± 21 |
| 13 | 778 °C | 594 | 37.06234 ± 0.01303 | 0.12270 ± 0.00065 | 0.08825 ± 0.00034 | 0.62232 ± 0.00465 | 0.08155 ± 0.00012 | 100.0 | 99.6 | 92.1 | 6.2 | 0.0 | 64.6 | 35.2 | 10.0 | 2860 ± 20 |
| 14 | 776 °C | 596 | 22.88186 ± 0.00982 | 0.07017 ± 0.00046 | 0.05962 ± 0.00014 | 0.40840 ± 0.00402 | 0.04435 ± 0.00008 | 100.0 | 99.6 | 96.3 | 2.2 | 0.0 | 83.8 | 15.9 | 11.5 | 2972 ± 22 |
| 15 | 828 °C | 597 | 31.41047 ± 0.02001 | 0.09254 ± 0.00091 | 0.10044 ± 0.00015 | 0.70122 ± 0.00406 | 0.07569 ± 0.00013 | 100.0 | 99.5 | 96.5 | 2.4 | 0.0 | 82.9 | 16.9 | 14.9 | 3032 ± 24 |
| 16 | 829 °C | 597 | 19.90208 ± 0.01101 | 0.06166 ± 0.00056 | 0.06303 ± 0.00014 | 0.44717 ± 0.00361 | 0.04374 ± 0.00009 | 100.0 | 99.5 | 97.7 | 1.1 | 0.0 | 91.2 | 8.6 | 14.3 | 2958 ± 23 |
| 17 | 880 °C | 597 | 29.96778 ± 0.01401 | 0.08563 ± 0.00111 | 0.10177 ± 0.00017 | 0.72663 ± 0.00458 | 0.07177 ± 0.00011 | 100.0 | 99.4 | 97.6 | 1.3 | 0.0 | 89.7 | 10.1 | 16.7 | 3078 ± 27 |
| 18 | 879 °C | 597 | 18.75171 ± 0.00873 | 0.05589 ± 0.00037 | 0.06296 ± 0.00014 | 0.44927 ± 0.00291 | 0.04433 ± 0.00008 | 100.0 | 99.4 | 97.6 | 1.3 | 0.0 | 89.7 | 10.0 | 15.8 | 3016 ± 22 |
| 19 | 931 °C | 597 | 29.42728 ± 0.01003 | 0.08354 ± 0.00051 | 0.10761 ± 0.00019 | 0.68556 ± 0.00435 | 0.07908 ± 0.00011 | 100.0 | 99.4 | 97.1 | 2.0 | 0.0 | 85.5 | 14.2 | 16.2 | 3088 ± 22 |
| 20 | 931 °C | 597 | 14.11806 ± 0.00712 | 0.03946 ± 0.00063 | 0.05964 ± 0.00014 | 0.37453 ± 0.00333 | 0.04221 ± 0.00009 | 100.0 | 99.3 | 97.8 | 1.4 | 0.0 | 89.5 | 10.3 | 18.7 | 3112 ± 31 |
| 21 | 982 °C | 597 | 14.58120 ± 0.00811 | 0.04490 ± 0.00027 | 0.05614 ± 0.00021 | 0.58616 ± 0.00413 | 0.07813 ± 0.00015 | 100.0 | 99.1 | 96.6 | 2.8 | 0.0 | 80.5 | 19.3 | 25.8 | 2973 ± 21 |
| 22 | 982 °C | 597 | 8.01606 ± 0.00601 | 0.02325 ± 0.00022 | 0.05614 ± 0.00013 | 0.32935 ± 0.00298 | 0.04162 ± 0.00009 | 100.0 | 99.0 | 97.4 | 2.1 | 0.0 | 85.1 | 14.7 | 28.0 | 3062 ± 24 |
| 23 | 1032 °C | 597 | 18.02302 ± 0.00942 | 0.05112 ± 0.00038 | 0.50287 ± 0.00070 | 2.71639 ± 0.01088 | 0.33551 ± 0.00031 | 100.0 | 96.3 | 99.5 | 0.4 | 0.0 | 96.5 | 3.2 | 108.1 | 3136 ± 23 |
| 24 | 1032 °C | 596 | 6.57283 ± 0.00433 | 0.01836 ± 0.00019 | 0.16062 ± 0.00023 | 0.88263 ± 0.00591 | 0.10417 ± 0.00014 | 100.0 | 96.7 | 99.8 | 0.0 | 0.0 | 99.7 | 0.1 | 97.5 | 3154 ± 26 |
| 25 | 1083 °C | 597 | 27.30235 ± 0.01502 | 0.08364 ± 0.00063 | 2.64885 ± 0.00480 | 14.26759 ± 0.09923 | 1.68355 ± 0.00250 | 100.0 | 88.1 | 100.2 | -0.3 | 0.0 | 102.1 | -2.4 | 379.3 | 3153 ± 24 |
| 26 | 1083 °C | 596 | 4.77058 ± 0.00432 | 0.01466 ± 0.00022 | 0.35394 ± 0.00054 | 1.55777 ± 0.00818 | 0.21545 ± 0.00033 | 100.0 | 92.6 | 100.8 | -0.9 | 0.0 | 107.3 | -7.4 | 224.9 | 3076 ± 31 |

## 10017B    whole-rock fragment

| # | Temp (°C) | Time (s) | $^{40}$Ar ± 1σ | $^{39}$Ar ± 1σ | $^{38}$Ar ± 1σ | $^{37}$Ar ± 1σ | $^{36}$Ar ± 1σ | $^{40}$Ar* (%) | $^{39}$Ar$_k$ (%) | $^{38}$Ar$_{cos}$ (%) | $^{38}$Ar$_{trap}$ (%) | $^{38}$Ar$_{Cl}$ (%) | $^{36}$Ar$_{cos}$ (%) | $^{36}$Ar$_{trap}$ (%) | Ca/K | Apparent Age ± 1σ (Ma) |
|---|---|---|---|---|---|---|---|---|---|---|---|---|---|---|---|---|
| 1 | 460 °C | 597 | 1.76062 ± 0.00172 | 0.02787 ± 0.00017 | 0.00333 ± 0.00003 | 0.02099 ± 0.00089 | 0.00242 ± 0.00002 | 100.0 | 99.9 | 86.7 | 3.1 | 0.0 | 22.6 | 22.6 | 1.5 | 1068 ± 12 |
| 2 | 460 °C | 596 | 1.71721 ± 0.00161 | 0.02530 ± 0.00019 | 0.00247 ± 0.00002 | 0.01860 ± 0.00078 | 0.00166 ± 0.00002 | 100.0 | 99.9 | 85.3 | 2.3 | 0.0 | 82.0 | 17.7 | 1.4 | 1128 ± 13 |
| 3 | 513 °C | 597 | 5.77492 ± 0.00471 | 0.06962 ± 0.00028 | 0.00891 ± 0.00005 | 0.06202 ± 0.00126 | 0.00625 ± 0.00003 | 100.0 | 99.9 | 88.0 | 2.5 | 0.0 | 81.2 | 18.5 | 1.7 | 1305 ± 13 |
| 4 | 513 °C | 597 | 5.19825 ± 0.00271 | 0.05302 ± 0.00026 | 0.00628 ± 0.00004 | 0.03676 ± 0.00111 | 0.00409 ± 0.00003 | 100.0 | 100.0 | 88.2 | 1.5 | 0.0 | 87.6 | 12.1 | 1.4 | 1466 ± 14 |
| 5 | 567 °C | 596 | 13.80108 ± 0.00852 | 0.10568 ± 0.00047 | 0.01838 ± 0.00009 | 0.11821 ± 0.00205 | 0.01264 ± 0.00005 | 100.0 | 99.9 | 91.2 | 1.8 | 0.0 | 85.9 | 13.9 | 2.2 | 1773 ± 16 |
| 6 | 567 °C | 596 | 11.50581 ± 0.00841 | 0.07493 ± 0.00029 | 0.01312 ± 0.00006 | 0.07886 ± 0.00156 | 0.00887 ± 0.00004 | 100.0 | 99.9 | 91.5 | 1.6 | 0.0 | 87.6 | 12.1 | 2.1 | 1961 ± 16 |
| 7 | 620 °C | 596 | 25.07486 ± 0.01405 | 0.12846 ± 0.00062 | 0.03622 ± 0.00011 | 0.22829 ± 0.00289 | 0.02475 ± 0.00008 | 100.0 | 99.9 | 94.3 | 1.3 | 0.0 | 89.4 | 10.4 | 3.5 | 2261 ± 18 |
| 8 | 620 °C | 596 | 18.42943 ± 0.00892 | 0.08504 ± 0.00043 | 0.02438 ± 0.00010 | 0.15378 ± 0.00184 | 0.01666 ± 0.00006 | 100.0 | 99.9 | 94.4 | 1.3 | 0.0 | 89.4 | 10.3 | 3.5 | 2398 ± 19 |
| 9 | 672 °C | 596 | 32.43182 ± 0.01403 | 0.13306 ± 0.00094 | 0.06126 ± 0.00014 | 0.40979 ± 0.00346 | 0.04226 ± 0.00010 | 100.0 | 99.8 | 96.1 | 1.2 | 0.0 | 90.2 | 9.5 | 6.0 | 2557 ± 21 |
| 10 | 673 °C | 596 | 21.45908 ± 0.01501 | 0.08295 ± 0.00047 | 0.04144 ± 0.00010 | 0.29092 ± 0.00302 | 0.02819 ± 0.00007 | 100.0 | 99.8 | 96.5 | 1.0 | 0.0 | 91.9 | 7.8 | 6.9 | 2640 ± 20 |
| 11 | 724 °C | 597 | 32.90495 ± 0.00925 | 0.11978 ± 0.00071 | 0.09680 ± 0.00028 | 0.71995 ± 0.00433 | 0.06678 ± 0.00013 | 100.0 | 99.6 | 97.4 | 1.1 | 0.0 | 91.4 | 8.3 | 11.8 | 2726 ± 20 |
| 12 | 724 °C | 596 | 20.56260 ± 0.01202 | 0.06936 ± 0.00048 | 0.06647 ± 0.00014 | 0.49333 ± 0.00398 | 0.04445 ± 0.00011 | 100.0 | 99.5 | 98.1 | 0.6 | 0.0 | 95.0 | 4.7 | 14.0 | 2835 ± 21 |
| 13 | 777 °C | 596 | 28.26300 ± 0.01603 | 0.09237 ± 0.00056 | 0.12332 ± 0.00018 | 0.94638 ± 0.00466 | 0.08365 ± 0.00013 | 100.0 | 99.3 | 98.3 | 0.7 | 0.0 | 93.9 | 5.8 | 20.2 | 2884 ± 21 |
| 14 | 777 °C | 596 | 17.59380 ± 0.01201 | 0.05651 ± 0.00037 | 0.07984 ± 0.00017 | 0.62779 ± 0.00488 | 0.05421 ± 0.00009 | 100.0 | 99.2 | 98.4 | 0.8 | 0.0 | 93.8 | 5.9 | 21.9 | 2910 ± 21 |
| 15 | 829 °C | 596 | 24.56330 ± 0.01201 | 0.07674 ± 0.00053 | 0.13263 ± 0.00037 | 1.05738 ± 0.00584 | 0.09070 ± 0.00013 | 100.0 | 99.0 | 98.4 | 0.8 | 0.0 | 93.2 | 6.4 | 27.3 | 2953 ± 22 |
| 16 | 829 °C | 596 | 15.50250 ± 0.01002 | 0.04952 ± 0.00035 | 0.08683 ± 0.00020 | 0.67493 ± 0.00427 | 0.05749 ± 0.00010 | 100.0 | 99.1 | 98.9 | 0.4 | 0.0 | 96.8 | 2.9 | 27.0 | 2920 ± 22 |
| 17 | 881 °C | 597 | 22.87507 ± 0.00673 | 0.07080 ± 0.00044 | 0.13543 ± 0.00028 | 1.05328 ± 0.00573 | 0.09212 ± 0.00014 | 100.0 | 99.0 | 98.6 | 0.8 | 0.0 | 93.9 | 5.8 | 29.5 | 2968 ± 21 |
| 18 | 880 °C | 597 | 13.83350 ± 0.00742 | 0.03945 ± 0.00030 | 0.08554 ± 0.00014 | 0.63703 ± 0.00396 | 0.05633 ± 0.00011 | 100.0 | 98.9 | 99.2 | 0.3 | 0.0 | 97.5 | 2.2 | 32.0 | 3089 ± 23 |
| 19 | 931 °C | 596 | 20.96992 ± 0.00676 | 0.06161 ± 0.00040 | 0.13039 ± 0.00019 | 0.92533 ± 0.00475 | 0.09012 ± 0.00012 | 100.0 | 99.0 | 98.4 | 1.0 | 0.0 | 92.2 | 7.5 | 29.7 | 3044 ± 22 |
| 20 | 931 °C | 596 | 11.43285 ± 0.00831 | 0.03443 ± 0.00035 | 0.08001 ± 0.00014 | 0.56973 ± 0.00448 | 0.05410 ± 0.00010 | 100.0 | 98.9 | 98.8 | 0.6 | 0.0 | 94.7 | 5.1 | 32.8 | 3009 ± 25 |
| 21 | 982 °C | 596 | 12.54876 ± 0.00752 | 0.03858 ± 0.00036 | 0.11933 ± 0.00018 | 0.75991 ± 0.00530 | 0.08197 ± 0.00013 | 100.0 | 98.6 | 98.7 | 0.9 | 0.0 | 93.1 | 6.7 | 39.3 | 2990 ± 24 |
| 22 | 983 °C | 597 | 6.42146 ± 0.00572 | 0.01844 ± 0.00023 | 0.06400 ± 0.00015 | 0.41025 ± 0.00376 | 0.04302 ± 0.00008 | 100.0 | 98.5 | 99.1 | 0.5 | 0.0 | 95.5 | 4.3 | 44.3 | 3085 ± 27 |
| 23 | 1033 °C | 597 | 10.35381 ± 0.00703 | 0.03220 ± 0.00039 | 0.37663 ± 0.00052 | 2.06748 ± 0.00845 | 0.24676 ± 0.00031 | 100.0 | 95.5 | 99.7 | 0.1 | 0.0 | 98.6 | 1.2 | 131.7 | 3012 ± 27 |
| 24 | 1033 °C | 597 | 5.34649 ± 0.00503 | 0.01578 ± 0.00019 | 0.17536 ± 0.00037 | 0.96152 ± 0.00576 | 0.11339 ± 0.00016 | 100.0 | 95.8 | 99.9 | 0.0 | 0.0 | 100.1 | -0.3 | 124.7 | 3086 ± 27 |
| 25 | 1082 °C | 597 | 26.08966 ± 0.01403 | 0.09292 ± 0.00062 | 2.66366 ± 0.00420 | 14.56111 ± 0.15078 | 1.66135 ± 0.00180 | 100.0 | 89.1 | 100.5 | -0.5 | 0.0 | 104.4 | -4.6 | 344.7 | 2916 ± 22 |
| 26 | 1083 °C | 596 | 4.86252 ± 0.00281 | 0.01397 ± 0.00023 | 0.46438 ± 0.00058 | 2.49378 ± 0.00982 | 0.28434 ± 0.00048 | 100.0 | 87.6 | 100.7 | -0.8 | 0.0 | 106.6 | -6.8 | 399.3 | 3259 ± 35 |

## 10049A    whole-rock fragment

| # | Temp (°C) | Time (s) | $^{40}$Ar ± 1σ | $^{39}$Ar ± 1σ | $^{38}$Ar ± 1σ | $^{37}$Ar ± 1σ | $^{36}$Ar ± 1σ | $^{40}$Ar* (%) | $^{39}$Ar$_k$ (%) | $^{38}$Ar$_{cos}$ (%) | $^{38}$Ar$_{trap}$ (%) | $^{38}$Ar$_{Cl}$ (%) | $^{36}$Ar$_{cos}$ (%) | $^{36}$Ar$_{trap}$ (%) | Ca/K | Apparent Age ± 1σ (Ma) |
|---|---|---|---|---|---|---|---|---|---|---|---|---|---|---|---|---|
| 1 | 460 °C | 597 | 3.20159 ± 0.00351 | 0.03554 ± 0.00023 | 0.00061 ± 0.00002 | 0.02045 ± 0.00075 | 0.00019 ± 0.00001 | 100.0 | 100.0 | 26.1 | 2.4 | 0.0 | 41.8 | 41.8 | 1.1 | 1383 ± 14 |
| 2 | 460 °C | 596 | 3.10576 ± 0.00201 | 0.03324 ± 0.00019 | 0.00059 ± 0.00002 | 0.01861 ± 0.00075 | 0.00015 ± 0.00001 | 100.0 | 100.0 | 30.6 | 0.9 | 0.0 | 78.0 | 18.7 | 1.1 | 1419 ± 14 |
| 3 | 514 °C | 597 | 10.78963 ± 0.00571 | 0.09528 ± 0.00047 | 0.00182 ± 0.00002 | 0.06864 ± 0.00168 | 0.00052 ± 0.00002 | 100.0 | 99.9 | 34.9 | 1.0 | 0.0 | 78.4 | 18.2 | 1.4 | 1616 ± 15 |
| 4 | 513 °C | 596 | 9.57229 ± 0.00521 | 0.06902 ± 0.00027 | 0.00132 ± 0.00002 | 0.04783 ± 0.00102 | 0.00036 ± 0.00002 | 100.0 | 100.0 | 35.7 | 0.6 | 0.0 | 84.7 | 11.8 | 1.4 | 1841 ± 16 |
| 5 | 566 °C | 596 | 25.36993 ± 0.01401 | 0.14723 ± 0.00056 | 0.00322 ± 0.00004 | 0.13249 ± 0.00190 | 0.00110 ± 0.00003 | 100.0 | 99.9 | 43.3 | 0.9 | 0.0 | 82.3 | 14.5 | 1.8 | 2102 ± 17 |
| 6 | 567 °C | 596 | 20.36470 ± 0.01201 | 0.09820 ± 0.00049 | 0.00211 ± 0.00004 | 0.08850 ± 0.00184 | 0.00074 ± 0.00002 | 100.0 | 99.9 | 41.8 | 1.3 | 0.0 | 76.8 | 20.0 | 1.8 | 2339 ± 19 |
| 7 | 620 °C | 596 | 42.76576 ± 0.02601 | 0.16593 ± 0.00073 | 0.00445 ± 0.00005 | 0.25277 ± 0.00288 | 0.00201 ± 0.00004 | 100.0 | 99.9 | 52.7 | 1.8 | 0.0 | 75.5 | 21.1 | 3.0 | 2633 ± 19 |
| 8 | 619 °C | 596 | 29.37095 ± 0.01101 | 0.09350 ± 0.00071 | 0.00290 ± 0.00004 | 0.15894 ± 0.00237 | 0.00119 ± 0.00003 | 100.0 | 99.9 | 60.5 | 0.1 | 0.0 | 95.5 | 1.0 | 3.3 | 2913 ± 22 |
| 9 | 672 °C | 597 | 49.10487 ± 0.02103 | 0.14099 ± 0.00102 | 0.00547 ± 0.00006 | 0.43250 ± 0.00391 | 0.00303 ± 0.00004 | 100.0 | 99.8 | 66.5 | 2.0 | 0.0 | 77.6 | 18.6 | 6.0 | 3066 ± 22 |
| 10 | 673 °C | 596 | 29.35852 ± 0.01402 | 0.06946 ± 0.00101 | 0.00339 ± 0.00004 | 0.28703 ± 0.00266 | 0.00181 ± 0.00003 | 100.0 | 99.7 | 74.3 | 0.6 | 0.0 | 90.2 | 5.6 | 8.1 | 3357 ± 30 |
| 11 | 725 °C | 596 | 40.78164 ± 0.01902 | 0.09907 ± 0.00081 | 0.00631 ± 0.00006 | 0.62963 ± 0.00368 | 0.00420 ± 0.00004 | 100.0 | 99.6 | 78.2 | 2.5 | 0.0 | 76.1 | 19.9 | 12.5 | 3319 ± 24 |
| 12 | 725 °C | 596 | 22.91942 ± 0.01102 | 0.05064 ± 0.00050 | 0.00395 ± 0.00004 | 0.42898 ± 0.00380 | 0.00241 ± 0.00003 | 100.0 | 99.4 | 83.5 | 0.8 | 0.0 | 88.6 | 6.7 | 16.7 | 3467 ± 25 |
| 13 | 777 °C | 596 | 30.58871 ± 0.01603 | 0.06035 ± 0.00062 | 0.00573 ± 0.00005 | 0.79830 ± 0.00484 | 0.00460 ± 0.00004 | 100.0 | 99.1 | 87.3 | 1.7 | 0.0 | 82.6 | 12.8 | 26.2 | 3648 ± 26 |
| 14 | 777 °C | 596 | 17.96808 ± 0.01101 | 0.03847 ± 0.00038 | 0.00427 ± 0.00004 | 0.52426 ± 0.00403 | 0.00285 ± 0.00003 | 100.0 | 99.1 | 87.6 | 1.3 | 0.0 | 85.2 | 9.9 | 27.0 | 3521 ± 26 |
| 15 | 829 °C | 597 | 25.25621 ± 0.01201 | 0.05202 ± 0.00051 | 0.00699 ± 0.00005 | 0.86872 ± 0.00555 | 0.00463 ± 0.00004 | 100.0 | 98.8 | 89.9 | 0.9 | 0.0 | 87.8 | 7.2 | 33.1 | 3585 ± 26 |
| 16 | 829 °C | 596 | 15.26924 ± 0.00802 | 0.03126 ± 0.00028 | 0.00431 ± 0.00004 | 0.55160 ± 0.00371 | 0.00283 ± 0.00003 | 100.0 | 98.8 | 90.3 | 0.7 | 0.0 | 88.9 | 5.9 | 35.0 | 3595 ± 25 |
| 17 | 880 °C | 597 | 22.14435 ± 0.00662 | 0.04663 ± 0.00058 | 0.00698 ± 0.00005 | 0.87629 ± 0.00478 | 0.00429 ± 0.00003 | 100.0 | 98.7 | 92.0 | -0.3 | 0.0 | 96.9 | -2.3 | 37.3 | 3553 ± 28 |
| 18 | 880 °C | 596 | 12.44807 ± 0.00534 | 0.02407 ± 0.00026 | 0.00386 ± 0.00004 | 0.49676 ± 0.00367 | 0.00254 ± 0.00003 | 100.0 | 98.6 | 91.7 | 0.6 | 0.0 | 90.2 | 4.6 | 41.0 | 3688 ± 27 |
| 19 | 931 °C | 597 | 17.49107 ± 0.01203 | 0.03804 ± 0.00045 | 0.00571 ± 0.00005 | 0.70986 ± 0.00427 | 0.00370 ± 0.00003 | 100.0 | 98.7 | 91.3 | 0.4 | 0.0 | 91.4 | 3.6 | 37.1 | 3502 ± 28 |
| 20 | 931 °C | 596 | 8.14181 ± 0.00383 | 0.01846 ± 0.00020 | 0.00282 ± 0.00003 | 0.34162 ± 0.00323 | 0.00186 ± 0.00002 | 100.0 | 98.7 | 91.2 | 0.7 | 0.0 | 89.5 | 5.6 | 36.7 | 3438 ± 26 |
| 21 | 982 °C | 597 | 9.66087 ± 0.00632 | 0.02529 ± 0.00027 | 0.00446 ± 0.00004 | 0.52258 ± 0.00336 | 0.00284 ± 0.00003 | 100.0 | 98.6 | 92.9 | 0.1 | 0.0 | 94.5 | 0.6 | 41.1 | 3222 ± 26 |
| 22 | 982 °C | 597 | 3.94802 ± 0.00243 | 0.01126 ± 0.00016 | 0.00216 ± 0.00003 | 0.25429 ± 0.00231 | 0.00147 ± 0.00002 | 100.0 | 98.4 | 92.5 | 1.0 | 0.0 | 87.8 | 7.6 | 45.0 | 3095 ± 29 |
| 23 | 1033 °C | 597 | 4.70622 ± 0.00240 | 0.01476 ± 0.00016 | 0.00878 ± 0.00007 | 1.32031 ± 0.00706 | 0.00594 ± 0.00004 | 100.0 | 93.8 | 97.7 | 0.1 | 0.0 | 93.5 | 0.6 | 186.9 | 3027 ± 26 |
| 24 | 1033 °C | 597 | 2.08237 ± 0.00235 | 0.00635 ± 0.00014 | 0.00100 ± 0.00004 | 0.47742 ± 0.00445 | 0.00068 ± 0.00003 | 100.0 | 94.8 | 92.7 | -0.9 | 0.0 | 88.6 | -7.2 | 155.5 | 3053 ± 40 |

## 10049B    whole-rock fragment

| # | Temp (°C) | Time (s) | $^{40}$Ar ± 1σ | $^{39}$Ar ± 1σ | $^{38}$Ar ± 1σ | $^{37}$Ar ± 1σ | $^{36}$Ar ± 1σ | $^{40}$Ar* (%) | $^{39}$Ar$_k$ (%) | $^{38}$Ar$_{cos}$ (%) | $^{38}$Ar$_{trap}$ (%) | $^{38}$Ar$_{Cl}$ (%) | $^{36}$Ar$_{cos}$ (%) | $^{36}$Ar$_{trap}$ (%) | Ca/K | Apparent Age ± 1σ (Ma) |
|---|---|---|---|---|---|---|---|---|---|---|---|---|---|---|---|---|
| 1 | 460 °C | 596 | 2.37036 ± 0.00161 | 0.02096 ± 0.00014 | 0.00039 ± 0.00001 | 0.01332 ± 0.00080 | 0.00012 ± 0.00001 | 100.0 | 100.0 | 31.6 | 1.9 | 0.0 | 32.3 | 32.3 | 1.2 | 1614 ± 16 |
| 2 | 460 °C | 597 | 2.36827 ± 0.00270 | 0.01943 ± 0.00021 | 0.00040 ± 0.00001 | 0.01275 ± 0.00078 | 0.00011 ± 0.00001 | 100.0 | 100.0 | 40.3 | -0.1 | 0.0 | 98.2 | -1.4 | 1.3 | 1696 ± 19 |
| 3 | 513 °C | 596 | 8.19482 ± 0.00621 | 0.06174 ± 0.00029 | 0.00118 ± 0.00002 | 0.05301 ± 0.00134 | 0.00036 ± 0.00002 | 100.0 | 99.9 | 34.8 | 1.3 | 0.0 | 74.2 | 21.9 | 1.7 | 1791 ± 16 |
| 4 | 513 °C | 597 | 7.52580 ± 0.00451 | 0.04952 ± 0.00035 | 0.00100 ± 0.00002 | 0.03696 ± 0.00101 | 0.00029 ± 0.00002 | 100.0 | 99.9 | 39.3 | 0.5 | 0.0 | 87.2 | 9.5 | 1.5 | 1949 ± 18 |
| 5 | 567 °C | 597 | 20.16475 ± 0.00592 | 0.10977 ± 0.00051 | 0.00224 ± 0.00003 | 0.11097 ± 0.00171 | 0.00081 ± 0.00003 | 100.0 | 99.9 | 44.4 | 0.6 | 0.0 | 86.5 | 9.8 | 2.0 | 2182 ± 18 |
| 6 | 567 °C | 596 | 16.53869 ± 0.00891 | 0.07466 ± 0.00049 | 0.00171 ± 0.00003 | 0.07625 ± 0.00165 | 0.00056 ± 0.00003 | 100.0 | 99.9 | 46.4 | 0.3 | 0.0 | 92.2 | 4.1 | 2.0 | 2426 ± 20 |
| 7 | 620 °C | 596 | 34.87406 ± 0.01702 | 0.13107 ± 0.00068 | 0.00359 ± 0.00005 | 0.22033 ± 0.00244 | 0.00135 ± 0.00003 | 100.0 | 99.9 | 55.4 | 0.0 | 0.0 | 95.7 | 0.0 | 3.3 | 2677 ± 20 |
| 8 | 620 °C | 596 | 24.34519 ± 0.00812 | 0.07966 ± 0.00054 | 0.00229 ± 0.00003 | 0.14497 ± 0.00218 | 0.00096 ± 0.00002 | 100.0 | 99.9 | 56.7 | 0.7 | 0.0 | 87.3 | 8.7 | 3.6 | 2874 ± 21 |
| 9 | 672 °C | 596 | 40.42981 ± 0.01303 | 0.11615 ± 0.00097 | 0.00454 ± 0.00006 | 0.36341 ± 0.00292 | 0.00224 ± 0.00004 | 100.0 | 99.8 | 68.2 | 0.6 | 0.0 | 89.7 | 6.0 | 6.1 | 3065 ± 23 |
| 10 | 672 °C | 597 | 24.57482 ± 0.00882 | 0.06522 ± 0.00047 | 0.00285 ± 0.00004 | 0.24480 ± 0.00275 | 0.00139 ± 0.00003 | 100.0 | 99.7 | 72.0 | -0.1 | 0.0 | 96.0 | -0.7 | 7.4 | 3183 ± 23 |
| 11 | 725 °C | 597 | 34.61958 ± 0.01902 | 0.08242 ± 0.00058 | 0.00541 ± 0.00006 | 0.56357 ± 0.00423 | 0.00305 ± 0.00004 | 100.0 | 99.5 | 81.1 | 0.2 | 0.0 | 93.3 | 1.8 | 13.5 | 3351 ± 23 |
| 12 | 725 °C | 597 | 19.51817 ± 0.01002 | 0.04535 ± 0.00056 | 0.00330 ± 0.00004 | 0.37102 ± 0.00306 | 0.00194 ± 0.00003 | 100.0 | 99.4 | 82.7 | 0.4 | 0.0 | 91.0 | 3.9 | 16.1 | 3389 ± 28 |
| 13 | 777 °C | 597 | 26.24394 ± 0.00825 | 0.05591 ± 0.00050 | 0.00568 ± 0.00005 | 0.68188 ± 0.00428 | 0.00355 ± 0.00004 | 100.0 | 99.2 | 87.3 | 0.5 | 0.0 | 90.5 | 4.4 | 24.1 | 3527 ± 25 |

| 14 | 777 °C | 597 | 15.73226 ± 0.00871 | 0.03384 ± 0.00026 | 0.00358 ± 0.00004 | 0.45158 ± 0.00329 | 0.00231 ± 0.00003 | 100.0 | 99.1 | 87.4 | 0.9 | 0.0 | 87.5 | 7.3 | 26.4 | 3514 ± 24 |
| 15 | 829 °C | 597 | 22.37923 ± 0.00961 | 0.04634 ± 0.00043 | 0.00612 ± 0.00005 | 0.78030 ± 0.00480 | 0.00392 ± 0.00003 | 100.0 | 98.8 | 90.2 | 0.4 | 0.0 | 91.2 | 3.6 | 33.4 | 3576 ± 25 |
| 16 | 828 °C | 596 | 13.35474 ± 0.00752 | 0.02701 ± 0.00038 | 0.00382 ± 0.00004 | 0.49107 ± 0.00370 | 0.00237 ± 0.00003 | 100.0 | 98.7 | 91.3 | -0.1 | 0.0 | 95.2 | -0.7 | 36.1 | 3615 ± 30 |
| 17 | 880 °C | 597 | 19.16601 ± 0.00593 | 0.04044 ± 0.00033 | 0.00569 ± 0.00005 | 0.74324 ± 0.00515 | 0.00365 ± 0.00003 | 100.0 | 98.7 | 90.8 | 0.4 | 0.0 | 91.7 | 2.9 | 36.5 | 3549 ± 24 |
| 18 | 881 °C | 595 | 10.64919 ± 0.00882 | 0.02264 ± 0.00028 | 0.00337 ± 0.00003 | 0.41134 ± 0.00405 | 0.00207 ± 0.00002 | 100.0 | 98.7 | 91.9 | -0.2 | 0.0 | 96.8 | -2.1 | 36.1 | 3537 ± 28 |
| 19 | 931 °C | 597 | 15.04436 ± 0.00923 | 0.03262 ± 0.00026 | 0.00478 ± 0.00004 | 0.61627 ± 0.00465 | 0.00309 ± 0.00003 | 100.0 | 98.7 | 91.1 | 0.4 | 0.0 | 91.2 | 3.5 | 37.5 | 3507 ± 24 |
| 20 | 931 °C | 597 | 7.05227 ± 0.00372 | 0.01636 ± 0.00021 | 0.00251 ± 0.00003 | 0.30259 ± 0.00284 | 0.00156 ± 0.00002 | 100.0 | 98.7 | 92.0 | -0.1 | 0.0 | 95.7 | -0.8 | 36.7 | 3403 ± 28 |
| 21 | 982 °C | 597 | 7.95303 ± 0.00602 | 0.02261 ± 0.00022 | 0.00358 ± 0.00004 | 0.44188 ± 0.00393 | 0.00235 ± 0.00003 | 100.0 | 98.6 | 91.6 | 0.6 | 0.0 | 90.4 | 4.7 | 38.8 | 3097 ± 24 |
| 22 | 982 °C | 596 | 2.97412 ± 0.00322 | 0.00846 ± 0.00016 | 0.00159 ± 0.00003 | 0.19633 ± 0.00210 | 0.00101 ± 0.00002 | 100.0 | 98.4 | 93.4 | -0.1 | 0.0 | 95.4 | -0.5 | 46.2 | 3100 ± 35 |
| 23 | 1033 °C | 596 | 4.22834 ± 0.00345 | 0.01413 ± 0.00022 | 0.00728 ± 0.00006 | 1.20176 ± 0.00539 | 0.00476 ± 0.00003 | 100.0 | 94.1 | 97.9 | -0.5 | 0.0 | 97.0 | -3.6 | 177.1 | 2929 ± 31 |
| 24 | 1032 °C | 596 | 2.58907 ± 0.00323 | 0.00738 ± 0.00014 | 0.00195 ± 0.00004 | 0.60176 ± 0.00504 | 0.00146 ± 0.00003 | 100.0 | 94.3 | 94.0 | 1.1 | 0.0 | 81.4 | 7.7 | 169.5 | 3161 ± 35 |

Isotope abundances given in nanoamps (spectrometer sensitivity is ~1.8 x 10$^{-14}$ moles/nA),

and corrected for $^{37}$Ar and $^{39}$Ar decay, with half-lives of 35.2 days and 269 years, respectively,

and for spectrometer discrimination per atomic mass unit of 1.004535 ± 0.002968.

Isotope sources calculated using the reactor constants in Renne et al. (2005),

and assuming ($^{38}$Ar/$^{36}$Ar)$_{cos}$ = 1.54, ($^{38}$Ar/$^{38}$Ar)$_{tran}$ = 0.188, and ($^{40}$Ar/$^{38}$Ar)$_{tran}$ = 0.

No corrections were made for cosmogenic $^{40}$Ar.

Ages were calculated using the decay constants and standard age calibration of Renne et al. (2011) and K isotope abundances of Steiger and Jäger (1977)

and calculated relative to Hb3gr fluence monitor (1081.0 ± 1.2 Ma).

J-Value is 0.0262509 ± 0.0002064 (analytical uncertainties only, excludes uncertainty on the standard age).

Uncertainties on apparent step ages include anlytical uncertainties on isotope measurements, interfearence corrections, and the J-value, but exclude decay constant and standard age uncertainties.

Plateau ages were calculated as the weighted average $^{40}$Ar*/$^{39}$Ar$_K$ ratio of steps 13-18.

Average analytical blanks are: $^{40}$Ar = 0.03; $^{39}$Ar = 0.0009; $^{38}$Ar = 0.0002; $^{37}$Ar = 0.00005; $^{36}$Ar = 0.0002 (nanoamps).

Temperature was controlled with approximately ± 5 °C precision and ± 10 °C accuracy.

Data shown in gray are indeterminate or negligibly above the detection limit.

**Table S18.** Summary of MP-MDD model parameters.

| Phase | $E_a$ (kJ/mol) | $\ln(D_o/a^2)_1$ ($\ln(s^{-1})$) | $\Phi_{1\text{-}39}$ | $\Phi_{1\text{-}37}$ | Ca/K | P38$_{Ca}$ (mol/g$_{Ca}$/Ma) | $\ln(D_o/a^2)_2$ ($\ln(s^{-1})$) | $\Phi_{2\text{-}39}$ | $\Phi_{2\text{-}37}$ | Ca/K | P38$_{Ca}$ (mol/g$_{Ca}$/Ma) |
|---|---|---|---|---|---|---|---|---|---|---|---|
| **10017-2** | | | | | | | | | | | |
| Plagioclase | 179 | 9.5 | 0.133 | 0.637 | 64 | 8.25 x 10$^{-15}$ | 7.6 | 0.073 | 0.350 | 64 | 8.25 x 10$^{-15}$ |
| K-Glass | 139 | 8.9 | 0.450 | 0.007 | 0.22 | 6.43 x 10$^{-14}$ | 5.4 | 0.344 | 0.006 | 0.22 | 6.43 x 10$^{-14}$ |
| **10049-2** | | | | | | | | | | | |
| Plagioclase | 181 | 10.2 | 0.116 | 0.537 | 57 | 8.25 x 10$^{-15}$ | 8.3 | 0.098 | 0.450 | 57 | 8.25 x 10$^{-15}$ |
| K-Glass | 142 | 9.3 | 0.550 | 0.009 | 0.21 | 6.72 x 10$^{-14}$ | 5.9 | 0.236 | 0.004 | 0.21 | 6.72 x 10$^{-14}$ |

Each phase is fit with a two domain model.

$\Phi$ is the fraction of $^{39}$Ar$_K$ or $^{37}$Ar$_{Ca}$ contained within a given domain and is calculated based on the total released in the first 22 extractions.

P38$_{Ca}$ is the domain-specific production rate for $^{38}$Ar$_{cos}$ and is calculated based on the relative concentrations of K, Ca, and Fe in plagioclase and K and Ca in K-glass.

Fe/Ca ratios in 10017 and 10049 plagioclase are 0.033 and 0.046, respectively.

Total $^{39}$Ar$_K$, $^{37}$Ar$_{Ca}$, and $^{38}$Ar$_{cos}$ signals in 10017 are 1.506, 10.29, and 1.386 nanoamps, respectively.

Total $^{39}$Ar$_K$, $^{37}$Ar$_{Ca}$, and $^{38}$Ar$_{cos}$ signals in 10049 are 1.157, 7.33, and 0.0553 nanoamps, respectively.

**Supplementary References:**

49. Helsley CE (1970) Magnetic properties of lunar 10022, 10069, 10084 and 10085 samples. *Proc. Apollo 11 Lunar Sci. Conf.*:2213-2219.

50. Stephenson A, Collinson DW, & Runcorn SK (1974) Lunar magnetic field paleointensity determinations on Apollo 11, 16, and 17 rocks. *Proc. Lunar Planet. Sci. Conf. 5th*:2859-2871.

51. Stephenson A & Collinson DW (1974) Lunar magnetic field palaeointensities determined by an anhysteretic remanent magnetization method. *Earth Planet. Sci. Lett.* 23:220-228.

52. Tikoo SM*, et al.* (2012) Magnetic fidelity of mare basalts and implications for a lunar dynamo. *Earth Planet. Sci. Lett.* 337-338:93-103.

53. Kirschvink JL, Kopp RE, & Raub TD (2008) Rapid, precise, and high-sensitivity acquisition of paleomagnetic and rock-magnetic data: Development of a low-noise automatic sample changing system for superconducting rock magnetometers. *Geochem. Geophys. Geosyst.* 9:Q05Y01, doi:10.1029/2007GC001856.

54. Weiss BP, Gattacceca J, Stanley S, Rochette P, & Christensen UR (2010) Paleomagnetic records of meteorites and early planetesimal differentiation. *Space Sci. Rev.* 152:341-390.

55. Kirschvink JL (1980) The least-squares line and plane and the analysis of paleomagnetic data: examples from Siberia and Morocco. *Geophys. J. R. Astr. Soc.* 62:699-718.

56. Weiss BP*, et al.* (2008) Magnetism on the angrite parent body and the early differentiation of planetesimals. *Science* 322:713-716.

57. Muxworthy AR, Heslop D, Paterson GA, & Michalk D (2011) A Preisach method for estimating absolute paleofield intensity under the constraint of using only isothermal measurements: 2. Experimental testing. *J. Geophys. Res.* 116:doi:10.1029/2010JB007844.

58. Yu Y (2010) Paleointensity determination using anhysteretic remanence and saturation isothermal remanence. *Geochem. Geophys. Geosyst.* 11:Q02Z12, doi:10.1029/2009GC002804.

59. Kletetschka G, Acuna MH, Kohout T, Wasilewski PJ, & Connerney JEP (2004) An empirical scaling law for acquisition of thermoremanent magnetization. *Earth Planet. Sci. Lett.* 226:521-528.

60. Cisowski SM, Collinson DW, Runcorn SK, Stephenson A, & Fuller M (1983) A review of lunar paleointensity data and implications for origin of lunar magnetism. *Proc. Lunar Planet. Sci. Conf. 13th*:A691-A704.

61. Yu YJ (2006) How accurately can NRM/SIRM determine the ancient planetary magnetic field intensity? *Earth Planet. Sci. Lett.* 250:27-37.

62. Fuller M (1974) Lunar magnetism. *Rev. Geophys. Space Phys.* 12:23-69.

63. Cisowski S (1981) Interacting vs. non-interacting single-domain behavior in natural and synthetic samples. *Phys. Earth Planet. Inter.* 26:56-62.

64. Lowrie W & Fuller M (1971) On the alternating-field demagnetization characteristics of multidomain thermoremanent magnetization in magnetite. *J. Geophys. Res.* 76:6339-6349.

65. Xu S & Dunlop DJ (1995) Toward a better understanding of the Lowrie-Fuller test. *J. Geophys. Res.* 100:22533-22542.

66. Kohout T, Kletetschka G, Donadini F, Fuller M, & Herrero-Bervera E (2008) Analysis of the natural remanent magnetization of rocks by measuring the efficiency ratio through alternating field demagnetization spectra. *Stud. Geophys. Geod.* 52:225-235.

67. Wasilewski P (1988) Magnetic characterization of the new magnetic mineral tetrataenite and its contrast with isochemical taenite. *Phys. Earth Planet. Inter.* 52:150-158.

68. Kirichenko A, Kornilov A, & Pudalov V (2005) Properties of Polyethylsiloxane as a Pressure-Transmitting Medium. *Instrum. Exp. Tech.* 48:813-816.

69. Armstrong JT (1982) *Microbeam Analysis*, ed Heinrich KFJ (San Francisco Press, San Francisco), pp 175-180.

70. Armstrong JT (1995) CITZAF: a package of correction programs for the Quantitative electron micrbeam X-ray analysis of thick polished materials, thin films, and particles. *Microbeam Anal.* 4:177-200.

71. Armstrong JT (1991) *Electron Probe Quantitation*, ed K. F. J. Heinrich DEN (Plenum Press), pp 261-315.

72. Pouchou JL & Pichoir F (1991) *Electron Probe Quantitation*, ed K. F. J. Heinrich DEN (Plenum Press), pp 261-315.

73. Stephenson A, Sadikun S, & Potter D, K. (1986) A theoretical and experimental comparison of the anisotropies of magnetic susceptibility and remanence in rocks and minerals. *Geophys. J. R. Astr. Soc.* 84:185-2000.

74. Nye JF (1985) *Physical Properties of Crystals: Their Representation by Tensors and Matrices* (Oxford University Press, Oxford).

75. Selkin PA, Gee JS, Tauxe L, Meurer WP, & Newell AJ (2000) The effect of remanence anisotropy on paleointensity estimates: a case study from the Archean Stillwater Complex. *Earth Planet. Sci. Lett.* 183:403-416.

76. Albee AL*, et al.* (1970) Ages, irradiation history, and chemical composition of lunar rocks from the Sea of Tranquillity. *Science* 167:463-466.

77. Turner G (1970) Argon-40/argon-39 dating of lunar rock samples. *Proc. Apollo 11 Lunar Sci. Conf.*:1665-1684.

78. Turner G (1970) Argon-40/Argon-39 dating of lunar rock samples. *Science* 167:466-468.

79. Compston W, Chappell BW, Arriens PA, & Vernon MJ (1970) The chemistry and age of Apollo 11 lunar material. *Proc. Apollo 11 Lunar Sci. Conf.* 1:1007.

80. Gopalan K, Kaushal S, Lee-Hu C, & Wetherill GW (1970) Rubidium-strontium, uranium, and thorium-lead dating of lunar material. *Science* 167:471-473.

81. Gopalan K, Kaushal S, Lee-Hu C, & Wetherill GW (1970) Rb-Sr and U, Th-Pb ages of lunar materials. *Proc. Apollo 11 Lunar Sci. Conf.*:1195.

82. Papanastassiou DA, Wasserburg GJ, & Burnett DS (1970) Rb-Sr ages of lunar rocks from the sea of tranquillity. *Earth Planet. Sci. Lett.* 8:1-19.

83. De Laeter JR, Vernon MJ, & Compston W (1973) Revision of lunar Rb-Sr ages. *Geochim. Cosmochim. Acta* 37:700-702.

84. Guggisberg S*, et al.* (1979) Classification of the Apollo-11 mare basalts according to $Ar^{39}$-$Ar^{40}$ ages and petrological properties. *Proc. Lunar Planet. Sci. Conf. 10th*:1-39.

85. Gaffney AM, Borg LE, & Asmerom Y (2007) The origin of geochemical diversity of lunar mantle sources inferred from the combined U–Pb, Rb–Sr, and Sm–Nd isotope systematics of mare basalt 10017. *Geochim. Cosmochim. Acta* 71:3656-3671.

86. Marti K, Lugmair GW, & Urey HC (1970) Solar wind gases, cosmic ray spallation products, and the irradiation history. *Science* 167:548-550.

87. Marti K, Lugmair GW, & Urey HC (1970) Solar wind gases, cosmic-ray spallation products and the irradiation history of Apollo 11 samples. *Proc. Apollo 11 Lunar Sci. Conf.*:1357.

88. Hintenberger H*, et al.* (1970) Rare gases, hydrogen, and nitrogen: Concentrations and isotopic composition in lunar material. *Science* 167:543-545.

89. Tatsumoto M (1970) Age of the moon: An isotopic study of U-Th-Pb systematics of Apollo 11 lunar samples-II. *Proc. Apollo 11 Lunar Sci. Conf.*:1595.

90. Tatsumoto M & Rosholt JN (1970) Age of the Moon: An isotopic study of uranium-thorium-lead systematics of lunar samples. *Science* 167:461-463.

91. Fireman EL, D'Amico JC, & DeFelice JC (1970) Tritium and argon radioactivties in lunar material. *Science* 167:566-568.

92. Hintenberger H, Weber HW, & Takaoka N (1971) Concentrations and isotopic abundances of the rare gases in lunar matter. *Proc. Lunar Sci. Conf. 2nd*:1607-1625.

93. Bogard DD, Funkhouser JG, Schaeffer OA, & Zahringer J (1971) Noble gas abundances in lunar material. Cosmic-ray spallation products and radiation ages from the Sea of Tranquilitatis and the Ocean of Storms. *J. Geophys. Res.* 76:2757-2779.

94. Eberhardt P, *et al.* (1970) Trapped solar wind boble gases, $Kr^{81}/Kr$ exposure ages and K/Ar ages in Apollo 11 lunar material. *Science* 167:558-560.

95. Eberhardt P, *et al.* (1974) Noble gas investigations of lunar rocks 10017 and 10071. *Geochim. Cosmochim. Acta* 38:97-120.

96. O'Kelley GD, Eldridge JS, Schonfeld E, & Bell PR (1970) Elemental compositions and ages of lunar samples by nondestructive gamma-ray spectrometry. *Science* 167:580-582.

97. Burnett DS, Huneker JC, Podasek FA, Price Russ G, & Wasserburg GJ (1971) The irradiation history of lunar samples. *Proc. Lunar Sci. Conf. 2nd*:1671.

98. Shedlovsky JP, *et al.* (1970) Pattern of bombardment-produced radionuclides in rock 10017 and in lunar soil. *Proc. Apollo 11 Lunar Sci. Conf.*:1503.

99. Shedlovsky JP, *et al.* (1970) Pattern of bombardment-produced radionuclides in rock 10017 and in lunar soil. *Science* 167:574-576.

100. Crozaz G, *et al.* (1970) Solid state studies of the radiation history of lunar samples. *Science* 167:563-566.

101. Lal D, MacDougall D, Wilkening L, & Arrhenius G (1970) Mixing of the lunar regolith and cosmic ray spectra: Evidence from particle-track studies. *Proc. Apollo 11 Lunar Sci. Conf.*:2295.

102. Fleischer RL, *et al.* (1970) Particle track, x-ray, thermal, and mass spectrometric studies of lunar material. *Science* 167:568-571.

103. Fleischer RL, Haines EL, Hart HR, Woods RT, & Comstock GM (1970) The particle track record of the Sea of Tranquillity. *Proc. Apollo 11 Lunar Sci. Conf.*:2103.

104. Eberhardt P, *et al.* (1970) Correlation between rock type and irradiation history of Apollo 11 igneous rocks. *Earth Planet. Sci. Lett.* 10:67-72.

105. Geiss J, *et al.* (1977) Absolute time scale of lunar mare formation and filling. *Phil. Trans. R. Soc. London A* 285:151-158.

106. Beaty DW & Albee AL (1980) The geology and petrology of the Apollo 11 landing site. *Proc. Lunar Planet. Sci. Conf. 11th*:23-35.

107. Cassata WS, Renne PR, & Shuster DL (2009) Argon diffusion in plagioclase and implications for thermochronometry: A case study from the Bushveld Complex, South Africa. *Geochim. Cosmochim. Acta* 73:6600-6612.

108. Shuster DL, *et al.* (2010) A record of impacts preserved in the lunar regolith. *Earth Planet. Sci. Lett.* 290:155-165.

109. Steiger RH & Jager E (1977) Subcommission on Geochronology - Convention on use of decay constants in geochronology and cosmochronology. *Earth Planet. Sci. Lett.* 36:359-362.

110. Cassata W, Shuster DL, Renne PR, & Weiss BP (2010) Evidence for shock heating and constraints on Martian surface temperatures revealed by $^{40}Ar/^{39}Ar$ thermochronometry of Martian meteorites *Geochim. Cosmochim. Acta* 74:6900-6920.

111. Lovera OM, Richter FM, & Harrison TM (1991) Diffusion domains determined by $^{39}Ar$ released during step heating. *J. Geophys. Res.* 96:2057-2069.

112. Huang S (2008) Surface temperatures at the nearside of the Moon as a record of the radiation budget of Earth's climate system. *Adv. Space. Res* 41:1853-1860.

113. Bauch KE, Hiesinger H, & Helbert J (2009) Estimation of lunar surface temperatures: A numerical model. *Lunar Planet. Sci. Conf. XL*:abstract #1789.

114. Roelof EC (1968) Thermal behavior of rocks on the lunar surface. *Icarus* 8(1–3):138-159.

115. Keihm SJ, Peters K, & Langseth MG (1973) Apollo 15 measurement of lunar surface brightness temperature thermal conductivity of the upper 1 1/2 meters of regolith. *Earth and Planetary Science Letters* 19:337-351.

116. McNeill DF (1997) Facies and early diagenetic influence on the depositional magnetization of carbonates. *Geology* 25:799-802.

117. Morbidelli A, Marchi S, Bottke WF, & Kring DA (2012) A sawtooth-like timeline for the first billion years of lunar bombardment. *Earth Planet. Sci. Lett.* 355-356:144-151.

118. Wagner R, Head JW, Wolf U, & Neukum G (2002) Stratigraphic sequence and ages of volcanic units in the Gruithuisen region of the Moon. *J. Geophys. Res.* 107(E11):5104.
119. Hintenberger H, *et al.* (1970) Rare gases, hydrogen, and nitrogen: Concentrations and isotopic composition in lunar material. *Science* 167:543-545.
120. Marti K, Lugmair GW, & Urey HC (1970) Solar wind gases, cosmic-ray spallation products and the irradiation history of Apollo 11 samples. *Proc. Apollo 11 Lunar Sci. Conf.*:1357.
121. O'Kelley GD, Eldridge JS, Schonfeld E, & Bell PR (1970) Elemental compositions and ages of lunar samples by nondestructive gamma-ray spectrometry. *Science* 167:580-582.
122. Schaeffer OA, Funkhouser JG, Bogard DD, & Zähringer J (1970) Potassium-argon ages of lunar rocks from Mare Tranquillitatis and Oceanus Procellarum. *Science* 170:161-162.
123. Hintenberger H, Weber HW, & Takaoka N (1971) Concentrations and isotopic abundances of the rare gases in lunar matter. *Proc. Lunar Sci. Conf. 2nd*:1607-1625.
124. Guggisberg S, *et al.* (1979) Classification of the Apollo-11 mare basalts according to $Ar^{39}$-$Ar^{40}$ ages and petrological properties. *Proc. Lunar Planet. Sci. Conf. 10th*:1-39.
125. Turner G (1971) $^{40}$Ar-$^{39}$Ar ages from the lunar maria. *Earth Planet. Sci. Lett.* 11:161-191.
126. Snyder GA, Lee D-C, Taylor LA, Halliday AN, & Jerde EA (1994) Evolution of the upper mantle of the Earth's Moon: Neodymium and strontium isotopic constraints from high-Ti mare basalts. *Geochim. Cosmochim. Acta* 58:4795-4808.
127. Compston W, Chappell BW, Arriens PA, & Vernon MJ (1970) The chemistry and age of Apollo 11 lunar material. *Proc. Apollo 11 Lunar Sci. Conf.* 1:1007.
128. Gopalan K, Kaushal S, Lee-Hu C, & Wetherill GW (1970) Rb-Sr and U, Th-Pb ages of lunar materials. *Proc. Apollo 11 Lunar Sci. Conf.*:1195.
129. Gopalan K, Kaushal S, Lee-Hu C, & Wetherill GW (1970) Rubidium-strontium, uranium, and thorium-lead dating of lunar material. *Science* 167:471-473.
130. Papanastassiou DA, Wasserburg GJ, & Burnett DS (1970) Rb-Sr ages of lunar rocks from the sea of tranquillity. *Earth Planet. Sci. Lett.* 8:1-19.
131. De Laeter JR, Vernon MJ, & Compston W (1973) Revision of lunar Rb-Sr ages. *Geochim. Cosmochim. Acta* 37:700-702.
132. Gaffney AM, Borg LE, & Asmerom Y (2007) The origin of geochemical diversity of lunar mantle sources inferred from the combined U–Pb, Rb–Sr, and Sm–Nd isotope systematics of mare basalt 10017. *Geochim. Cosmochim. Acta* 71:3656-3671.
133. Marti K, Lugmair GW, & Urey HC (1970) Solar wind gases, cosmic ray spallation products, and the irradiation history. *Science* 167:548-550.
134. Tatsumoto M (1970) Age of the moon: An isotopic study of U-Th-Pb systematics of Apollo 11 lunar samples-II. *Proc. Apollo 11 Lunar Sci. Conf.*:1595.
135. Tatsumoto M & Rosholt JN (1970) Age of the Moon: An isotopic study of uranium-thorium-lead systematics of lunar samples. *Science* 167:461-463.
136. Langseth MG, Keihm SJ, & Peters K (1976) Revised lunar heat-flow values. *Proc. Lunar Sci. Conf. 7th*:3143.